Integrated photonics on thin-film lithium niobate

Di Zhu,[1,*] **Linbo Shao,**[1] **Mengjie Yu,**[1]
Rebecca Cheng,[1] **Boris Desiatov,**[1] **C. J. Xin,**[1]
Yaowen Hu,[1] **Jeffrey Holzgrafe,**[1] **Soumya Ghosh,**[1]
Amirhassan Shams-Ansari,[1] **Eric Puma,**[1]
Neil Sinclair,[1,2] **Christian Reimer,**[3] **Mian Zhang,**[3]
and Marko Lončar[1,4]

[1]*John A. Paulson School of Engineering and Applied Sciences, Harvard University, 29 Oxford Street, Cambridge, Massachusetts 02138, USA*
[2]*Division of Physics, Mathematics and Astronomy, and Alliance for Quantum Technologies (AQT), California Institute of Technology, 1200 E. California Boulevard, Pasadena, California 91125, USA*
[3]*HyperLight Corporation, 501 Massachusetts Avenue, Cambridge, Massachusetts 02139, USA*
[4]*e-mail: loncar@seas.harvard.edu*
Corresponding author: dizhu@g.harvard.edu

Lithium niobate (LN), an outstanding and versatile material, has influenced our daily life for decades—from enabling high-speed optical communications that form the backbone of the Internet to realizing radio-frequency filtering used in our cell phones. This half-century-old material is currently embracing a revolution in thin-film LN integrated photonics. The successes of manufacturing wafer-scale, high-quality thin films of LN-on-insulator (LNOI) and breakthroughs in nanofabrication techniques have made high-performance integrated nanophotonic components possible. With rapid development in the past few years, some of these thin-film LN devices, such as optical modulators and nonlinear wavelength converters, have already outperformed their legacy counterparts realized in bulk LN crystals. Furthermore, the nanophotonic integration has enabled ultra-low-loss resonators in LN, which has unlocked many novel applications such as optical frequency combs and quantum transducers. In this review, we cover—from basic principles to the state of the art—the diverse aspects of integrated thin-film LN photonics, including the materials, basic passive components, and various active devices based on electro-optics, all-optical nonlinearities, and acousto-optics. We also identify challenges that this platform is currently facing and point out future opportunities. The field of integrated LNOI photonics is advancing rapidly and poised to make critical impacts on a broad range of applications in communication, signal processing, and quantum information. © 2021 Optical Society of America

Integrated photonics on thin-film lithium niobate

DI ZHU, LINBO SHAO, MENGJIE YU, REBECCA CHENG,
BORIS DESIATOV, C. J. XIN, YAOWEN HU,
JEFFREY HOLZGRAFE, SOUMYA GHOSH,
AMIRHASSAN SHAMS-ANSARI, ERIC PUMA, NEIL SINCLAIR,
CHRISTIAN REIMER, MIAN ZHANG, AND MARKO LONČAR

1. INTRODUCTION

Integrated photonics holds great promise for realizing low-cost and scaled optical solutions for communication, sensing, and computation. Moreover, the miniaturization and integration of photonic structures enable new design knobs and functionalities that are inaccessible in their bulk counterparts. Many material systems have been investigated and adopted for integrated photonics. Good examples include silicon (Si) [1], indium phosphide (InP) [2], silicon nitride (SiN_x) [3], gallium arsenide (GaAs) [4], aluminum nitride (AlN) [5,6], and silicon carbide (SiC) [7]. Despite great progress, these material platforms cannot simultaneously support ultra-low propagation loss, fast and low-loss optical modulation, and efficient all-optical nonlinearities.

Studied since the 1960s, lithium niobate ($LiNbO_3$, LN) is one of the most versatile and attractive materials for photonics, owing to its exceptional electro-, nonlinear-, and acousto-optic properties, as well as its wide transparency window and relatively high refractive index. For instance, LN electro-optic modulators are ubiquitous in fiber-optic communications, while periodically poled lithium niobate (PPLN) is widely used for wavelength conversion and photon-pair generation. Despite its great potential, LN had generally fallen behind the competing integrated photonic platforms, mainly due to the significant difficulties of material integration and processing. Traditional integrated LN devices are based on low-index-contrast waveguides, normally formed by titanium (Ti) indiffusion or proton exchange in bulk LN. These devices have weak mode confinement, large device footprints, and reduced nonlinear efficiencies. As a result, LN devices have largely remained bulky, discrete components. This is in stark contrast to other major integrated photonic platforms, typically based on thin films supported by low-index cladding, which benefit from high-index-contrast and sub-wavelength optical confinement.

Followed by foundational works laid around the early 2000s [8–10], high-quality thin-film LN wafers prepared from ion slicing and wafer bonding have recently been made commercially available. With breakthroughs in fabrication techniques, ultra-low-loss, high-index-contrast, nanophotonic LN waveguides have been realized [11–20]. Within the past few years, a complete set of integrated optical components has been developed on the thin-film LN platform with unprecedented performance. Some notable examples include compact and ultra-high-performance modulators [21–25], broadband frequency comb sources [26–28], as well as record-efficiency wavelength converters [29–31] and photon-pair sources [32–34]. This versatile platform can host a wide variety of devices, as illustrated in Fig. 1, including various optical and optomechanical cavities, tunable filters, electro-optic modulators, acousto-optic modulators (AOMs), microwave-to-optical transducers, nonlinear wavelength converters, frequency combs, non-classical light sources, detectors,

and quantum memories. With such a rich component toolbox, we expect thin-film LN to become a material platform of choice for realizing multi-functional, high-performance integrated photonic circuits for both classical and quantum applications.

This review aims to present a comprehensive introduction of integrated photonics based on thin-film LN, from basic principles to the state of the art. In Section 2, we start by introducing the material properties of LN and basic passive optical components such as waveguides and cavities. In Section 3, we discuss electro-optics, from its most ubiquitous application in electro-optic modulators to the novel development of frequency combs, quantum transducers, and synthetic space photonics. Section 4 covers the diverse all-optical nonlinearities in thin-film LN, such as $\chi^{(2)}$-based wavelength conversion, Kerr comb generation, Raman lasing, and supercontinuum generation. In Section 5, we survey recent advances in integrated piezo-optomechanics (acousto-optics), which bridges optics, electronics, and mechanics. Section 6 describes recent efforts in heterogeneous integration that combine thin-film LN with other mature material platforms or unique functional components for both classical and quantum applications. In Section 7, we discuss challenges and opportunities, and provide an outlook. We hope this review, in conjunction with some other recent reviews on this topic [35–42], can give readers a starting point to delve into this exciting and rapidly advancing field.

2. MATERIAL AND INTEGRATED PASSIVE OPTICS

In this section, we give an overview of the material properties of LN and summarize how thin-film LN is prepared. We then review waveguides and cavities on the
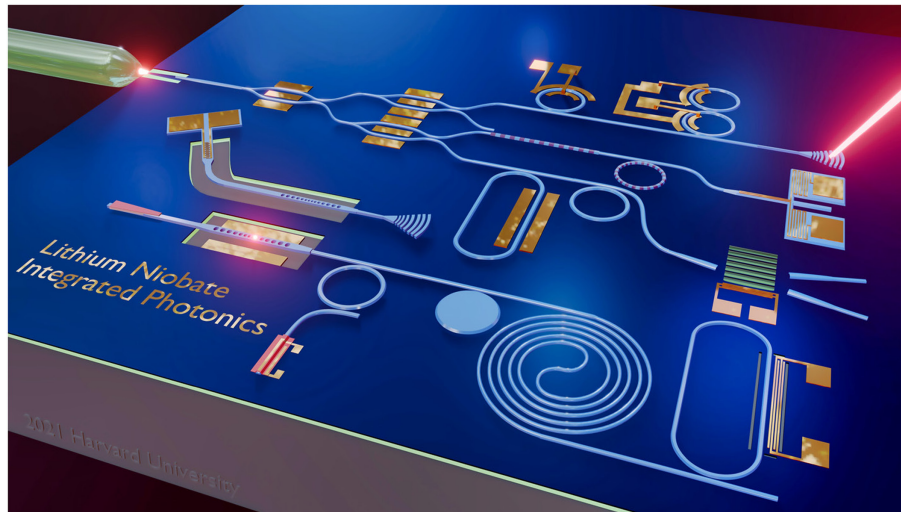
Integrated photonic devices on thin-film lithium niobate. The illustrated components include tapered waveguides and grating couplers, a spiral delay line, ring and microdisk resonators, photonic crystal cavities, an electro-optic frequency comb source, periodically poled waveguide and ring, a heterogeneously bonded laser source, an amorphous Si photodetector, Mach–Zehnder and in-phase/quadrature electro-optic modulators, an acousto-optic modulator, single- and coupled-ring modulators, a microwave-to-optical transducer, and an integrated single-photon detector as well as an emitter. Note that this figure only serves as a visual illustration of the wide range of devices that can be hosted on the platform. When integrating different categories of devices on a single chip, one may need to address practical fabrication issues to ensure process compatibility.

thin-film LN platform, which are the basis for various functional and active devices discussed in later sections.

2.1. Material Properties of Lithium Niobate

The study of material properties of LN traces back to the 1960s, and summaries of its physical properties can be found, for example, in Ref. [43,44]. The crystal structure of LN belongs to the $3m$ point group: it exhibits threefold rotation symmetry about the c axis, commonly defined as the Z axis, and mirror symmetry about three planes that are 60° apart (Fig. 2). In this review and most LN integrated photonics references, the X and Y axes are defined such that the LN crystal is mirror-symmetric about the YZ plane, as shown in Fig. 2(b). LN is a ferroelectric material [45]. Figure 2(a) depicts the relative positions of the lithium (Li) and niobium (Nb) atoms with respect to the oxygen (O) octahedra. Along the $+c$ axis, the octahedra is filled with Li, Nb, vacancy, Li, Nb, vacancy, and so on. A strong external electric field can relocate Li and Nb (cations), and move Li to the adjacent vacancy. This results in an inversion of ferroelectric domain orientation, which is the basis of periodic poling as used in quasi-phase matching (QPM).

In Table 1, we list some key material properties of LN and compare them to other popular materials used in integrated photonics. LN has a broad transparency window, from 350 nm to 5 μm, covering the visible, near-infrared, and mid-infrared wavelength ranges. Its relatively large refractive index ($\sim$2.2 at 1550 nm) allows high-index-contrast waveguides to be formed on top of most amorphous and crystal substrates (e.g., SiO_2 or sapphire). Its high Curie temperature ($\sim$1210°C) ensures a stable ferroelectric phase to render it compatible with a wide range of fabrication processes and operation conditions. Unlike Si and SiN_x, LN is a non-centrosymmetric crystal and possesses large second-order nonlinear coefficients ($d_{33} = -27$ pm/V). Combined with ferroelectric domain engineering, LN has been widely used for optical wavelength conversion and photon-pair generation. Crucially, LN's exceptional Pockels coefficient ($r_{33} \approx 31$ pm/V) has made it the material of choice for electro-optic (EO) modulators, which is at the core of telecommunication networks. LN also has a third-order nonlinear coefficient ($n_2 = 1.8 \times 10^{-19}$ m^2/W) that is comparable to other commonly used optical materials, making Kerr comb generation possible.

Figure 2
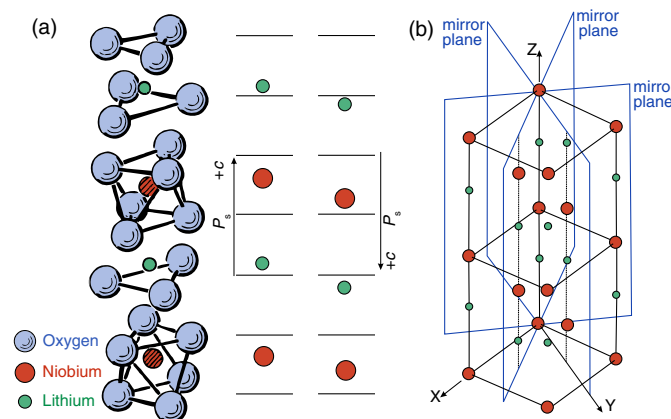
Crystal structure of lithium niobate. (a) Positions of lithium (Li) and niobium (Nb) atoms with respect to oxygen (O) octahedra in the ferroelectric phase. Poling moves the positions of Li and Nb, resulting in the inversion of the spontaneous polarization and domain orientation. (b) Standard definition of X, Y, and Z axes, where Y aligns with a mirror plane. Adapted from [43,45].

Table 1. List of Key Properties of Some Commonly Used Materials in Photonics[a]

Material	Symmetry Group	Optical Refractive Index[b]	RF Dielectric Constant	Second-Order Nonlinear Coefficient (pm/V)	Nonlinear Refractive Index, n_2 (m²/W)	EO Coefficient (pm/V)	Photoelastic Coefficients	Piezoelectric Strain Coefficient (pC/N)
LiNbO$_3$	$3m$	2.21 (o) 2.14 (e)	$\varepsilon_{11,22} = 44$ $\varepsilon_{33} = 27.9$ (clamped, high-frequency response)	$d_{31} = -4.3$ $d_{33} = -27.0$ $d_{22} = 2.10$ (at 1064 nm)	1.8×10^{-19} (at 1550 nm)	$r_{13} = 9.6$ $r_{22} = 6.8$ $r_{33} = 30.9$ $r_{51} = 32.6$	$p_{11} = -0.026$ $p_{12} = 0.09$ $p_{13} = 0.133$ $p_{14} = -0.075$ $p_{31} = 0.179$ $p_{33} = 0.071$ $p_{41} = -0.151$ $p_{44} = 0.146$	$d_{31} = -1.0$ $d_{22} = 21$ $d_{33} = 16$ $d_{15} = 74$
LiTaO$_3$	$3m$	2.119 (o) 2.123 (e)	$\varepsilon_{11,22} = 38.3$ $\varepsilon_{33} = 46.2$	$d_{31} = 0.85$ $d_{33} = 13.8$ (at 1064 nm)	1.46×10^{-19} (at 800 nm)	$r_{13} = 8.4$ $r_{22} = -0.2$ $r_{33} = 30.5$ $r_{51} = 20$	$p_{11} = -0.081$ $p_{12} = 0.081$ $p_{13} = 0.093$ $p_{14} = -0.026$ $p_{31} = 0.089$ $p_{33} = -0.044$ $p_{41} = -0.085$ $p_{44} = 0.028$	$d_{31} = -3.0$ $d_{22} = 9.0$ $d_{33} = 9.0$ $d_{15} = 26$
Si	$m3m$	3.48	11.7	0	5×10^{-18} (at 1550 nm)	0	$p_{11} = -0.094$ $p_{12} = 0.017$ $p_{44} = 0.051$	0
SiO$_2$	Amorphous	1.44	3.9	0	3×10^{-20} (at 1550 nm)	0	$p_{11} = 0.121$ $p_{12} = 0.270$	0
α-Quartz	32	1.53 (o) 1.54 (e)	3.8	$d_{11} = 0.584$ (at 1318 nm)	2.6×10^{-20} (at 1318 nm)	$r_{41} = 0.2$ $r_{62} = 0.93$	$p_{11} = 0.16$ $p_{12} = 0.27$ $p_{13} = 0.27$ $p_{14} = -0.03$ $p_{31} = 0.29$ $p_{33} = 0.10$ $p_{41} = -0.047$ $p_{44} = -0.079$	$d_{11} = 2.3$ $d_{14} = -0.67$
Si$_3$N$_4$	Amorphous	2.00	7.5	0	2.5×10^{-19} (at 1550 nm)	0	$p_{12} = 0.047$	0
AlN	$6mm$	2.12 (o) 2.16 (e)	8.6	$d_{31} = 1.6$ $d_{33} = 4.7$ (at 1550nm)	2.3×10^{-19} (at 1550 nm)	$r_{13} = 0.67$ $r_{33} = -0.59$ (sputtered thin film)	$p_{11} = -0.1$ $p_{12} = -0.027$ $p_{13} = -0.019$ $p_{33} = -0.107$ $p_{44} = -0.032$ $p_{66} = -0.037$	$d_{31} = -2.0$ $d_{33} = 5.0$ $d_{15} = 4.0$
ZnO	$6mm$	1.93 (o) 1.94 (e)	10.4	$d_{33} = 1.23$ (at 1064 nm)	6.88×10^{-15} (ZnO:Ni thin film, at 1064 nm)	$r_{33} = 0.5$ (ZnO:Mn thin film) $r_{33} = 2.6$ (single crystal)	$p_{11} = 0.222$ $p_{12} = 0.099$ $p_{13} = -0.111$ $p_{31} = 0.0888$ $p_{33} = -0.0235$ $p_{44} = 0.0585$	$d_{31} = -5.1$ $d_{33} = 12.4$ $d_{15} = -8.3$
GaAs	$\bar{4}3m$	3.38	12.9	$d_{36} = 170$ (at 1064 nm)	2.6×10^{-17}	$r_{41} = 1.43$ (at 1550 nm)	$p_{11} = -0.165$ $p_{12} = -0.140$ $p_{44} = -0.072$	$d_{14} = 2.6$
Diamond	$m3m$	2.39	5.7	0	4×10^{-20} (at 800 nm)	0	$p_{11} = 0.125$ $p_{12} = -0.325$ $p_{44} = 0.11$	0

[a]From a variety of sources and some data may be incomplete. Discrepancies exist in the literature due to material composition, physical form, and growth method/condition.

[b]Linear optical refractive indices are given at 1550 nm, with o/e denoting ordinary/extraordinary axis.

Considering acoustic applications, the speed of sound on the surface of bulk LN or inside thin-film LN is ~4 km/s, resulting in a higher acoustic index than SiO_2 and sapphire. This means that the thin-film LN platform is able to guide not only photons, but also phonons. Combining this with large piezoelectric coefficients (for example, $d_{22} = 21$ pC/N and $d_{33} = 16$ pC/N for Rayleigh waves, and $d_{15} = 74$ pC/N for shear waves) and photoelastic coefficients (e.g., $p_{13} = 0.133$ and $p_{44} = 0.146$) of LN, it is possible to realize a wide variety of novel piezo-optomechanical devices, in addition to more traditional surface-acoustic-wave (SAW) microwave filters. Finally, LN has thermo-optic ($\frac{dn_e}{dT} = 3.34 \times 10^{-5}$ K^{-1} at 1523 nm and 300 K [46]), pyroelectric (~95 μCm^{-2} K^{-1} [47]), and photorefractive effects. They may be leveraged to provide additional functionalities and engineering knobs, such as wavelength tuning of modulators and resonators, but may also cause detrimental effects and limit device operation (especially for photorefraction; see Subsection 7.1).

2.2. Thin-Film Lithium Niobate

While traditional diffusion-based photonic devices in bulk LN have played an important role in optical and RF signal processing, they have several critical limitations, predominately originating from the large optical mode due to the low index contrast. For example, EO modulators realized using this approach require large drive voltages and challenging RF-optical dispersion engineering. Furthermore, it is impossible to make tight bends in these waveguides, which prevents the realization of, for example, low-loss ring or racetrack resonators. These limitations, along with the desire to integrate many different functionalities on the same LN chip, motivated the production of thin-film LN-on-insulator (LNOI) wafers.

Historically, the realization of high-quality LN thin films has proven difficult. Various methods have been explored, including chemical vapor deposition [48], RF sputtering [49], pulsed laser deposition [50], sol-gel [51], and molecular beam epitaxy [52]. However, these approaches have failed to produce highly crystalline materials, and lattice matching requirements severely limit the substrate options for epitaxial growth [35].

The development and refinement of the "Smart-Cut" technology [53], commonly used to generate SOI wafers, has emerged as the standard technique for producing high-quality LN thin films [35,54]. The use of crystal ion slicing to prepare thin-film LN started in the late 1990s [8] and early 2000s [10], including a patent that was filed in 1998 and that expired in 2018 [9]. Instead of making a thin film using deposition or growth methods, the film is split from a high-quality bulk substrate through ion slicing and thermal annealing, and is bonded to an insulating substrate, typically through adhesive (e.g., using benzocyclobutene, BCB) [55] or direct wafer bonding [10]. However, while both BCB and direct bonding techniques have succeeded in producing single-crystalline LNOI, the direct bonding method is preferred for many applications, as the higher annealing temperatures allowed by the process are necessary for recovering nonlinear and electro-optic properties of the ion-sliced material [35].

The Smart-Cut fabrication process for LNOI is illustrated schematically in Fig. 3. From a high-quality LN substrate, a cleavage plane is first defined at the desired film thickness via high-dose implantation of He$^+$ (or H$^+$) ions. In parallel, the substrate wafer, usually LN or Si with an oxide layer, is prepared. After the LN substrate is bonded to the wafer, thermal annealing is used to split the substrate along the cleavage plane, defining the thin film. Additional annealing reduces ion-implantation-induced crystal defects, and polishing improves surface smoothness. It is important to note that most LNOI fabrication is performed using congruent rather than stoichiometric LN, meaning that the crystals are lithium deficient [44].

Through the use of ion slicing with direct wafer bonding, large-area, single-crystalline LN thin films on SiO$_2$-on-LN substrates were demonstrated [56,57]. This fabrication method can also be employed to produce other high-quality ferroelectric thin films, as well as more exotic iterations of thin-film LNOI, such as doped and stoichiometric LN wafers. Currently, LNOI wafers with sizes up to 6 in. have been made commercially available from companies such as NanoLN, Partow Technologies, NGK Insulators, and SRICO.

2.3. Waveguides

Waveguides are the backbone of integrated photonic circuits. In this subsection, we summarize how waveguides are formed in thin-film LN (Fig. 4). Throughout the text, we use "bulk" to refer to diffusion-based waveguides in bulk LN [Fig. 4(a)]. For thin-film devices, we use the term "monolithic" to describe devices realized by direct etching [Fig. 4(b)]. This is to differentiate from "hybrid" devices based on rib loading or heterogeneous bonding [Figs. 4(c) and 4(d)], which involve additional materials other than the LNOI substrate and any cladding materials. Furthermore, terms such as thin-film lithium niobate (TFLN) and thin-film lithium niobate on insulator (TFLNOI) are often used in the literature. They are, in most cases, interchangeable with LNOI.

2.3a. Weakly Guiding Diffused Waveguides in Bulk LN

Traditional LN waveguides are often based on titanium (Ti) in-diffusion or proton exchange [36]. Ti in-diffused waveguides are formed by depositing Ti strips on bulk LN substrates followed by thermal annealing. Ti diffuses into LN crystals with a typical diffusion length of a few micrometers. The presence of Ti ions causes an increase in the optical refractive index ranging from 0.001 to 0.04, depending on Ti density. Proton-exchange waveguides are formed by immersing LN into a liquid source of hydrogen. At moderate temperatures (between 150 and 400°C), protons (H$^+$) replace lithium ions (Li$^+$), causing a refractive index change (only in the extraordinary direction, Δn_e) around 0.1 or less. Further improvement of the waveguide quality could be achieved by a reverse-proton-exchange (RPE) process, which re-diffuses Li$^+$ ions into the top layer of the crystal, leading to a more symmetric optical mode. Such index perturbation-based waveguides can also be formed by ion implantation [58] and femtosecond laser writing [59]. A major drawback of these waveguides is the low index contrast, resulting in weak optical confinement (mode area of 10 to 100 μm^2) and

Figure 3
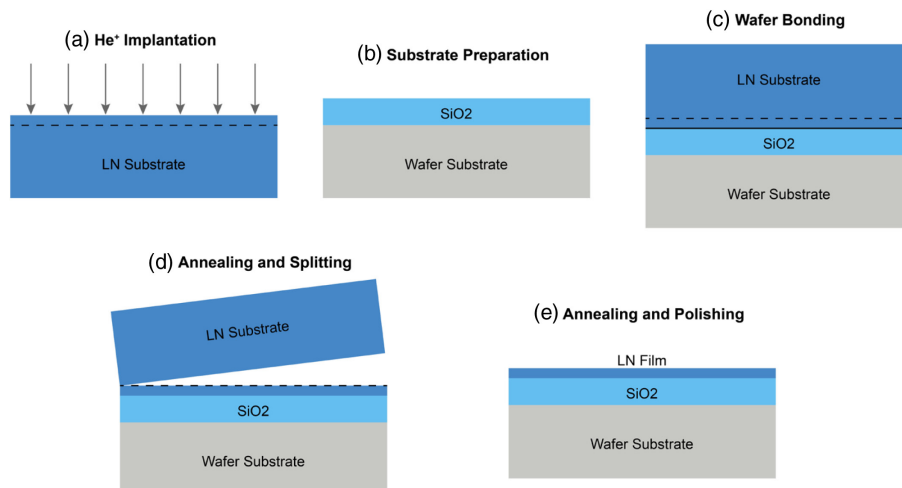
Schematic of the Smart-Cut process for a LNOI wafer.

large bending radius (millimeter). They are therefore unsuitable for dense integration, unable to realize microresonators, and challenging to perform dispersion engineering.

2.3b. Monolithic Ridge/Rib Waveguides on Thin-Film LN

The availability of thin-film LNOI facilitates the fabrication of monolithic ridge waveguides with large index contrast (roughly an order of magnitude larger than ion-diffused waveguides) and strong mode confinement. Figure 4(b) shows the cross section of a typical LNOI rib waveguide with slanted sidewalls and a slab (due to limitations in the dry etching process as discussed later). The slab is desirable in, for example, electro-optical modulators, since it increases the microwave field inside LN. Furthermore, it can help reduce overlap of the optical mode with etched surfaces, and thus reduce optical losses.

To avoid dry etching, LN can be processed by mechanical means. Ridge waveguides using optical-grade diamond blade dicing [60–63] have been demonstrated [Fig. 5(a)]. Diced waveguides can achieve high aspect ratios (>10 [62]) and low optical loss (<1 dB/cm [14]), but are challenging for the realization of complex shapes such as couplers, crosses, and tapers. Chemical-mechanical (chemomechanical) polishing (CMP) has also been employed to fabricate ridge waveguides on thin-film LNs [Fig. 5(b)] [12,64–67]. A typical process [12] involves (1) Cr deposition, (2) patterning the Cr mask through femtosecond laser ablation, (3) removing uncovered LN through CMP, and (4) Cr removal. The CMP process yields waveguides with sub-nanometer surface roughness and propagation losses as low as 0.027 dB/cm [12]. Arrays of beam splitters and Mach–Zehnder interferometers (MZIs) have also been demonstrated using this process [65,66], making future large-scale photonic integrated circuits (PICs) possible. One problem with CMP-based LN waveguides is that they have shallow sidewalls, limiting the minimum bending radius. LN can also be wet etched (e.g., using HF:HNO$_3$ solution) [68], and the LNOI waveguide has been

Figure 4
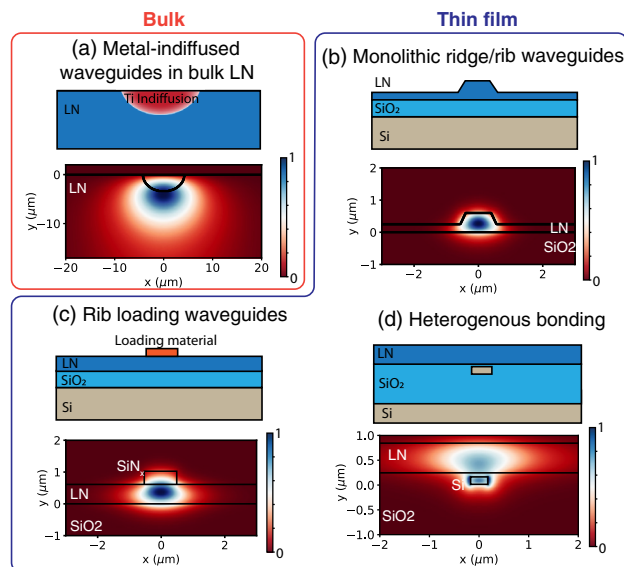
Major waveguide types in LN and their typical mode distribution. (a) Metal-indiffused waveguide in bulk LN (similar for proton-exchanged waveguides). The boundary of the waveguide core in the lower panel indicates diffusion length; actual index variation extends beyond that. (b) Monolithic ridge/rib waveguides in thin-film LN. (c) Rib-loaded waveguides. (d) Heterogeneously bonded thin-film LN on photonic integrated circuits made from other materials.

demonstrated using ion-beam-enhanced KOH etching [69,70]. Furthermore, waveguiding in thin-film LN using proton exchange [71–73] and helium ion implantation [74] has been reported. These waveguides have relatively low index contrast and mode confinement in the lateral direction despite their relatively small mode volume compared to their bulk counterparts. In addition, proton exchange tends to degrade EO and nonlinear coefficients [72,75].

Compared to mechanical dicing/polishing and wet etching, dry etching is much preferred for integrated photonics. It is anisotropic, well-controlled in etch depth, able to transfer complex 2D patterns, and compatible with multi-layer processing. However, dry etching of LN had been notoriously difficult. Unlike most other integrated photonics platforms such as Si and SiN_x, a proper reactive ion-etching recipe was not available for LN. Fluorine-based reactive-ion etching (RIE) can remove LN effectively by forming volatile, fluorinated niobium (Nb) species [77]. However, it also forms lithium fluoride (LiF), which is non-volatile, and results in severe redeposition problems [78]. This effect is less critical in proton-exchanged waveguides due to low Li contents [77,79,80] but problematic for thin-film LN waveguides. LiF is highly resistive to further etching, and thus increases sidewall roughness and scattering loss. Early on, focused ion-beam milling was also used to pattern LN [81,82]. They are suitable for defining small and sparse patterns such as photonic crystals; however, this technique is not time-efficient for larger patterns or wafer-scale fabrication.

Currently, pure physical etching with Ar^+ plasma (or Ar^+ milling) [83] is among the most popular dry etching approaches for LNOI. It can be carried out with different tools, such as inductively coupled plasma (ICP), electron-cyclotron resonance (ECR), or ion-beam etch (IBE) systems. There are a few challenges associated with pure physical etching. First, it has low etch selectivity with respect to the available lithography resists (usually around 1:1), resulting in limited etch depth. Though shallow-etched LNOI can also support guided modes [84], deep-etched waveguides would have tighter mode confinement. Commonly used hard masks include amorphous Si [85] and Cr [86]. Various photo or electron-beam resists are also used as etch masks, such as hydrogen silsesquioxane (HSQ) [11,15,87], Zeon electron-beam positive-tone resist (ZEP) [27,88], CSAR [87], SU8 [55], and even the positive-tone UV-lithography photoresist [89]. The other challenge with Ar^+ etching is that it forms nonvertical sidewalls due to redeposition. Unlike LiF redeposition (which is in the form of particles and clusters), LN redeposition from Ar^+ etching can be smooth and does not introduce large scattering loss. Furthermore, it can be removed

Figure 5
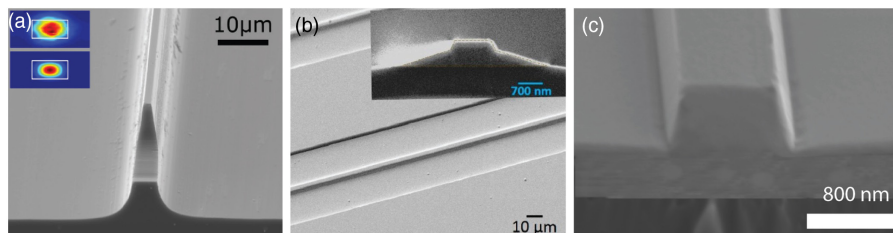
Monolithic LNOI ridge/rib waveguides. (a) Precision-diced waveguide (top and bottom insets show measured and simulated fundamental TE mode, respectively) [60], (b) chemical-mechanical polished waveguides (inset shows waveguide cross section) [64], and (c) dry-etched waveguide [76]. (a) Reprinted with permission from [60]. Copyright 2015 Optical Society of America. (b) Reprinted with permission from Lin *et al.*, Micromachines (Basel) **10**, 612 (2019) [64] under open access license. (c) Reprinted with permission from [76]. Copyright 2019 Optical Society of America.

using wet chemistry, after the dry etch process is finished, to further reduce optical losses. Nonetheless, the purely mechanical nature of the etch results in an "over-cut" waveguide profile with a trapezoidal cross section. The sidewall angle, typically in the 40°–80° range, ultimately limits the minimum feature size and spacing between neighboring structures. Lower vacuum pressure and higher plasma power generally produce steeper sidewalls. Some processes introduce fluorine (F) gases such as CHF_3 [86], aiming to improve the sidewall angle. Also, wet chemical cleaning can help remove redeposition and other contaminants, and reduce sidewall roughness [89–91].

Besides etching, waveguide fabrication also requires lithography and post-processing. Lithography can be done by either photo- or electron-beam lithography. Since LN is insulating, it commonly experiences significant charging during electron-beam lithography, which can be addressed using a spin-coated aqueous, conductive solution (e.g., Espacer™), or a thin layer of a metallic element (e.g., Cr). Post-processing may include several steps such as acid/solvent cleaning, thermal annealing, polishing, and oxide cladding.

With the optimization of lithography, etching, and post-etch cleaning, the propagation loss of dry-etched LNOI waveguides has improved from $> 6\,dB/cm$ [55] in 2007 to $0.027\,dB/cm$ in 2017 [11]. Devices with optical loss below $0.1\,dB/cm$ can now be routinely produced by several groups, making LNOI a reliable and scalable low-loss platform for integrated photonics. However, these values are still beyond the material absorption rate measured in whispering gallery resonators made from bulk congruent LN ($<0.4\,dB/m$ [92,93]). The major loss mechanism in the dry-etched LNOI waveguide is the contribution from sidewall roughness. Various methods have been reported to reduce surface roughness, including CMP [13,94] and gas clustered ion-beam smoothening [19]. Alternatively, one can design the waveguide cross section so that the mode is more confined in the core and less exposed to the sidewalls using a wide and thin waveguide [95]. Finally, we note that the impact of ion implantation, used for ion slicing, on the intrinsic material losses is not fully understood at the moment.

2.3c. Hybrid Waveguides

Another class of waveguides on thin-film LN is the rib-loaded waveguide, which avoids the necessity of LN etching. In this category, a strip of material is deposited/patterned on top of the unetched LN thin film, as shown in Figs. 6(a)–6(c). The patched material usually has a refractive index that is similar to or higher than that of LN but is easier to deposit and etch. This way, an effective rib waveguide is formed, where part of the optical mode is confined in the LN slab and can access its unique material properties. Various loading materials have been used, including SiN_x [17,25,96–99], TiO_2 [100,101], chalcogenide glass [102], Ta_2O_5 [103], and Si [104,105]. Recently, it has been demonstrated that the loading ridge can also be low-index material (e.g., photo- or electron-beam resist) [106,107]. Different from standard rib-loaded waveguides, this approach is based on the concept of bound states in the continuum (BIC), where waveguiding is achieved by destructive interference of all leakage channels [108]. BIC waveguides, however, only guide light in specific polarizations and wavelengths.

It is also possible to bond LN to PICs made from other mature material platforms, such as Si_3N_4 [110] and Si [23,109,111–114]. A subtle but important difference between the rib-loading and bonding approach is that LN is the main host material in the former but a stamping/subsidiary material in the latter. These hybrid approaches represent a promising path towards heterogeneous integration of LN with other PIC platforms, complementing their missing functionalities such as EO modulation,

second-order nonlinearity, and the ability of QPM. One disadvantage, however, is that only a portion of the optical mode is in the LN, which results in weaker nonlinear and EO interactions.

Figure 7 summarizes the propagation losses of different types of LNOI waveguides reported in the literature. Low-loss waveguides with propagation losses below 1 dB/cm were made possible since 2015 using multiple methods, and a few dB/m can now be achieved using dry etching and chemo-mechanical polishing.

2.3d. Fiber-to-Chip Coupling

The tight optical confinement of LNOI waveguides drastically reduces the device footprint and enhances nonlinear-optical interactions. It, however, presents a significant challenge in optical packaging due to the mode mismatch between the waveguides and standard optical fibers. In order to create an efficient interface between the optical fibers and the chip, two common schemes, namely end-fire coupling (also called butt-coupling) and grating coupling, have been widely studied (see Fig. 8).

Figure 6
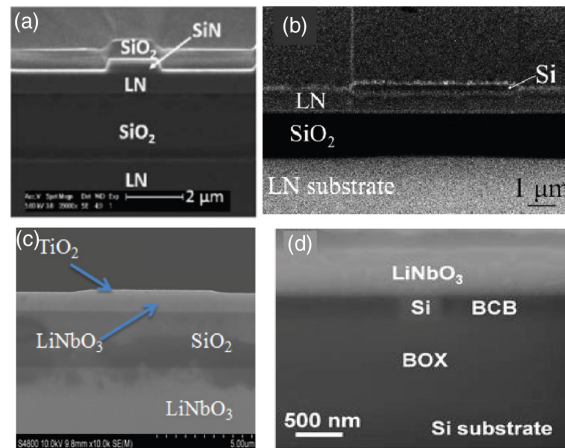
Hybrid waveguides on LN. (a)–(c) Rib-loaded waveguide in LNOI using SiN_x [17], Si [100], and TiO_2 [104], respectively. (d) LN thin film bonded on SOI waveguide [109]. Reprinted with permission from [17,100,104,109]. Copyright 2016, 2015, 2017, 2012 Optical Society of America.

Figure 7
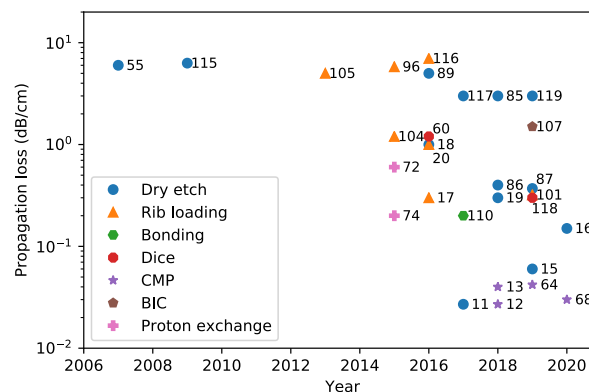
Propagation loss of various waveguides on thin-film LN. References: [11–20,55,60,64,67,71,73,85–87,89,98,100,102,103,106,110,115–118].

End-fire coupling can be performed by aligning a lensed fiber to a diced/polished or etched facet of the waveguide. This approach is broadband and can work for any polarizations. However, due to the mismatch between the spot size of the lensed fiber (~2 μm diameter) and waveguide mode (~1 μm), typical fiber-to-chip coupling efficiencies are between −4 and −6 dB [32]. To mitigate this problem, a mode converter in the form of an inverse taper can be used to expand the waveguide mode at the facet [119,122–127]. Since a typical LNOI rib waveguide has a profile that consists of a trapezoidal ridge on top of a slab, single-step tapering will only reduce the ridge width, which pushes the optical mode to the slab instead of expanding it symmetrically into the cladding, and in fact reduces coupling efficiency. Thus, two-step tapering is needed. This is accomplished by tapering down both the rib and the slab that gradually pushes the mode to the oxide cladding. Using this approach, fiber-to-chip coupling loss of 1.7 dB per facet has been achieved [119] [see Fig. 8(a)]. More recently, fiber-to-chip coupling loss as low as 0.54/0.59 dB per facet for the TE/TM mode has been demonstrated by adding a SiON cladding waveguide to the LNOI adiabatic taper [127].

Grating couplers allow vertical coupling at arbitrary positions of the chip with relatively large alignment tolerance. However, their operation bandwidth is narrow, and they are sensitive to polarization. Grating couplers are therefore convenient for rapid testing of large arrays of linear-optical devices (including optical modulators) at wafer scale, but not well suited for the characterization of most nonlinear devices that involve multiple wavelengths and polarizations. There have been a number of reports on LNOI grating couplers [120,128–133], with a current record coupling efficiency as low as −3.5 dB per coupler [120] [see Fig. 8(b)]. Two unique problems of LNOI grating couplers are (1) the anisotropy of LN causes orientation-dependent coupling and (2) the nonvertical sidewall angle in dry etching limits the minimum pitch size and fill factor of the gratings. On the other hand, bonded LNOI has the unique advantage that it allows buried metal layers, which can serve as an efficient optical reflector to minimize downward coupling and improve coupling efficiency [128,129]. Besides

Figure 8
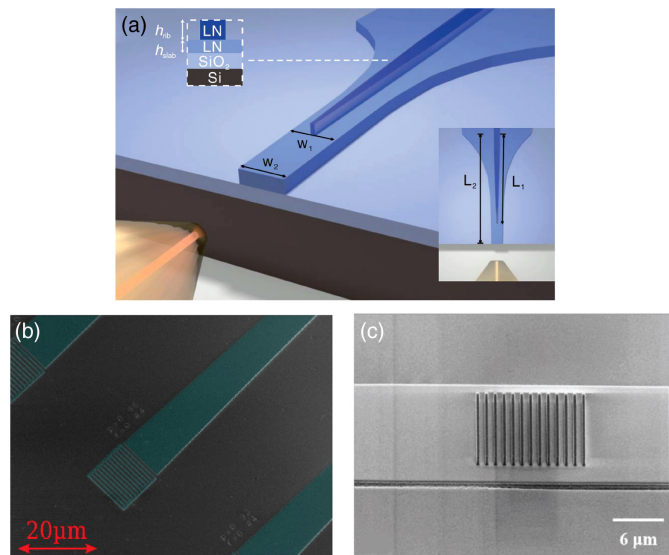
Fiber-to-chip coupling. (a) End-fire coupling through a mode converter with two-step tapering. (b) Thin-film LN grating coupler. (c) Hybrid amorphous Si grating on LN waveguide. (a)–(c) Reprinted with permission from [119–121]. Copyright 2019, 2019, and 2018 Optical Society of America.

monolithically etched LN gratings, another promising approach is to pattern hybrid gratings on top of the LNOI waveguide using, for example, amorphous Si [16,121]. Si gratings have a larger refractive index and allow finer and sharper structures, alleviating the limitations imposed by LN etch. This approach has demonstrated coupling efficiency as high as ~ -3 dB per coupler with a 1-dB bandwidth of 55 nm [121] [see Fig. 8(c)].

Beyond what has been demonstrated on the LNOI platform, approaches that have been explored on other material platforms such as adiabatic tapered fibers [134,135], apodized [136], angled-etched [137], or multi-layer gratings [138] may be adapted to further improve fiber-to-chip coupling efficiencies. In addition, for hybrid systems, it is possible to adiabatically couple the optical mode from LN to, for example, Si [22] or SiN$_x$ [110] waveguides, and leverage the rich optical packaging toolbox developed for those platforms to achieve efficient coupling [139].

Fiber-to-chip coupling is a ubiquitous problem shared by all high-index-contrast integrated photonic platforms. As LNOI devices move forward from proof-of-concept demonstrations to mission-critical products, we anticipate that this optical packaging problem can be collectively addressed by the academic community as well as commercial sectors.

2.4. Cavities

Optical microcavities are another set of essential components for integrated photonics. They enable wavelength filtering and strongly enhance nonlinear-, electro-, and acousto-optic interactions. In this subsection, we briefly review the state of the art of optical cavities on thin-film LN, including microdisks, rings and racetracks, and photonic crystals (see Fig. 9).

2.4a. Microdisk

On-chip microdisks support whispering gallery modes with ultra-high quality factors (Q-factors) and compact mode volumes. Thanks to their high Q-factors, they

Figure 9
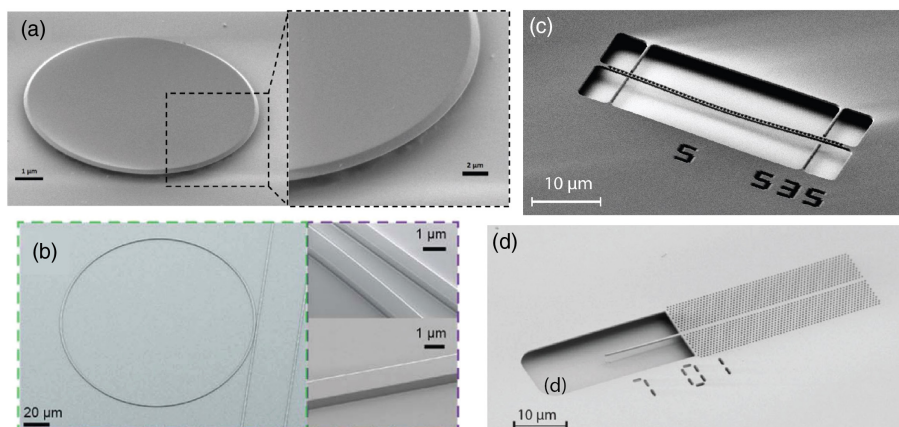
Optical microcavities based on thin-film LN. (a) Microdisk [140], (b) microring [11], (c) 1D photonic crystal cavity [141], and (d) 2D photonic crystal cavity [142]. (a)–(c) Reprinted with permission from [11,140,141]. Copyright 2014, 2017, 2017 Optical Society of America. (d) Li *et al.*, Laser Photon. Rev. **13**, 1800228 (2019) [142]. Copyright 2019 Wiley-VCH Verlag GmbH & Co. KGaA. Reprodued with permission.

have been widely used for nonlinear optics, cavity quantum electrodynamics, and optomechanics.

The fabrication of microdisk resonators in thin-film LN has been achieved by dry etching (highest Q-factor $\sim 10^6$) [18,140,143,144], femtosecond laser ablation followed by FIB sidewall milling and high-temperature annealing (highest Q-factor $\sim 10^7$) [145–150], direct FIB milling (Q- factor $\sim 10^5$) [151], or CMP (highest Q- factor $\sim 10^7$) [152–154]. On LNOI substrates, the LN microdisk can be easily suspended/undercut by removing the buried oxide using HF [see Fig. 9(a)]. It is also possible to fabricate suspended microdisks on bulk LN by chemically etching a buried layer of damaged lattice induced by ion implantation [155]. Besides single-crystal LN, microdisks made of polycrystalline LN deposited by pulsed laser deposition on a Si substrate have also been reported, showing a Q-factor of 3.4×10^4 that is likely limited by the polycrystal itself [156].

It is worth noting that mechanically polished, millimeter-scale disk resonators made from pristine bulk LN crystals have shown Q-factors as high as 2×10^8 [93], an order of magnitude higher than what has been demonstrated in thin-film LN. This indicates that the current cavity Q-factors using the LNOI platform are likely still largely limited by surface scattering. Another reason could be the induced damages resulting from the ion-slicing process used in thin-film LN production, which may result in higher material-limited loss.

LNOI microdisks have enabled various demonstrations ranging from electro-optic modulators [144] and nonlinear wavelength converters [140,146,149–152,156–163] to cavity optomechanics [164]. Some of these demonstrations will be discussed in later sections.

2.4b. Microring and Racetrack

Microring and racetrack resonators are formed by waveguide loops and support cleaner resonance modes than microdisks due to the suppression of higher-order radial modes. They follow the same fabrication procedure as waveguides, and their intrinsic Q-factors directly reflect the propagation losses of the waveguide. Therefore, microring/racetrack resonators are often used as an accurate way of measuring waveguide losses, especially when the loss is low. Excluding bending loss, the intrinsic Q-factor follows $Q_i = \frac{2\pi n_g}{\lambda \alpha}$, where n_g is the group velocity, λ is the free-space wavelength, and α is the propagation loss. The free-spectral range (FSR) of the resonance can be used to calculate $n_g = \lambda^2/(\text{FSR} \cdot L)$, where L is the cavity length. In addition, the intrinsic Q of the resonator is related to the measured loaded Q-factor by $Q_i = 2 Q_l/(1 \pm \sqrt{T_0})$, where T_0 is the normalized transmission, and $+$ and $-$ correspond to the under- and over-coupled regimes, respectively. At critical coupling, $T_0 = 0$ and $Q_i = 2 Q_l$.

On the LNOI platform, microring and racetrack resonators have been fabricated by dry etching [see Fig. 9(b)] [11,15,28,55,85,88,165], rib loading [102,103], CMP [12], as well as using BIC waveguides [106]. The state-of-the-art quality factors of these resonators are listed in Table 2, with the highest intrinsic Q-factor achieved to date $\sim 10^7$. Furthermore, resonators have enabled low-voltage EO modulators [55,85,166], broadband EO frequency comb generation [26], ultra-efficient parametric wavelength conversions [30,31,94,167–170], and Kerr comb generation [27,28,171,172]. Coupled rings combined with EO modulation have also been explored to form a photonic molecule [173], and have found applications in frequency shifting [174] as well as microwave-to-optical photon conversion [175,176]. Details of these applications will be discussed in later sections.

2.4c. Photonic Crystal

Photonic crystal (PhC) cavities simultaneously possess high *Q*-factor and wavelength-scale mode volume, which enhance optical nonlinearities and reduce the physical footprint. In 2013, Diziain *et al*. demonstrated second-harmonic generation (SHG) in suspended 2D photonic crystals fabricated from bulk LN by FIB and wet etching of an ion-damaged buried layer [178]. On LNOI substrates, both 1D and 2D photonic crystal cavities have been demonstrated [see Figs. 9(b) and 9(d)] [141,142,177,179,180]. With small mode volume and large local field intensity, photorefractive effects (discussed in Section 7) are enhanced to the extreme, enabling photon-level tuning of cavity resonances [181]. As a cavity, it also allows resonant EO modulation [182], with the advantage of reduced electrode size and thus higher RC-limited operating frequency. In addition, optomechanical crystals [141,177,180] that confine both optical and mechanical modes have been demonstrated on suspended LN thin films.

3. ELECTRO-OPTICS

The electro-optic (EO) effect is perhaps the most attractive property of LN. This effect directly mixes optical and RF fields, enabling optical modulation, sideband generation, and frequency shifting in the gigahertz range. Low-loss ridge waveguides with closely placed microwave electrodes, strong field confinement, and high-quality resonators in thin-film LN drastically improve the EO interaction strength. In recent years, we have seen a proliferation of works on EO modulators in LN, based on both non-resonant and resonant optical structures, pushing towards wider microwave bandwidth and lower half-wave voltages. Such efficient EO interaction has also enabled EO frequency combs, which are of interest for applications in spectroscopy and topological photonics. In quantum applications, EO-based frequency conversion serves as a promising candidate to link microwave photons (e.g., in superconducting quantum systems) and optical photons (for long-haul networks). In addition, time modulation enables the study of synthetic dimensions in the frequency domain. This section covers EO optical modulators, EO frequency comb sources, coupled-ring modulators (photonic molecules), cavity EO for quantum transduction, as well as EO-modulation-based synthetic photonics.

Table 2.   State-of-the-Art *Q*-Factors of Some Representative Optical Cavities in the Thin-Film LN Platform, Noted by Their Cavity Type and Fabrication Method

Cavity Type	Fabrication Method	Q-factor $(10^6)^a$	Year	Ref.
Microdisk	Dry etched	1.70	2017	[158]
Microdisk	Femtosecond laser + FIB	9.61	2019	[150]
Microdisk	CMP	14.6	2018	[152]
PPLN microdisk	Dry etching, piezo-force-microscopy poling	8.0	2020	[161]
Microring	Rib-loaded	0.13	2015	[102]
Microring	Dry etch	10	2017	[11]
Microring at visible wavelength	Dry etch	11	2019	[15]
Microring	BIC	0.577	2019	[106]
Microring	CMP	11.4	2018	[12]
PPLN ring	Dry etched, Z-cut poling	1.8	2020	[167]
PPLN racetrack	Dry etched, X-cut poling	0.37	2019	[30]
Ring-shaped WGR	Dry etch followed by CMP	3.0	2017	[94]
PPLN ring-shaped WGR	Dry etch followed by CMP, Z-cut poling	1.3	2018	[168]
Photonic crystal	Dry etch	0.109	2017	[141]
Piezo-optomechanical crystal	Dry etch	0.47	2020	[177]

^{a}Intrinsic *Q*-factors are cited when available.

3.1. Basic Formulation of Electro-Optic Modulation

We first summarize some basic formulation to describe the linear EO effect. The linear EO strength in a material is described using the Pockels tensor, $\bar{\bar{r}}$. It relates the applied DC/RF electric field to the change in the inverse permittivity tensor, or impermeability tensor, by $\Delta(\frac{1}{n^2})_{ij} = \sum_k r_{ijk} E_k$, where i, j, and k can take values of 1 to 3, corresponding to the x, y, and z crystal directions. Because of the symmetry property, $r_{ijk} = r_{jik}$, a contracted index notation is usually used: $r_{ijk} \equiv r_{Ik}$, with $I = 1, \cdots, 6$ [183]. The correspondence between I and ij, as well as the matrix form of r_{Ik} with symmetry reduction for LN (point group $3m$), are listed in Eq. (1):

$$r_{Ik} = \begin{bmatrix} 0 & -r_{22} & r_{13} \\ 0 & r_{22} & r_{13} \\ 0 & 0 & r_{33} \\ 0 & r_{42} & 0 \\ r_{42} & 0 & 0 \\ -r_{22} & 0 & 0 \end{bmatrix} \text{ with } I = \begin{cases} 1 & \text{for } ij = 11 \\ 2 & \text{for } ij = 22 \\ 3 & \text{for } ij = 33 \\ 4 & \text{for } ij = 23 \text{ or } 32 \\ 5 & \text{for } ij = 13 \text{ or } 31 \\ 6 & \text{for } ij = 12 \text{ or } 21 \end{cases}. \tag{1}$$

In integrated photonics, modulation strengths are often calculated using coupled-mode theory from index perturbations. Thus it is often more convenient to directly express the permittivity change as a function of the applied electric field: $\Delta \epsilon_{ij} = -\sum_k \epsilon_{ii} \epsilon_{jj} r_{ijk} E_k / \epsilon_0$ [184,185].

In LN modulators, the strongest and most utilized EO coefficient is r_{33} (~ 31 pm/V), which induces an index change along the Z crystal axis when the E-field is applied along z as well. Note that LN is anisotropic and Z is the extraordinary axis ($n_{33} = n_e = 2.14$ and $n_{11} = n_{22} = n_o = 2.21$ at 1550 nm). The induced permittivity change along z is $\Delta \epsilon_z = -n_e^4 \epsilon_0 r_{33} E_z$, and the refractive index change is approximately $\Delta n \approx -1/2 \, n_e^3 r_{33} E_z$. Most of the devices reviewed in this section use r_{33}.

Another noteworthy but less exploited EO coefficient is $r_{51} = r_{42} \approx 30$ pm/V. It causes deformation of the index ellipsoid in the xz or yz crystal plane when the DC/RF field is applied along x or y, respectively. The permittivity change under such modulation follows $\Delta \bar{\bar{\epsilon}} = -\epsilon_0 r_{42} n_0^2 n_e^2 E_y \begin{bmatrix} 0 & 0 & 0 \\ 0 & 0 & 1 \\ 0 & 1 & 0 \end{bmatrix}$ or $-\epsilon_0 r_{51} n_0^2 n_e^2 E_x \begin{bmatrix} 0 & 0 & 1 \\ 0 & 0 & 0 \\ 1 & 0 & 0 \end{bmatrix}$.

This effect can induce polarization rotation, as used in Pockels cells. In bulk LN waveguides, it has been used for single-sideband modulation and magnetic-free optical isolation by mimicking an EO-driven rotating waveplate [186]. Solc-type polarization control and wavelength filtering have also been demonstrated utilizing this off-diagonal EO coefficient in PPLN waveguides [14,187]. In cavity EO, this off-diagonal EO coefficient can couple two resonances with different polarizations [188,189].

3.2. Non-Resonant Electro-Optic Modulators

EO modulators translate electrical signals to light and are essential components in modern telecommunication networks. LN has been the material of choice for modulators because of its exceptional EO property, low optical and microwave losses, and excellent temperature stability. Integrated EO modulators in bulk LN have been studied extensively for decades [190–192]. Though the basic principles remain similar, migrating these modulators into the thin-film platform brings unique advantages and engineering opportunities. In this subsection, we review non-resonant optical modulators based on thin-film LN waveguides, with specific focus on traveling-wave

modulators, including their figures of merit, design strategies, performance tradeoffs, and latest experimental demonstrations.
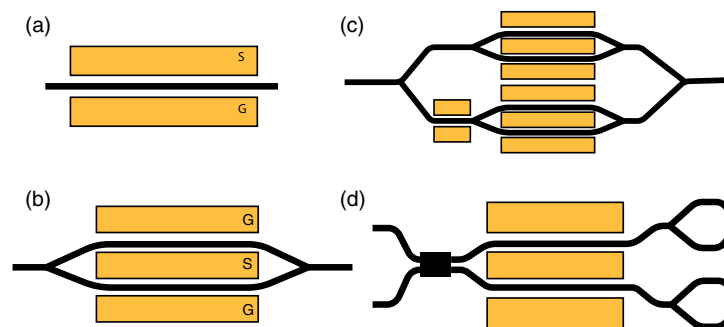
3.2a. Common Modulator Configurations

Figure 10 shows typical EO modulators in X- or Y-cut LN (with Z crystal axis in plane and perpendicular to the waveguides). In phase modulators [see Fig. 10(a)], an applied voltage induces an index change in the waveguide and causes a phase shift of the transmitted light. When driven with a strong RF signal, phase modulators generate sidebands, and can be used for frequency comb generation [193] and frequency shifting [194,195], among other applications. Figure 10(b) shows a typical intensity modulator based on a MZI embedded in a coplanar waveguide (CPW) electrode, a configuration called the Mach–Zehnder modulator (MZM). This design features a push–pull configuration, where the two arms naturally experience electric fields with opposite polarities and thus opposite phase shifts. This is the most common configuration in thin-film LN modulators. In addition, combining two MZMs can realize an in-phase/quadrature (IQ) modulator [see Fig. 10(c)] [16]. IQ modulators can encode information in both amplitude and phase, and are important for coherent transmission systems. Besides MZMs, Michelson interferometer modulators (MIMs) have also been studied [196,197], as illustrated in Fig. 10(d). Here, we have been focused on X/Y-cut modulators. In principle, Z-cut EO modulators can also be implemented by placing electrodes on top of the waveguides. But so far they are less common in thin-film LN devices, because it is more difficult to efficiently deliver the electric field on the submicrometer waveguides while maintaining low microwave and optical loss.

3.2b. Performance Metrics

The key metrics for EO modulators include the half-wave voltage (V_π), EO bandwidth (BW), and insertion loss (IL). For intensity modulators, the extinction ratio (ER) is also a critical parameter. In addition, the linearity and dynamic range are of interest, especially in analog applications. Here, we discuss these performance metrics, their design rules, and the state of the art. Some of these topics have also been discussed in Ref. [198,199]. Figure 11 shows a representative MZM on thin-film LN, with measured V_π, ER, and EO bandwidth.

Figure 10

Four common configurations of EO modulators. (a) EO phase modulator, where an applied voltage induces an index change of the waveguide and thus causes a phase shift in the output light. (b) Mach–Zehnder intensity modulator, consisting of a pair of phase modulators embedded in a Mach–Zehnder interferometer. (c) In-phase/quadrature (IQ) modulator, where both the amplitude and phase of the output light can be independently controlled. (d) Michelson interferometer modulator (MIM), where optical signals are reflected back at the ends of both arms.

Half-wave voltage (V_π). In phase modulators, the half-wave voltage refers to the voltage required to achieve a π-phase shift. In intensity modulators, it refers to the voltage required to switch the output between "on" and "off" states [see Fig. 11(b) as an example]. Note that the V_π measurement is frequency dependent, and more discussions are given in the next subsection on the EO bandwidth. Benefiting from the push–pull configuration, an MZM has a V_π that is half of a phase modulator. In addition, shorter optical wavelength requires lower V_π. To compare modulator designs fairly, in the rest of this section we will give V_π values referenced to MZMs operating near 1550 nm when citing literature (i.e., V_π reported in phase modulators will be divided by two). The V_π of a modulator depends inversely on its length L in the ideal case, and $V_\pi L$ is a commonly quoted figure for comparing the EO interaction strength.

LNOI waveguides feature compact mode areas and allow small electrode gaps. Typical X/Y-cut modulators can support electrode gaps as small as ∼5 μm. Further reducing the gap typically leads to excess optical absorption and microwave loss and requires more precise alignment in fabrication. Measurements of DC/low-frequency $V_\pi L$ in monolithic (dry-etched) LNOI MZMs (at telecom wavelength) typically range from 2.1 to 2.5 V-cm [16,21,22], and can reach, for example, 1.8 V-cm with a 3.5 μm electrode gap [85]. In hybrid LN modulators, since the optical mode is only partially confined in LN, $V_\pi L$ tends to be slightly larger [23,25,102,103,106,115,200], but can also be engineered to be comparable to monolithic ones: 2.1 V-cm has been demonstrated in SiN$_x$-loaded LN MZM [201].

Modeling of V_π requires the calculation of microwave and optical mode overlap—both can be simulated using standard electromagnetic mode solvers. Mathematical formulations can be found in, e.g., Refs. [199,202]. In general, maximum optical-microwave mode overlap inside LN along the correct crystal direction (Z for r_{33}) is desired. It is worth mentioning that the electric field in LN *cannot* be simply approximated as the voltage across the electrode over the gap size, V/g. This is because the dielectric constant of LN ($\epsilon_{r,z} = 28$ and $\epsilon_{r,x/y} = 44$ for clamped, high-frequency response) is drastically different from that of its cladding material

Figure 11
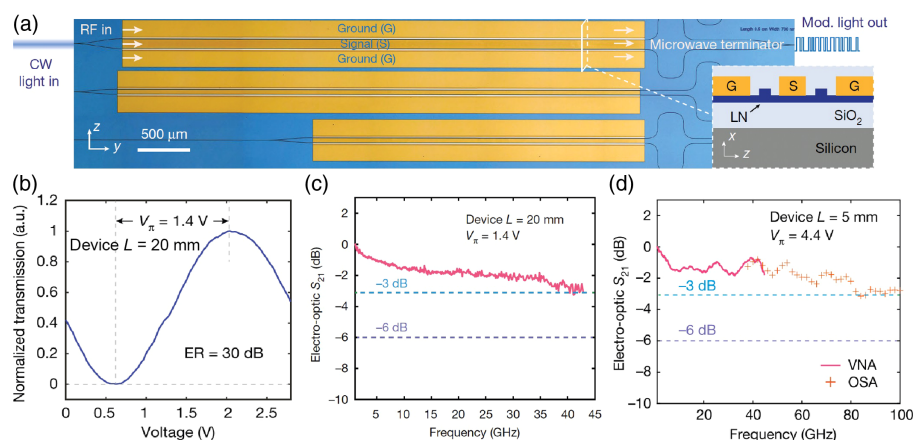
Traveling-wave lithium-niobate electro-optic Mach–Zehnder modulator. (a) Device layout (three MZMs) and cross section. (b) DC/low-frequency response of the modulator, showing a V_π of 1.4 V in a 20 mm device with an ER of 30 dB. (c), (d) Electro-optic frequency response. Shorter modulators can achieve larger EO bandwidth but require larger V_π. Reprinted with permission from Wang *et al.*, Nature **562**, 101–104 (2018) [21]. Copyright 2018 Springer Nature Limited.

(e.g., $\epsilon_r = 3.9$ for SiO$_2$). As a result, the electric field is non-uniform in the gap, as can be seen in Fig. 12. Intuitively, when one draws a line from the ground to the signal (passing through the LN ridge), we have $V = -\int \bar{E} \cdot d\bar{l}$. At material boundaries, the perpendicular $D_\perp = \epsilon E_\perp$ field, not the E-field, is continuous. Therefore, in a high (microwave) index medium, the E-field is small. In other words, the voltage drops preferentially across the low-index material instead of the high-index LN. In fact, this is a critical problem in designing modulator electrodes. To enhance the E-field in the LN waveguide, it is beneficial to have partially etched waveguides and place the electrodes directly on the slab. In general, a device with a thicker slab, a wider LN waveguide, and a dielectric cladding would have lower V_π. Furthermore, a cladding material with high RF index but low optical index is highly desirable for this purpose. As a practical example, Xu *et al*. use 1-µm-wide waveguides when routing the optical signals while tapering up to 4-µm-wide waveguides in the phase modulation region to reduce V_π [16]. It is worth mentioning that, to achieve the same V_π, wider waveguides allow a wider electrode gap, which can reduce microwave loss and increase bandwidth (as discussed in the following subsections).

EO bandwidth. Modulator responses are frequency dependent. This frequency dependence is usually characterized by the electro-optic scattering parameter, EO S_{21}. Definitions of EO bandwidth vary within the literature, but commonly used standards include the 3 dB and 6 dB bandwidth (i.e., the frequency at which the modulation efficiency drops by 3 or 6 dB from a reference frequency). The reference frequency can be chosen at or near DC [21], but may also be taken at a higher frequency (e.g., 1 GHz) [16,203]. Choosing a non-DC reference frequency has the following rationales. First, DC and low-frequency responses are difficult to measure and sometimes unstable. It is observed that the DC response of LN modulators can be inefficient and unstable, and often drifts over time due to photorefraction, photoconduction, and surface charge accumulation [204,205]. In commercial LN modulators, it is common to have separate DC bias electrode and feedback circuits to stabilize the operation. Thermal-optic phase shifters can be used for DC control as well. They are more stable and compact [16], but at the expense of static power dissipation. Second, some modulator designs have a rapid roll-off at low frequencies, often due to impedance mismatch. This narrow-band roll-off may not be a concern for some applications; instead, the flatness and modulation response at high frequency may be more important.

In a non-traveling-wave modulator, where the electrode is a simple capacitor, the EO bandwidth is mainly restricted by the RC (resistance-capacitance) limit of the electrode. Though LN possesses one of the largest EO coefficients among all

Figure 12
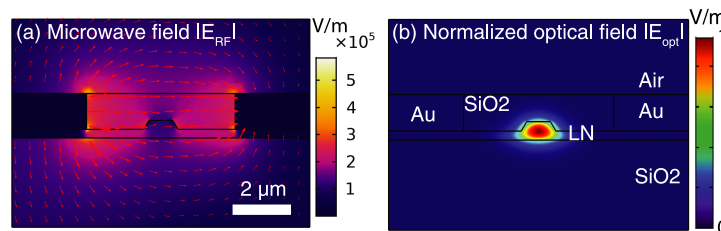
(a) Microwave and (b) optical electric field distribution in a monolithic X-cut EO modulator. The electrode has a gap of 5 µm. The microwave field is normalized so that the voltage across the two electrodes is 1 V. Due to the large microwave permittivity of LN, the electric field in the LN ridge is weaker than that in the cladding.

materials, the absolute index modulation under a reasonable voltage is still weak. For instance, an electric field of 10^5 V/m (1 V/10 μm) can only induce an index change of 1.4×10^{-5}. To accumulate a π phase shift, the modulator requires millimeter- or even centimeter-scale length given reasonable driving voltage. Electrodes with such length will have a large capacitance. At frequencies $\omega > 1/RC$, the capacitor (which is the electrode) has low impedance so the voltage would not drop across it. Conventionally, R is at 50 Ω, determined by the source and cable impedance. For example, a typical few-micrometer-gap CPW electrode has a capacitance on the order of 100 pF/m, resulting in a RC-limited, 3-dB EO bandwidth of about 15 GHz in a 2-mm-long modulator [85].

To achieve an EO bandwidth of tens to hundreds of gigahertz, traveling-wave modulators are necessary, where the electrode is a transmission line. In traveling-wave modulators, three key design considerations are particularly important: (1) velocity matching, (2) impedance matching, and (3) microwave loss.

Velocity matching allows microwave and optical signals to co-propagate at the same speed so that the modulation accumulates constructively. A natural question is "which velocity to match?" [206]. Considering the case of a phase modulator, where a single-tone microwave signal modulates continuous-wave (CW) light, it is tempting to think that their phase velocities should match so that their phase fronts align when propagating. However, once the optical field is modulated, new frequencies (sidebands) are generated, and the centroid of the modulated optical signal travels at its group velocity ($v_{g,\text{opt}} = d\omega_{\text{opt}}/d\beta_{\text{opt}}$, where ω_{opt} and β_{opt} are the angular frequency and propagation constant of the optical signal, respectively). _Therefore, the phase velocity of the microwave signal should match the group velocity of the optical signal_ [207,208]. This can also be understood using a phase-matching picture: (1) energy conservation requires the frequency difference between the original and modulated light to be equal to the microwave frequency, $\Delta\omega_{\text{opt}} = \omega_{\text{RF}}$; (2) similarly, momentum conservation requires $\Delta\beta_{\text{opt}} = \beta_{\text{RF}}$. As a result, $d\omega_{\text{opt}}/d\beta_{\text{opt}} = \omega_{\text{RF}}/\beta_{\text{RF}}$ is needed for efficient modulation; i.e., optical group velocity matches microwave phase velocity. For practical applications such as optical communication, instead of a single-tone or narrow-band signal, the microwave drive is usually a complex waveform. It is natural to think that the group velocity of the microwave signal should match that of light. While the concept of group velocity accurately describes the propagation speed of the envelope of an optical wavepacket (carrier frequency at hundreds of terahertz and bandwidth of tens of gigahertz), it is less proper for the electrical signals, which usually span from DC to tens or hundreds of gigahertz (e.g., for information encoded in square waves). It is worth noting that while the optical group and phase velocities/indices differ significantly in thin-film LN waveguides (usually >15% difference), microwave transmission lines have relatively small dispersion so their group and phase velocities/indices are similar (usually < 1% difference and will asymptotically approach a constant at higher frequencies). In practice, velocity mismatch matters more at higher frequencies. It is therefore appropriate to match the microwave effective index to the optical group index towards the highest target modulation frequency. In bulk LN modulators, the microwave index is mainly restricted by the permittivity of LN, which is very high ($\epsilon_{r,z} = 28$ and $\epsilon_{r,x/y} = 44$) and hard to match the optical index ($\epsilon_{r,z} = 4.6$ and $\epsilon_{r,x/y} = 4.9$). In thin-film LN modulators, as the LN's participation in the microwave field is small, the effective index of the transmission line is easier to engineer and can be effectively tuned by the thickness of the cladding or buried oxide, as well as the metal thickness, leading to perfect velocity matching.

Impedance matching ensures proper RF interface between the modulator and driving electronics. It is conventional to design the characteristic impedance (Z_0) of the transmission line to be 50 Ω to match standard 50 Ω RF electronics, including source, amplifier, cable, termination, etc. However, impedance matching is often compromised (usually with $Z_0 < 50\,\Omega$) due to practical design constraints. Impedance mismatch leads to two main issues. (1) It causes microwave reflection. Reflections between the two ends of the transmission line can form standing waves (resonances) and cause ripples in EO frequency response, which is especially prominent when the transmission line is short or low-loss. In addition, reflections at the source end prevent efficient power delivery, with a (power) reflection coefficient of $|(Z_L - 50\Omega)/(Z_L + 50\Omega)|^2$. (2) Given the same RF power, lower characteristic impedance results in smaller voltage, following $P = V^2/Z_0$. Combining input reflection and voltage scaling, the impedance mismatch gives an overall V_π penalty of $1/[2Z_0/(Z_0 + 50\Omega)]$ or, equivalently, an EO S_{21} offset of $20\log[2Z_0/(Z_0 + 50\Omega)]$. For instance, $Z_0 = 40\Omega$ will cause a 12.5% increase in V_π or, equivalently, a 1 dB offset in EO S_{21}. The effect of EO offset, as well as resonance ripples, can be seen in the simulated EO S_{21} in Fig. 13 (iii), where Z_0 is set to 40 Ω. Note that the rapid drop-off near DC is because at low frequency, the transmission line is much shorter than the wavelength, so the source directly sees an input impedance of 50 Ω (neglecting DC resistance) given by the load/termination. This drop-off is even sharper for longer modulators. In the presence of the sharp drop-off, the definition of 3-dB EO bandwidth varies sensitively to the choice of reference frequency. Also, Z_0 is frequency dependent and tends to be higher at lower frequencies due to increased line inductance. In thin-film LN modulators, because of the narrow CPW gap (typically around 5 µm), the center conductor needs to be very narrow ($\sim 10\,µm$) to achieve 50 Ω impedance, which induces significant ohmic microwave losses. In many cases, it is more beneficial to increase the center conductor width (e.g., 20–30 µm). This will reduce Z_0 to around 35–40 Ω, but can significantly reduce the transmission line loss (by a few dB/cm) and may outweigh the penalty paid by impedance mismatch. Under

Figure 13
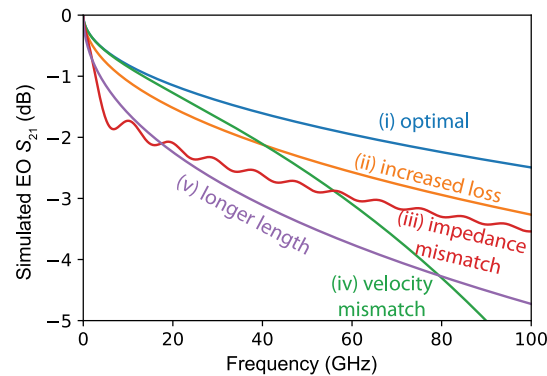
Illustration of how EO bandwidth is affected by transmission line loss, impedance mismatch, velocity mismatch, and modulator length. (i) Simulated EO S_{21} of a MZM of which the transmission has a characteristic impedance of 50 Ω, propagation loss of $0.75\,\mathrm{dB\,cm^{-1}\,GHz^{-1/2}}$, perfectly matched phase velocity $n_m = n_{g,\mathrm{opt}} = 2.28$, and modulation length of 7 mm. (ii) An increased transmission line loss ($0.9\,\mathrm{dB\,cm^{-1}\,GHz^{-1/2}}$) accelerates the roll-off in EO response. (iii) Impedance mismatch (40 Ω) causes an offset and forms ripples in EO response. (iv) Velocity mismatch ($n_{g,\mathrm{opt}} - n_m = 0.2$) leads to rapid roll-off at high frequencies. (v) Longer length (1.4 cm) reduces EO bandwidth, but it is worth mentioning that the actual V_π is still lower than that of shorter modulators.

this tradeoff, one needs to strike a balance when designing a modulator depending on a specific bandwidth and V_π requirement.

Given that velocity matching can be achieved relatively easily as compared to its bulk counterpart, transmission line loss is the main limiting factor for high-frequency operation of LNOI modulators. Major loss factors include metal loss (ohmic heating), dielectric loss, and surface roughness [209]. In general, metal loss dominates and increases as $\sqrt{f}$ due to the skin effect (skin depth $\delta_s = \sqrt{1/(\pi f \sigma \mu_0)}$, where f is the frequency, σ is the conductivity, and μ_0 is the vacuum permeability). Dielectric loss depends on the material's loss tangent and scales linearly with frequency. The choice of the substrate and cladding/buried oxide material critically affects the dielectric loss. In addition, metal roughness effectively increases the travel path of current and thus increases loss, but this effect has not been studied in depth in the context of thin-film LN modulators.

In standard CPWs, the tuning knobs are very limited—gap size, center conductor width, metal thickness, and dielectric above and below the metal. This results in a small engineering margin. More importantly, due to the small gaps used in LNOI modulators (typically $\sim 5\,\mu$m), the microwave mode is highly confined and causes significant current crowding near the metal edge. As a result, typical losses of CPWs in LNOI modulators are around $0.7 - 1.1\,\text{dB}\,\text{cm}^{-1}\text{GHz}^{-1/2}$. Recently, segmented CPWs have been applied to LNOI modulators [203]. The segmented CPW consists of a standard CPW and microstructured segments extending out from the main CPW in the gap region. The segments prevent current from flowing on the edge of the metal near the gap region and significantly reduce microwave loss ($0.26\,\text{dB}\,\text{cm}^{-1}\text{GHz}^{-1/2}$ demonstrated in [203]). Similar designs have been used in III-V modulators [210], mainly to improve velocity matching, because the segments add capacitance and reduce the phase velocity, which is necessary due to the slow optical group velocity in III-V waveguides. For LNOI modulators, a carrier material with lower permittivity (such as quartz) may be needed instead of standard Si to compensate for the slow-wave effect and maintain velocity matching.

Considering all three factors mentioned above, the frequency response of an EO modulator follows [211]:

$$m(\omega) = \left| \frac{2Z_{\text{in}}}{Z_{\text{in}} + Z_L} \right| \left| \frac{(Z_L + Z_0)F_+ + (Z_L - Z_0)F_-}{(Z_L + Z_0)e^{\gamma_m L} + (Z_L - Z_0)e^{-\gamma_m L}} \right|, \tag{2}$$

where ω is the microwave frequency, $Z_{\text{in}} = Z_0 \frac{Z_L + Z_0 \tanh(\gamma_m L)}{Z_0 + Z_L \tanh(\gamma_m L)}$ is the input impedance of the transmission line, $F_\pm = (1 - e^{\pm \gamma_m L - j\frac{\omega}{c} n_{g,\text{opt}} L})/(\pm \gamma_m L - j\frac{\omega}{c} n_{g,\text{opt}} L)$ accounts for the forward/backward propagating waves, $\gamma_m = \alpha_m + j\frac{\omega}{c} n_m$ is the complex microwave propagation constant (n_m being the microwave effective index, α_m being the loss rate), $n_{g,\text{opt}}$ is the optical group index, L is the modulator length, and c is the speed of light in free space. Here, we assume both the source and load (termination) have impedance Z_L (in most cases at 50 Ω). The EO frequency response (EO S_{21}) in decibels is $20 \log(m(\omega))$. It can be seen that a thorough characterization of the electrical response of the microwave transmission line already allows us to accurately predict the EO response, as long as the optical group index is known. As a rule of thumb, in the case of perfect velocity and impedance matching, 3 dB EO bandwidth corresponds to $\sim$6.4 dB electrical bandwidth (often referred to as EE bandwidth) of the transmission line. This is essentially a loss-limited bandwidth. Figure 13 shows some simulated EO S_{21} curves based on Eq. (2) to illustrate the effects of metal loss, impedance mismatch, velocity mismatch, and modulator length. These effects have been discussed individually above.

Due to microwave loss and velocity mismatch, shorter modulators have larger EO bandwidth [see Fig. 11(c) versus Fig. 11(d), as well as Fig. 13(i) versus Fig. 13(v)], but the shorter length also results in larger V_π. The bandwidth-length product may be considered as an engineering tradeoff in modulator design [212,213]. In addition, since $V_\pi L$ is roughly a constant given a certain electrode and waveguide design, BW/V_π (referred to as voltage-bandwidth limit) becomes a valuable figure of merit when comparing modulator performance.

Insertion loss (IL). The IL can be divided into two parts: fiber-to-chip coupling loss and on-chip insertion loss. Fiber-to-chip coupling has been discussed in Subsection 2.3d. On-chip insertion loss includes (1) metal absorption on the electrode, (2) waveguide propagation and bending loss, and (3) insertion loss of the splitters/combiners (usually in the form of y-splitter [15,21] or multimode interference (MMI) couplers [16]). With state-of-the-art dry-etching processes, waveguide propagation loss is typically < 0.3 dB/cm (with 0.027 dB/cm measured in Ref. [11]; see Subsection 2.3), bending loss can be mitigated by increasing the bending radius, and splitter insertion loss as low as 0.054 dB has been demonstrated using dry-etched MMI in LN [16]. Excess optical loss mainly comes from absorption in the metallic electrode, which becomes worse when there is misalignment between the metal and optical layers. Metal absorption thus causes a tradeoff between V_π and on-chip insertion loss: a small electrode gap and wide waveguide reduces $V_\pi \cdot L$ but increases optical absorption in the metal.

Extinction ratio (ER). The ER is defined to be the output intensity ratio between the "on" and "off" states in an intensity modulator. It is largely determined by the design and fabrication of the MZI. Specifically, unbalanced loss in the two MZI arms will decrease the ER, and imperfections in the splitter/combiner will decrease the ER. In addition, undesired polarization impurity/rotation in the MZM, for example, from waveguide bending [214], will also affect the ER. Typical measured ERs of LNOI MZMs are around 20 to 30 dB (tested at low frequency) [16,21,23,201]. ER > 40 dB has been demonstrated in a 3 mm MZM [22]. In addition, by cascading two MZIs, ER of 53 dB has been demonstrated in Ref. [116].

Linearity and dynamic range. Considering an intensity modulator biased at the quadrature point (halfway between "on" and "off"), the modulated optical intensity will respond linearly to a small electrical voltage. However, at large microwave drives, the nonlinearity of the modulator becomes significant and affects the signal integrity in RF photonics systems and analog fiber-optic datalinks. The linearity can be quantified using, for example, third-order intermodulation distortion (IMD3) spurious-free dynamic range (SFDR). Given two RF input signals at frequencies f_1 and f_2 (both within the modulator bandwidth), the intermodulation products include $m f_1 \pm n f_2$ (m and n are integers). IMD3 includes contributions from $2 f_1 - f_2$ and $2 f_2 - f_1$. These components are the most challenging distortion products since they are directly adjacent to the input tones. IMD3 SFDR refers to the input RF power range between the two points where the fundamental modulation output (RF power from photodetector) is beyond the system noise floor (lower limit) and where the IMD3 becomes larger than the noise floor (upper limit) [see Fig. 14(a)]. Alternatively, it can be seen as the signal-to-noise ratio of the fundamental output when the IMD3 reaches the system noise floor. Mathematically, it is defined as SFDR $= (P_{\text{int}}/\text{NF})^{2/3}$, where P_{int} is the output power (at the detector) where fundamental and IMD3 intercepts, and NF is the noise floor (in units of W/Hz or dBm/Hz). As a result, SFDR has the unit of dBHz$^{2/3}$. All of these definitions are equivalent since the fundamental has a slope of 1 and IMD3 has a slope of 3. Figure 14(a) illustrates the concept, and Fig. 14(b) shows measured IMD3 SFDR data from a thin-film LN modulator [22].

It is clear that the SFDR not only depends on the linearity of the modulator but also is affected by noise. The SFDR of a photonic link depends on laser noise, amplifier (RF and optical) noise, detector noise, and linearity and insertion loss of the modulator. SFDR is relatively under-studied in the current literature of LNOI modulators. Based on the limited number of reports [22,25,200,215], measured IMD3 SFDRs using LNOI modulators are in the range of $90-100\,\mathrm{dBHz}^{2/3}$, which has yet to outperform the best demonstrations in bulk LN modulators ($> 120\,\mathrm{dBHz}^{2/3}$ reported [216]). As the lasers, detectors, and amplifiers used in these reports are different, it is difficult to make fair comparisons of the modulator linearity across the literature. Future increases in optical pump power and reduction of coupling loss in LNOI modulator-based datalinks may substantially increase the measured SFDR.

3.2c. State of the Art

Though thin-film LN-based EO modulators were first demonstrated as early as 2005 [217], they have since undergone relatively slow development. This is mainly due to the lack of low-loss micro-/nano-structured waveguides. The first breakthrough came around 2013 when rib loading was proven to be an effective solution to avoid LN etching [103]. Since then, various loading materials have been exploited, and rib-loaded modulators have become a major approach [25,115,201,218,219]. Meanwhile, other approaches such as proton exchange in thin film have also been explored [72,220]. The second breakthrough happened around 2016 when dry-etched LNOI modulators reached waveguide propagation loss below 1 dB/cm [20]. Enabled by this monolithic approach, the field has seen rapid progress [85,116,196,221–224], including the demonstration of >100 GHz bandwidth modulators operating at CMOS-compatible voltages [21], and coherent modulators that support data rates up to 320 Gbit/s [16]. Moreover, heterogeneous integration by bonding thin-film LN (either etched [22,197] or unpatterned [23]) on SOI and SiN_x PICs has also proven to be a promising direction. This direction is now being investigated not only by academics, but also by silicon photonic foundries and national laboratories/facilities [200,225]. This may lead to scalable production and multi-functional integration for thin-film LN modulator technologies.

Figure 14
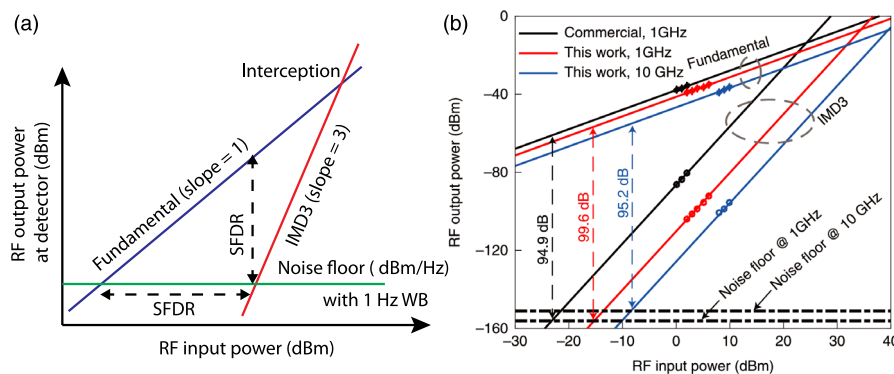
Third-order intermodulation distortion (IMD3) spurious-free dynamic range (SFDR). (a) Illustration of IMD3 SFDR. (b) Measured IMD3 SFDR in a thin-film LN modulator and its comparison to that of a commercial bulk modulator [22]. (b) Reprinted with permission from He *et al.*, Nat. Photonics **13**, 359–364 (2019) [22]. Copyright the Author(s), under exclusive license to Springer Nature Limited 2019.

Table 3 summarizes the performance of some representative EO modulators based on thin-film LN, including both monolithic and hybrid approaches, as well as covering Mach–Zehnder intensity modulators, phase modulators, and MIMs.

3.3. Resonant Electro-Optic Modulators

The non-resonant EO modulators described above can achieve low V_π and high bandwidth, but require long devices (centimeters for few-volt V_π) to do so. For many applications in high-density integrated photonics, more compact modulators are required. One straightforward way to accomplish this is to use resonant EO modulators, such as ring modulators and photonic crystal cavity modulators, illustrated in Figs. 15(a)–15(e). In their most basic form, such modulators allow the resonance frequency to be changed by an applied voltage, which can change the transmission of light at a frequency near resonance. This subsection reviews progress on such resonant modulators in thin-film LN.

One challenge when working with resonant EO modulators is that a voltage applied to the modulator can change both the amplitude and phase of the transmitted light, depending on the coupling ratio $\eta = \kappa_e/\kappa_i$, where κ_i and κ_e are the intrinsic/internal (due to loss in the cavity) and extrinsic/external (due to coupling to external waveguides) power loss rates, respectively. The transfer function for monochromatic light

Table 3.   Representative Non-Resonant EO Modulators Based on Thin-Film LN

Modulator Type[a]	Platform/ Method	$V_\pi \cdot L$ (V-cm)	V_π(V)	L (mm)	3 dB EO BW (GHz)	ER (dB)	Propagation Loss (dB/cm)	Year	Ref.
MZM	Monolithic	2.2	1.5	15	20	–	0.5	2017	[226]
MZM	Monolithic	2.2/2.3/ 2.8	4.4/2.3/ 1.4	5/10/20	100/80/45	30	0.3	2018	[21]
MZM	Monolithic	3.12	2.6	12	56	–	–	2019	[223]
MZM[b]	Monolithic	2.7	1.35	20	175[c]	20	< 0.5	2020	[203]
MZM[d]	Monolithic	1.8	9	2	15	10	3	2018	[85]
PM	Monolithic	4.7	4.7	10	40	–	1	2016	[20]
PM	Monolithic	1.748	1.9	9.2	47[e]	–	7	2018	[24]
PM	Monolithic	3.5	1.75	20	>45	–	0.5	2019	[193]
IQ modulator	Monolithic	2.47/ 2.325	1.9 / 3.1	13 / 7.5	48 / 67	25	0.15	2020	[16]
MZM	Etched LN on SOI	2.55/ 2.22	5.1 / 7.4	5 / 3	70	40	0.98	2019	[22]
MZM	Ta$_2$O$_5$ rib loading	4	6.8	6	–	20	5	2013	[103]
MZM	Chalcogenide rib loading	3.8	6.3	6	1	15	1.2	2015	[102]
MZM	SiN$_x$ rib loading	3	2.5	12	8	13.8	7	2016	[115]
MZM	SiN$_x$ rib loading	3.1	3.88	8	33	18	–	2016	[25]
MZM	SiN$_x$ rib loading	1.925	0.875	24	–	30	<2.25	2020	[201]
MZM	LN on SiN$_x$	6.67	3.34	5	30.55	> 20	1.6[f]	2020	[200]
MZM	LN on SOI	6.7	13.4	5	> 106[g]	30	0.6	2018	[23]
MIM	Etched LN on SOI	1.2	12	1	17.5	30	0.3[h]	2019	[197]
MIM	Monolithic	1.4/ 1.52	14 / 7.6	1 / 2	12	27.6/ 20	4.6	2019	[196]

[a]MZM, Mach–Zehnder modulator; PM, phase modulator; IQ modulator, in-phase/quadrature modulator; MIM, Michelson interferometer modulator. V_π and $V_\pi \cdot L$ refer to low-frequency (near-DC) values, and those for PMs are divided by 2 to match MZMs. All modulators were measured near 1550 nm.

[b]Segmented CPW electrode.

[c]Measured 1.8 dB EO roll-off at 50 GHz; extrapolated 3 dB EO bandwidth to be ∼175 GHz.

[d]Not traveling wave.

[e]Estimated from electrical bandwidth; measurement up to 500 GHz without significant roll-off from index mismatch.

[f]Estimated based on Ref. [227].

[g]Limited by measurement instrument; extrapolated to > 200 GHz.

[h]Estimated from calculation.

with frequency ω through a modulator such as that shown schematically in Fig. 15(a) with a resonance frequency $\omega_r = \omega_0 + \chi V$ that shifts linearly with applied voltage at a rate χ is given by [228]

$$t = \frac{E_{\text{out}}}{E_{\text{in}}} = \frac{(\kappa_i - \kappa_e) - 2i\Delta}{(\kappa_i + \kappa_e) - 2i\Delta}, \tag{3}$$

where $\Delta = \omega - \omega_r$. This optical transfer function does not represent either pure phase or amplitude modulation, but in certain regimes it can act as such. As an example that is particularly relevant for high-density photonic circuits, consider the phase modulation case where $\kappa_e \gg \kappa_i$ and the input light is resonant with the zero-voltage resonance frequency $\omega = \omega_0$. In this regime, the power transmission is nearly lossless $T = |t|^2 \approx 1$ and the output light is phase shifted relative to the input by $\delta\phi = \pi - \frac{4\chi\delta V}{\kappa_e}$ for small voltage signals δV. Note that for larger voltages of order $|V| \gtrsim \frac{\kappa_e}{4\chi}$, the phase response becomes nonlinear and saturates near the bounds $\delta\phi = 0$ and $\delta\phi = 2\pi$. If purely linear phase response is required, it can be achieved with the non-resonant phase modulators described in the previous section.

Resonant modulators can achieve strong modulation despite their small size because the optical field circulates and interacts with the microwave field produced by the electrodes many times. Typical resonant modulators are made using a cross-sectional waveguide and electrode geometry that is similar to that of a non-resonant modulator. In such a case, a useful way to compare the performance of a resonant and non-resonant modulator is to consider the effective interaction length of the modulator $l_{\text{eff}} = l_f \alpha$, given by the product of the optical field attenuation length $l_f = \frac{2c}{\kappa n_{\text{eff}}}$ inside the resonator, where $\kappa = \kappa_i + \kappa_e$ is the total power decay rate, and the effective

Figure 15
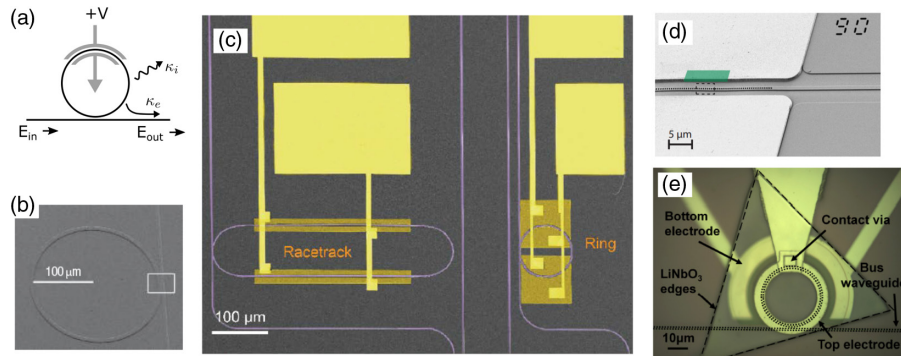
Resonant electro-optic modulators in thin-film lithium niobate. (a) Schematic diagram of a typical ring modulator. The input light (E_{in}) couples to a ring resonator with internal and external coupling rates (κ_i and κ_e, respectively). The gate voltage enables modulation of the output light (E_{out}). (b) Early Z-cut ring modulator, with electrodes placed above and below the device layer [55]. (c) Ring and racetrack modulators in X-cut lithium niobate [85]. (d) Photonic crystal cavity modulator [182]. (e) Ring resonator in a hybrid LN/Si platform [113]. (b) Reprinted by permission from Macmillan Publishers Ltd.: Guarino *et al.* Nat. Photonics **1**, 407–410 (2007) [55]. Copyright 2007. (c) Reprinted with permission from [85]. Copyright 2018 Optical Society of America. (d) Reprinted with permission from Li *et al.*, Nat. Commun. **11**, 4123 (2020) [182], licensed under a Creative Commons Attribution 4.0 International License. (e) Reprinted with permission from [113]. Copyright 2014 Optical Society of America.

electrode coverage fraction α. For some types of resonant modulators such as ring resonators, the electrode geometry is constrained such that the electric field cannot be applied along the optimum z crystal axis [202], which also reduces the effective electrode coverage fraction α below the simple geometric result. For thin-film lithium niobate, low-loss resonators with $Q = 10^7$ at wavelengths near 1.5 μm can be achieved, corresponding to EO interaction lengths of order 1 m—about tenfold longer than typical non-resonant EO modulators.

However, the compactness and high modulation efficiency of resonant modulators comes at the cost of reduced EO bandwidth. The optical field within the resonator can only respond to modulation at a rate set by the total decay rate κ of the resonator [229]. For example, for a resonator with $Q = 10^7$ at wavelengths near 1.5 μm, $\kappa = 2\pi \times 20$ MHz.

The design of EO modulators based on resonance frequency modulation requires a difficult tradeoff between modulation efficiency (set by the effective EO interaction length) and bandwidth (set by the resonator linewidth). However, for many applications such as optical switch networks [230] and optical beam steering [231], even the relatively low bandwidth provided by high-Q resonators is sufficient. For these applications, compact resonant modulators in thin-film LN offer a promising alternative to techniques such as thermal tuning, with lower power dissipation and higher bandwidth. Note that this tradeoff can be tailored by using multiple coupled optical resonators, such as in coupled resonator optical waveguides [232] and the photonic molecules described in Subsection 3.5. Additionally, by modulating the resonator-waveguide coupling instead of the resonance frequency, the bandwidth limitation can be reduced [229].

Over the past two decades, resonant EO modulators in thin-film LN have been widely studied. Table 4 presents a selection of recent works on single-resonator modulators, and compares relevant figures of merit for these devices. Both monolithically dry-etched thin-film LN resonators [55,85,166,173,182] and hybrid ones based on rib loading [98,102,103] or heterogenous bonding [111–113] have been explored. Typical resonant EO modulators in thin-film lithium niobate have resonances that can be electrically tuned at low frequencies by 1–20 pm/V. This figure of merit on voltage-tuning rate is determined in part by the same electrode design considerations as non-resonant modulators. For example, more closely spaced electrodes improve the voltage-tuning rate. This effect is exploited in Ref. [112], in which a doped Si waveguide is used as part of an electrode. Additionally, a large effective electrode coverage fraction α improves the voltage-turning rate. Modulators based on photonic crystal cavities such as those in Ref. [182] have a near-optimal effective electrode coverage fraction α because they do not require waveguide bends. Besides ring, racetrack, and photonic crystal cavities, Bragg reflectors may also be used to form resonant EO modulators [233] or tunable filters [234].

3.4. Electro-Optic Frequency Combs

3.4a. Non-Resonant Electro-Optic Comb

Optical frequency combs (OFCs) have enabled numerous applications in science and engineering. The ability to achieve strong optical confinement at the micro- and nano-scale on low-loss optical platforms has allowed the realization of chip-scale OFCs. One way to generate OFCs is through Kerr nonlinearity, which will be discussed in Subsection 4.5. Another way is through the linear EO effect, by phase-modulating an optical signal in a material with a large $\chi^{(2)}$ value. A comprehensive review of EO frequency combs, their principles, and their applications can be found in Ref. [235].

These non-resonant EO comb sources offer several promising features, including intrinsic mutual coherence between all the comb lines, convenient tuning of the repetition rate and center frequency, and favorable spectral flatness. The latter would be of great importance for optical communication [236], optical arbitrary waveform generation [237], and radio-frequency (RF) photonics [238].

An essential parameter for generating a frequency comb using an EO phase modulator is the modulation index ($\beta = \pi \frac{V_p}{V_\pi}$), where V_p and V_π are the peak voltage for the driving microwave field and the half-wave voltage of the modulator, respectively. By feeding a CW laser at the frequency ω_c to a phase modulator, and modulating it with a microwave field given by $V(t) = V_p \sin(\omega_m t)$, the optical output field can be written as

$$E(t) = E_0 e^{i\omega_c t} e^{i\beta \sin(\omega_m t)}. \tag{4}$$

Taking the Fourier transform of the time-domain signal and applying Jacobi–Anger expansion [239] allows us to express the output field in the frequency domain as

$$E(\omega) = E_0 \sum_{n=-\infty}^{+\infty} J_n(\beta)\delta(\omega - n\omega_m - \omega_c), \tag{5}$$

where J_n is the Bessel function of the first kind, and δ is the Dirac delta function. The output spectrum consists of equidistant spectral elements with spacing ω_m around the center frequency of the input field, ω_c. J_n defines each comb line's amplitude, while the modulation index can tune the overall shape of the spectrum.

Figure 16(a) shows an experimentally measured frequency comb generated from a LNOI phase modulator. This modulator was fabricated on an X-cut thin-film LN and has a length of 2 cm with V_π of 3.5–4.5 V in the frequency range between 5 and 40 GHz [193]. By driving it at substantial RF input voltage ($\sim 4 V_\pi$), a relatively broad comb with over 40 spectral elements was generated with 30 GHz spacing. The low RF V_π is the key to such performance.

Table 4. Representative Resonant EO Modulators Based on Thin-Film LN

| Resonator Type	Platform/ Method	Voltage Tuning Rate (pm/V)	Q-Factor (Loaded)	Crystal Cut	Ref.	Notes
Ring	Monolithic	1.05	4×10^3	Z	[55]	
Ring	LN on SOI	1.7	1.7×10^4	Z	[111]	
Ring	Ta$_2$O$_5$ rib loading	4.5	7.4×10^4	X	[103]	
Ring	LN on SOI	12.5	1.1×10^4	Z	[112]	Doped Si used as conductive electrode
Ring	LN on SOI	3.3	1.4×10^4	X	[113]	
Ring	Chalcogenide rib loading	3.2	1.2×10^5	Y	[102]	
Ring	Monolithic	2.15	2.8×10^3	Z	[166]	
Photonic crystal cavity	Hybrid Si on bulk LN	~ 2	1.2×10^5	X	[114]	Nonlinear phase shift attributed to the field effect in Si.
Racetrack	Monolithic	7	5×10^4	X	[85]	
Ring	Monolithic	4	2×10^6	X	[173]	Single ring properties in a dual ring device
Ring	SiN$_x$ rib loading	1.8	$\sim 9 \times 10^4$	X	[98]	
Photonic crystal cavity	Monolithic	16	1.34×10^5	X	[182]	

The limited microwave power that can be applied to individual phase modulators restricts the number of generated comb lines using this non-resonant approach. This

Figure 16
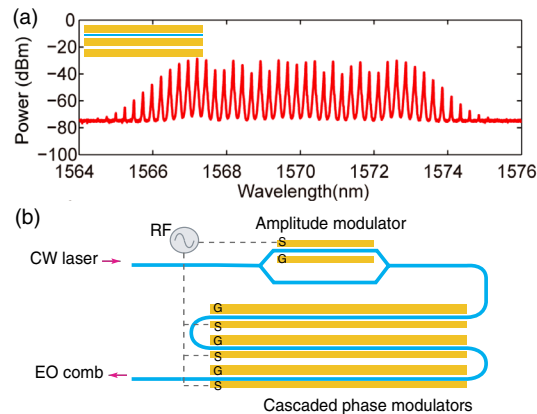
Non-resonant EO comb. (a) Frequency comb generated by driving a single LNOI phase modulator [193]. Inset illustrates the modulator geometry (yellow, metal; blue, optical waveguide). (b) Scheme to generate flat EO comb by cascading multiple EO amplitude and phase modulators. (a) © 2019 IEEE. Reprinted, with permission, from Ren *et al.*, IEEE Photon. Technol. Lett. **31**, 889–892 (2019) [193].

Figure 17
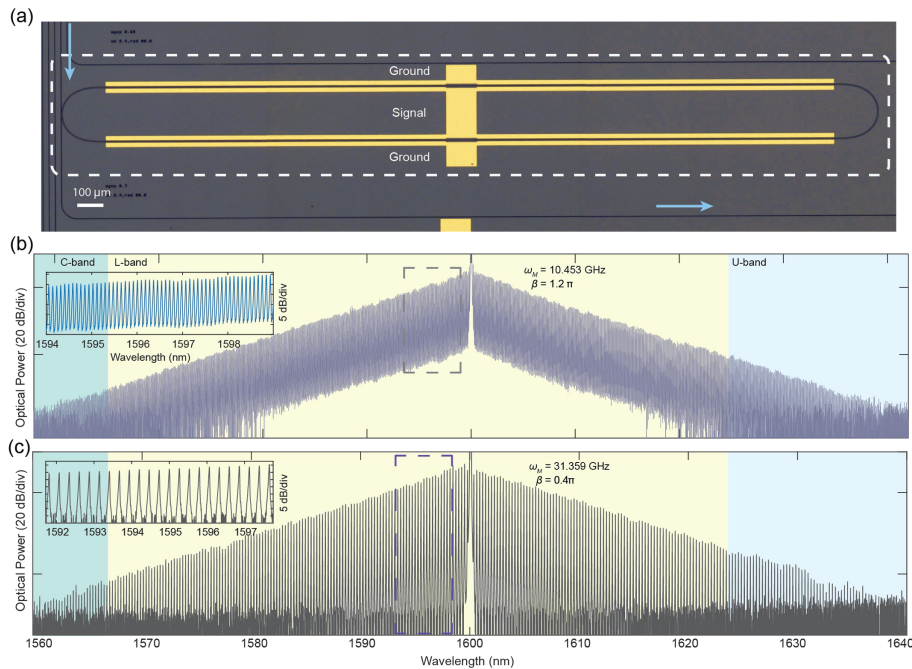
Resonant electro-optic frequency comb source. (a) Micrograph of a resonant integrated electro-optic frequency comb source fabricated on an X-cut LNOI wafer. (b) Measured output spectrum with a line spacing of 10 GHz spanning from 1560 to 1640 nm. The left inset shows a magnified portion of the comb spanning 4 nm. The right inset shows the measured transmission spectrum for an optical resonance that experiences broadening by increasing the microwave driving power. (c) EO comb generated by driving the 10 GHz FSR resonator with a 30 GHz microwave. (a) and (b) reprinted with permission from Zhang *et al.*, Nature **568**, 373–377 (2019) [26]. Copyright the Author(s), under exclusive license to Springer Nature Limited 2019.

issue can be addressed by cascading more devices to achieve broader combs. It is also known that the addition of a Mach–Zehnder intensity modulator in series with the phase modulator can improve the spectral flatness of the generated spectrum, such as the configuration illustrated in Fig. 16(b). Inspired by bulk-modulator demonstrations [240] and cascading a phase modulator with an amplitude modulator in the X-cut LNOI platform, the authors in Ref. [241] could trim their output comb spectrum to have a spectral flatness of 0.89 dB although for a limited number of comb lines.

3.4b. Resonant Electro-Optic Comb

As indicated in the previous section, the small spectral bandwidth (i.e., limited number of comb lines) could potentially limit the applications of non-resonant EO combs. By placing a phase modulator in an optical cavity, the modulation efficiency can be enhanced by the number of passes (determined by the finesse of the cavity) that light goes through the modulator, which could increase the comb bandwidth. Here, the frequency of the RF drive must match the FSR of the optical cavity to maximize cascaded sideband generation. This idea has been studied for almost 50 years [242–245].

With the advent of ultra-low-loss LNOI waveguides and resonators [11], resonant-based EO combs have been realized on chip with unprecedented performance [26]. In Ref. [26], by injecting CW laser light into a high-Q optical racetrack cavity [Fig. 17(a), FSR ~ 10 GHz], which is modulated at a microwave frequency equal to the FSR, a frequency comb spectrum consisting of 900 lines in the telecommunication band was generated [Fig. 17(b)]. A unique property of these comb sources is their ability to generate the spectrum at multiples of the FSR (defined by the size of the racetrack resonator) by changing the microwave driving frequency, as shown in Fig. 17(c). In resonant EO combs, a flat dispersion is desirable; otherwise, the mismatch between the microwave frequency and the cavity FSR introduces a spectral cut-off to the comb spectrum, which can be numerically modeled [246]. Compared to resonant EO combs based on bulk elements, LNOI waveguides allow dispersion engineering and can therefore achieve a broader comb bandwidth. Furthermore, as opposed to Kerr combs, EO comb generation is not sensitive to group velocity dispersion (GVD) at the pump frequency; therefore, it could potentially extend to a wider range of optical pump wavelengths. This flexibility allows pumping at different wavelengths and generating multiple combs simultaneously. A few areas of improvement can be foreseen in the near future. First, the current efficiency and output power of the LNOI EO comb are relatively low compared to Kerr combs. It is shown that employing an intermediate cavity between the input coupler and the EO comb cavity can increase the output comb power [246]. Second, the bandwidth can be improved using resonators with higher Q-factors. With these improvements, LNOI resonant EO combs will become a particularly useful element for applications in telecommunications and microwave photonics.

3.4c. Spectroscopy

Frequency combs are powerful tools for precision spectroscopy [247]. Dual-comb spectroscopy [248] is an emerging technique based on Fourier transform spectroscopy [249], without requiring any moving parts. In this technique, one comb with a repetition rate f_{rep} interrogates the sample of interest (e.g., a gas cell), and beats with a second comb (a local oscillator) with a repetition frequency of $f_{\text{rep}} + \delta f$. The time-domain interference is recorded on a fast photodiode, and the Fourier transform of the time trace reveals a spectrum consisting of the beat notes of the two combs in the RF domain. This technique holds promise in several aspects as it offers broadband measurements with a resolution given by the comb line spacing and a frequency accuracy provided by an atomic clock. One of the requirements for dual-comb spectroscopy

is the need for mutual coherence between the two comb sources. In most demonstrations, the two combs are generated from separate sources (e.g., mode-locked lasers), and establishing mutual coherence could be technically challenging. In dual-comb setups with EO comb sources, mutual coherence can be achieved by driving with phase-locked microwave sources and a shared optical pump laser [250]. These EO comb sources can also provide high agility, flexible operating frequency, and tunable repetition rate. Benefiting from LNOI technology, an on-chip dual-comb spectrometer in the telecommunication region with a resolution of $\sim$10 GHz was demonstrated using a pair of cavity-based EO comb microring sources [248]. Feeding a single CW laser source to both microrings resulted in a coherence time of 5×10^{-3} s. An acetylene gas cell at atmospheric pressure was interrogated in this dual-comb setup, and its transmittance and dispersion were measured. A residual (difference between the measured spectrum and the HITRAN database [251]) of 10% and a standard deviation of 3.4% were reported. As discussed earlier, EO comb sources can be operated over different center frequencies and natural phase-locking established by the microwave driving field. Therefore, one can inject two CW laser sources that are spectrally distant and generate two separate combs in a single device. Using this concept, Ref. [248] demonstrated a spectrally tailored dual-comb interferometer that could probe two different regions at telecommunication wavelengths that are 6.6 THz apart.

Compared to other dual-comb spectrometers based on Kerr combs [252,253], the EO approach has the potential of increasing the resolution (i.e., the repetition rate of the comb sources) with more versatility. By cascading a resonant EO comb and a phase modulator (non-resonant EO comb), a comb spacing of $\sim$3 GHz was achieved [254]. The low-repetition-rate output spectrum was achieved by densifying the original 10 GHz spectrum with a filling factor (integer number) set by the driving frequency on the phase modulator.

3.5. Coupled-Resonator-Based Modulators

EO modulation in coupled resonators brings rich physics and leads to novel and useful devices. In this subsection, we review the basic principles and recent progress of coupled-resonator-based EO modulators on thin-film LN.
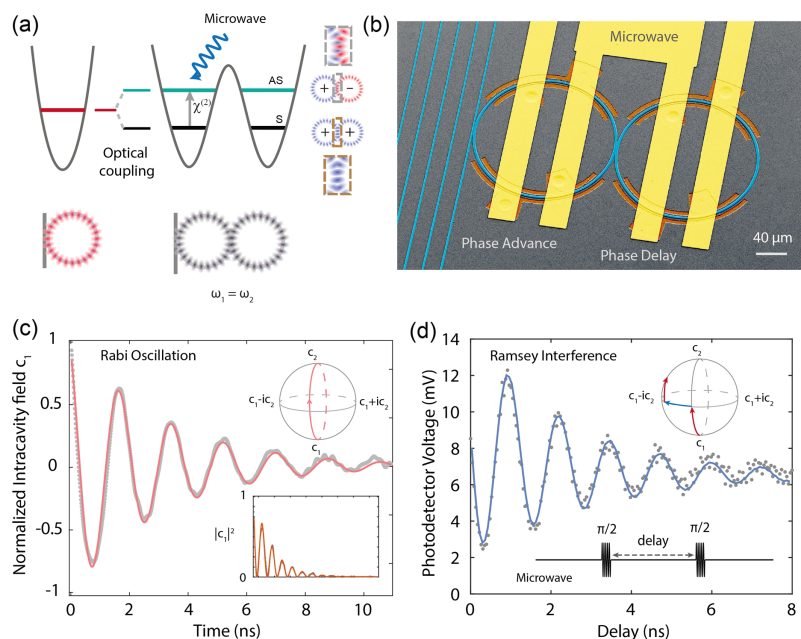
By forming hybrid modes, coupled resonators have resonance modes with energy splittings that are not determined by their intrinsic FSRs. Dynamical EO modulation of these resonators can induce transitions between these modes. The concept of a photonic two-level system was first demonstrated in 1998 [255]. Such artificial photonic molecules produce various optical phenomena and allow for nontrivial light control. In general, a photonic two-level system requires two optical resonance modes that are strongly coupled, so photons can transition from one mode to another before being dissipated. Recent progress in thin-film LN provides a great opportunity for this field, as high-Q resonators [11] offer the possibility of realizing long-lived photonic states, and the strong EO effect, in conjunction with the highly confined optical modes, enables efficient photonic transition.

Recently, a photonic two-level system was achieved using a pair of evanescently coupled LNOI microring resonators [173]. A fast index oscillation through electro-optic modulation leads to strong coupling between the two levels [Fig. 18(a)]. The Hamiltonian to describe such a system is $H = \omega_1 c_1{}^\dagger c_1 + \omega_2 c_2{}^\dagger c_2 + \Omega \cos(\omega_m t)(c_1{}^\dagger c_2 + \text{h.c.})$, where ω_1 and ω_2 represent the eigen-frequencies of the two optical modes in the coupled resonators, c_i and $c_i{}^\dagger$ are the annihilation and creation operators of the ω_i mode, Ω describes the coupling strength induced by microwave modulation, and ω_m is the microwave frequency. Based on this Hamiltonian, various phenomena such as Rabi oscillation, Ramsey interference, Autler–Towners splitting,

and Stark shifts were demonstrated in this device [Figs. 18(b)–18(d)]. In addition, the photonic molecule can be programmed into bright–dark mode photon pairs, allowing for photon storage and retrieval.

Coupled-resonator-based modulators also allow efficient frequency shifting and beam splitting at gigahertz scales. One approach to obtain complete frequency conversion is based on a generalized critical coupling condition [174]. Thus, the realization of photonic molecules in thin-film LN provides an opportunity to achieve fundamental functionalities for controlling the frequency degree of freedom of light. Specifically, an EO frequency shifter that works with CW optical input and continuous sinusoidal microwave drive was demonstrated, featuring a shift efficiency of ∼99% and an on-chip device insertion loss of 0.45 dB [174]. Under the generalized critical coupling condition, light injected at one frequency can be efficiently coupled from one frequency mode to another without back-conversion. Different from conventional single-sideband modulators, the coupled-ring shifter allows bidirectional frequency exchange of photons (i.e., frequency swap operation). This bidirectionality allows the device to be reconfigured as a tunable frequency beam splitter, in which the splitting ratio and frequency are controlled by microwave power and frequency, respectively. Such a frequency shifter and beam splitter allow coherent frequency control of photons, which are of particular interest to frequency-domain quantum computing [256]. In addition, extending the generalized critical coupling condition to a multi-level system is also proposed [174], which can lead to cascaded frequency shifting beyond 100 GHz using only several tens of gigahertz microwave drives.

Figure 18

Realization of a photonic molecule using coupled resonators in thin-film lithium niobate [173]. (a) Concept of the photonic molecule, where hybrid modes are formed by a pair of evanescently coupled microring resonators. The transition between the two modes can be induced by electro-optic modulation. (b) Scanning electron micrograph of a coupled-ring modulator that forms a photonic molecule. (c) Rabi oscillation and (d) Ramsey interference in the two-level system. Reprinted with permission from Zhang *et al.*, Nat. Photonics **13**, 36–40 (2019) [173]. Copyright the Author(s), under exclusive license to Springer Nature Limited 2018.

3.6. Cavity Electro-Optics

Combining electro-optically active optical resonators with low-loss microwave cavities—an approach known as cavity electro-optics [258–260]—can enable strong interactions between microwave and optical fields and create nearly quantum-limited modulation performance. Figure 19(a) illustrates a typical cavity EO device, such as those described in [175,176,257,261]. Two optical ring resonators form hybrid photonic molecule modes as described in Subsection 3.5. However, now the photonic molecule is driven by a microwave-frequency resonator (a lumped-element LC resonator in this case), with resonance frequency matched to the splitting between the hybrid optical modes. Additionally, this splitting can be tuned by a DC bias capacitor. The resonant enhancement of microwave power creates stronger optical modulation at the cost of a reduced bandwidth set by the linewidth of the microwave resonator. For example, one way to operate such a device is illustrated by the frequency-space diagram shown in Fig. 19(b), where a strong pump laser was tuned to be resonant with the red optical mode at frequency ω_-. An input microwave signal modulates the optical modes and induces resonantly enhanced sum-frequency generation into the blue optical mode at frequency ω_+, while the difference frequency at $\omega_- - \omega_m$ was suppressed as it is far off resonance. With this configuration, both the optical pump and the modulation sideband were resonantly enhanced. Not all cavity EO devices use this coupled-ring-resonator approach; other designs exploit neighboring longitudinal

Figure 19
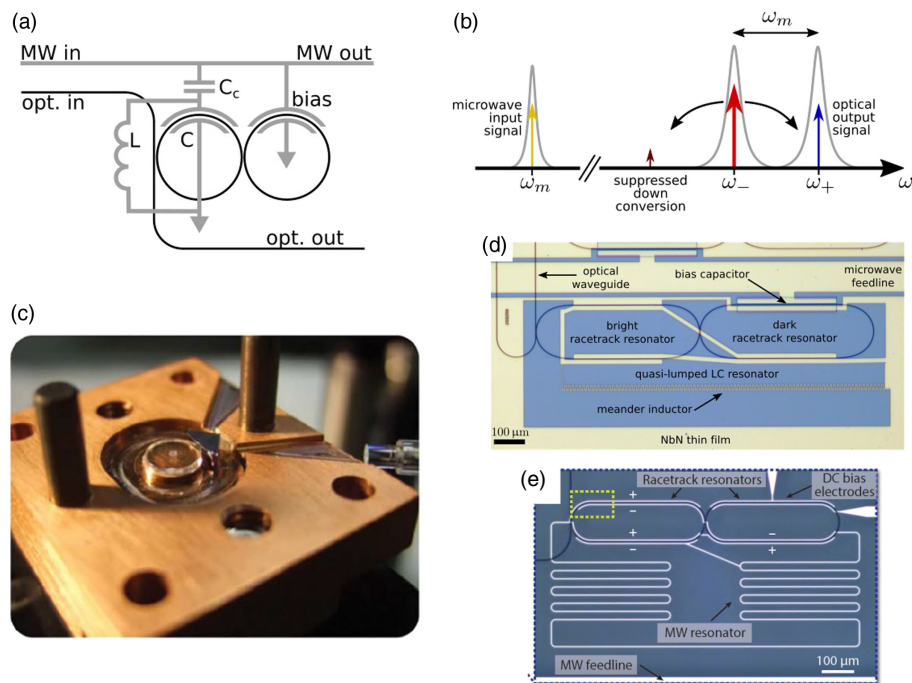
Cavity EO in lithium niobate. (a) Schematic diagram of a dual-ring cavity EO system [175]. (b) Frequency-space diagram showing microwave-optical transduction based on single-sideband modulation [175]. (c) Cavity EO transducer based on a polished LN whispering gallery mode resonator and a copper 3D cavity [257]. (d), (e) Cavity EO transducers using LNOI resonators and superconducting LC resonators [175,176]. (a), (b), and (d) Reprinted with permission from [175]. Copyright 2020 Optical Society of America. (c) Reprinted with permission from [257]. Copyright 2016 Optical Society of America. (e) Reprinted with permission from [176]. Copyright 2020 Optical Society of America.

[262] or transverse [188,257,263] optical modes of a single optical resonator, but the principle of operation is the same.

The main motivation for the development of such modulators is to achieve efficient transduction between microwave and optical fields to couple microwave super-conducting qubits to optical networks. Superconducting quantum devices have demonstrated rapid progress in recent years [264], which has encouraged interest in using them to create large-scale quantum networks. However, the microwave photons used to encode information in these devices are susceptible to strong thermal noise and attenuation at room temperature, which limits the practical size of such networks to something that can fit within a single cryogenic environment. Quantum interconnects [265] based on optical fiber links offer a way around this restriction, because they provide relatively weak attenuation and negligible thermal noise due to the high frequency of optical photons. A key component of such an interconnect is a quantum transducer that can convert single photons between microwave and optical frequencies. Several approaches have been studied to create such a transducer, which are described in several comprehensive reviews [266,267]. An approach based on the piezoelectric interaction in lithium niobate is described in Subsection 5.3a.

Cavity EO devices are particularly promising for this application because of their direct conversion mechanism (i.e., they do not rely on an intermediate form of energy, such as a mechanical excitation), which may enable higher efficiency and lower noise operation. The first cavity EO devices were based on bulk lithium-niobate whispering gallery mode resonators, such as that shown in Fig. 19(c) [257,260,263]. These devices benefit from low-loss optical modes (quality factor up to $\sim 10^8$), but the large size of the devices means that the EO interaction strength is comparatively weak. Thin-film LN offers relatively low loss (Q-factor up to $\sim 10^7$ [11]) and smaller optical modes, which can allow for a stronger EO interaction. Recently, cavity EO transducers in thin-film LN, shown in Figs. 19(d) and 19(e), have demonstrated microwave-to-optical photon conversion efficiency as high as 2×10^{-5} [175,176]. More recently, by mitigating the photorefractive effect and using a much higher pump power, on-chip conversion efficiency of 1% has been achieved [268]. While this still falls well below the limit required for direct quantum transduction, near-unity efficiency is expected to be feasible for optimized devices. We note that several other material platforms have also been investigated for cavity EO devices [188,262].

3.7. Synthetic Dimension Based on Electro-Optic Modulation

Synthetic dimensions allow the construction of high-dimensional spaces beyond the apparent geometric dimensions. It is of particular interest to study, for example, topological physics. In photonic systems, spectral synthetic dimension can be controlled under temporal modulation, in which different frequency modes form a synthetic lattice in the frequency domain. Such a temporal modulation provides coupling among the lattice points, which allows the creation of a frequency crystal. Realizing systems consisting of photonic synthetic dimensions typically requires the ability to simultaneously modulate multiple optical cavities or waveguides. LNOI is a suitable platform to investigate this field and push experimental realizations forward.

The key idea of synthetic frequency dimensions is to couple optical modes with different frequencies through dynamic modulation, as depicted in Fig. 20(a) [269]. For example, an EO modulation can create a time-dependent permittivity $\varepsilon(r, t) = \varepsilon_0(r) + \delta\varepsilon(r, t)$, where ε_0 and $\delta\varepsilon$ are the static permittivity and modulation-induced permittivity change, respectively. In the case of a harmonic microwave drive, the permittivity change follows $\delta\varepsilon(r, t) = \delta(r) \cos(\omega t + \phi)$, where ω and ϕ are the microwave frequency and phase. The temporally modulated system can be described

by the equation of motion $i\frac{d}{dt}a_n = ge^{i\phi}a_{n-1} + ge^{-i\phi}a_{n+1}$, where a_n represents the field amplitude of the nth mode, and g is the coupling strength [269].

Many theoretical studies have been conducted regarding forming synthetic dimensions through time modulation. These include Bloch oscillation in synthetic dimensions [271], demonstrating the photonic Weyl point [272], realizing a photonic gauge field in a synthetic dimension [273], generating high dimensionality in frequency space by folding a one-dimensional frequency crystal [274], and combining the synthetic dimension of frequency with physical dimensions [275] or with other synthetic dimensions [276]. Along with the rapid theoretical progress, experimental demonstrations of such synthetic dimensions have recently been explored in optical fiber systems. For instance, the band structure of a one-dimensional synthetic frequency crystal was theoretically investigated and experimentally probed [277]. Moreover, a combination of frequency and clockwise–counterclockwise modes was also realized in the fiber system, which led to a wide variety of physics [278].

Integrated photonics on LNOI provides a powerful platform for experimental realizations of frequency crystals. The theoretical investigation and experimental realization of high-dimensional frequency crystals with dimensions up to four was recently demonstrated [Fig. 20(b)] [270]. The density of states from one to four dimensions was formulated and probed for such frequency crystals [Fig. 20(c)]. Coherent random walks (quantum random walks with non-interacting photons) were also experimentally measured in one- and two-dimensional crystals.

In addition to frequency crystals, thin-film LN is also a promising platform to explore topological photonics, a rapidly emerging field. The concept of topological insulators originates from condensed matter physics, in which a bulk insulator can have a conducting state localized on its edge. Such edge states are robust to perturbation and defects due to the nontrivial topology of the band structure of the material. This

Figure 20
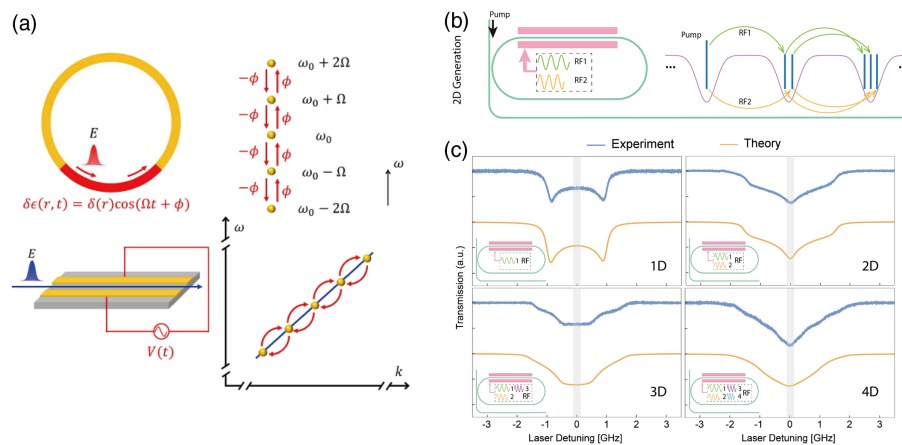
Realization of synthetic dimension [269] and high-dimensional frequency crystals [270] based on EO modulation. (a) A synthetic dimension can be achieved through EO modulation in a ring resonator or a waveguide. Different frequency modes are coupled by EO modulation and form a tight-binding lattice. (b) Concept of realizing high-dimensional frequency crystals in a single resonator. (c) Measurements of the density of the states of the frequency crystals with dimensionality ranging from one dimension to four dimensions. (a). Reprinted with permission from [269]. Copyright 2018 Optical Society of America. (b) Reprinted with permission from [270]. Copyright 2020 Optical Society of America.

concept has been transferred to photonics and resulted in various new phenomena including photonic topological edge states, topological lasing, etc. There have also been several theoretical studies related to topological photonics in synthetic crystals [279–287]. These proposals could be implemented using thin-film LN integrated photonics.

4. ALL-OPTICAL NONLINEARITY

LN possesses both second- and third-order nonlinearities and has a wide transparency window from the ultraviolet to the mid-infrared. The low linear propagation loss (both at visible and near-infrared) and absence of multiphoton absorption (for wavelengths above 800 nm) are of interest for ultrabroadband nonlinear processes even at very modest pump powers. In this section, we review recent demonstrations of harmonic generation, sum-frequency generation (SFG), difference-frequency generation (DFG), optical parametric generation, and four-wave mixing. Another unique potential offered by integrated LN photonic platform arises from the interplay between $\chi^{(2)}$ and $\chi^{(3)}$-based process, which can result in large effective third-order nonlinearity (due to cascaded second-order nonlinearity), self-referencing, dispersive-wave tailoring, and soliton compression.

At the heart of all nonlinear-optical interactions is the phase-matching condition. On the thin-film LN photonic platform, significant progress has been made in engineering group velocity, GVD, and modal phase matching at a wide range of wavelengths. More importantly, LN's ferroelectric property allows domain engineering (poling), which enables QPM. Combined with powerful dispersion engineering and cavity integration, nanophotonic PPLN could become a platform where a new branch of nonlinear science and applications will be born. In this section, we will cover dispersion engineering and phase matching in thin-film LN devices, and highlight several emerging applications in the classical and quantum domains.

4.1. Dispersion Engineering

Precise engineering of both the group velocity (GV) and GVD is a crucial step for utilizing the nonlinear properties of LN. In contrast to traditional LN waveguides, a thin-film platform allows the effective index of a waveguide mode to be tuned carefully by changing the waveguide geometry. Here, we illustrate how GV and GVD can be engineered by waveguide geometry. We also provide context for the importance of dispersion engineering and how it can be used for various nonlinear photonic applications.

The GVD (or β_2) of a material at a given frequency ω_0 can be written as $\beta_2 = (\frac{\partial^2 k}{\partial \omega^2})_{\omega=\omega_0}$, where $k = \frac{2\pi}{\lambda} \cdot n_{\text{eff}}$ is the wavevector with λ being the free-space wavelength [288]. Dispersion curves can be generated by simulating the effective index (n_{eff}) of transverse-electric (TE) and transverse-magnetic (TM) modes of a waveguide and numerically calculating the second derivative. Dispersion engineering on thin-film LN was first demonstrated in high-Q microring resonators with flexible GVD control [289] and has since been utilized for applications such as Kerr frequency comb generation [28] and supercontinuum generation [76].

Figure 21 illustrates how GVD can be engineered by tailoring the waveguide geometries, such as the waveguide width, etch depth, and initial LN film thickness [a typical LNOI waveguide cross section is shown in Fig. 21(b)]. Here, the dispersion curves are simulated using a finite-difference eigenmode (FDE) solver, and the material index is calculated from the Sellmeier equation for congruently grown bulk LN [290]. Figure 21(a) shows β_2 for bulk undoped LN in the ordinary and extraordinary crystal axes. In comparison to the bulk crystal, thin-film LN waveguides take

on a much larger range of β_2. Importantly, precise control of the dispersion curve through small variations in the geometry is invaluable in applications where near-zero (GVD ~ 0) dispersion or anomalous dispersion (GVD < 0) is desired.

Beyond these changes to the waveguide geometry, other configurations can also be explored. For example, an oxide layer is often deposited on top of the LN waveguide as a cladding, either to pull the optical mode further into the core of the waveguide or to make the structures more robust for additional fabrication procedures and post-process handling. The buried oxide layer beneath the LN film can also be removed to produce a suspended LN structure. These free-standing structures are important to leverage the piezoelectric properties of LN discussed later. The effect of the cladding on dispersion is summarized in Fig. 22, which shows the dispersion curve of the TE mode in the case of a suspended, air cladded, and oxide cladded structure for the same LN geometry.

GVD is critical for many nonlinear processes. For example, anomalous GVD is often required to achieve positive parametric gain via four-wave mixing for ultrabroadband optical spectral generation with a positive Kerr nonlinearity. Some of the most well-known examples are Kerr microcombs and supercontinuum generation. In a thin-film LN waveguide, the sign of GVD at the operating wavelength can be controlled by the waveguide geometry. LN is also attractive for Pockels microcombs where solitons can form at both the fundamental frequency and its second harmonic via $\chi^{(2)}$, or $\chi^{(2)}$ and $\chi^{(3)}$ interactions. The combination of GVDs at both frequencies reveals different nonlinear dynamics, as modeled in Ref. [291]. It is also known that PPLN can be used to generate an effective Kerr nonlinearity, the sign of which can be manipulated by
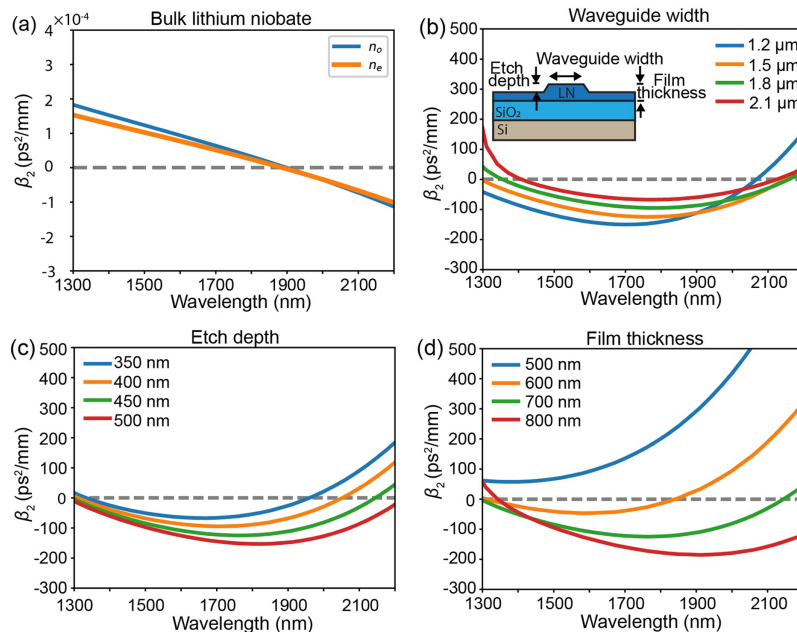
Figure 21

Illustration of geometric control of the waveguide dispersion. We compare the fundamental TE mode GVD for thin-film LN waveguides with different widths (b), etch depths (b), and initial film thicknesses (d) against LN's intrinsic material dispersion (a). The nominal waveguide configuration, as illustrated in the inset of (b), is based on 700-nm-thick, uncladded X-cut LN with etch angle of 60 deg, 1.5 μm top width, and etch depth of 450 nm.

choosing a positive/negative phase mismatch condition [292]. Therefore, thin-film PPLN offers additional knobs to engineer nonlinear-optical interactions.

In addition to the second-order derivative of the effective index (related to GVD), the first-order derivative (related to the GV) along with higher-order terms can also be engineered to achieve certain targeted nonlinear features. For example, zero GV mismatch between the fundamental and second-harmonic wavelengths is ideal for broadband SHG. In addition, minimal temporal walk-off is critical to achieve large effective $\chi^{(3)}$ and high conversion efficiency in cascaded $\chi^{(2)}$-based super-continuum generation via pulse pumping (Fig. 23). Higher-order dispersion has been studied extensively in integrated waveguides for modulation instability, soliton self-frequency shift, pulse generation, and dispersive-wave (DW) generation. For example, DW generation can be used to coherently enhance the spectral emission which is far detuned from the input light frequency. The position of the DW can be controlled via engineering the dispersion operator ($\hat{D}$), which consists of all the higher-order dispersion terms (Fig. 24). This has been utilized to generate visible and mid-infrared light via supercontinuum generation pumped by a near-infrared mode-locked laser [76,293,294].

4.2. Phase Matching

In $\chi^{(2)}$-mediated three-wave mixing processes, momentum is generally not conserved for the three frequencies involved due to material and waveguide dispersion. The momentum mismatch, also known as phase mismatch, for three-wave mixing is $\Delta k = k_1 + k_2 - k_3$, where $k_i = n_{\mathrm{eff}}(\omega_i)\,\omega_i/c$ is the propagation constant of the mode at frequency ω_i, $n_{\mathrm{eff}}(\omega_i)$ is the effective index of that mode, and c is the speed of light. The phase-matching condition, $\Delta k = 0$, must be met in order to achieve efficient energy transfer from the pump wavelength to the target wavelength(s) as light propagates through some length, L, of the nonlinear medium. When the phase-matching condition is not satisfied, energy will oscillate between the pump and target wavelength(s) with period $\Lambda = \frac{2\pi}{|\Delta k|}$, such that energy transferred to the target wavelength(s) is at most that accumulated over a propagation distance of $\Lambda/2$, regardless of the length of the nonlinear medium. Thus, in order to achieve efficient frequency conversion by taking advantage of the full propagation length through the nonlinear

Figure 22
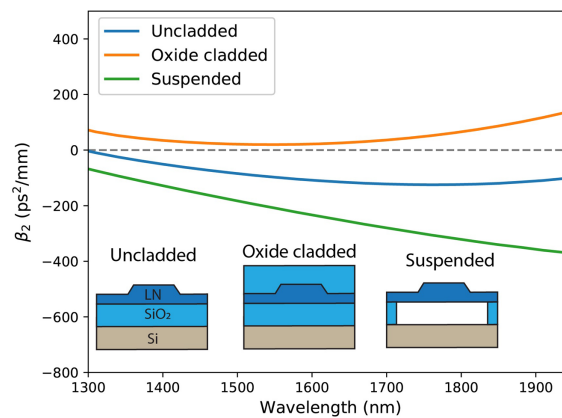
Effect of different cladding configurations on the TE mode dispersion of TFLN waveguides, including uncladded, 1-μm-thick SiO$_2$ top cladding, and suspended/free-standing structure. The LN waveguide follows the same geometric parameters as that in Fig. 21.

medium, one must engineer conditions under which phase matching is satisfied. Below are several ways in which phase matching can be achieved.

4.2a. Birefringent Phase Matching

At the heart of the phase mismatch problem is that in the typical dispersion regime of $\frac{dn_{eff}}{d\omega} > 0$, $n_{eff}(\omega_3) > n_{eff}(\omega_2) > n_{eff}(\omega_1)$ for $\omega_3 > \omega_2 > \omega_1$ if the light at all three frequencies follows the same dispersion curve. In a birefringent material such as LN, this occurs when the light at all three frequencies occupies the same polarization and

Figure 23
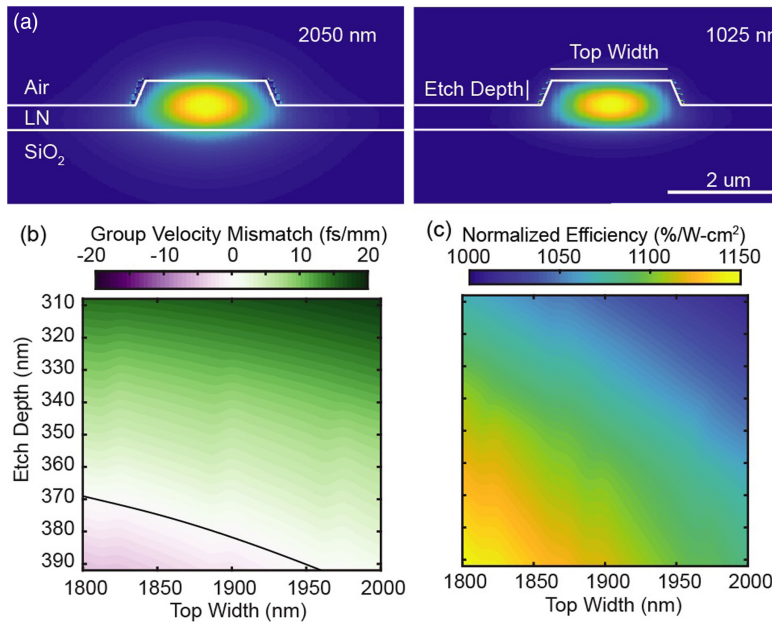
Group-velocity engineering for second-harmonic generation. (a) Waveguide cross section and optical mode profiles at the fundamental (left) and second-harmonic (right) wavelengths. (b) Simulated group-velocity mismatch as a function of waveguide top widths and etch depths. (c) Simulated normalized SHG efficiency. Reprinted with permission from [295]. Copyright 2020 Optical Society of America.

Figure 24
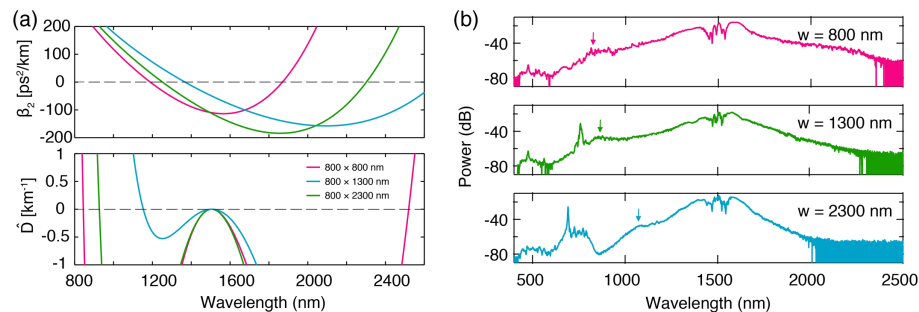
Engineering of higher-order dispersion for dispersive-wave generation. (a) Group velocity dispersion (β_2) and dispersion operator ($\hat{D}$) of air-clad LN rib waveguides of three different top widths. (b) Dispersive-wave generation via supercontinuum generation in LN waveguides with corresponding top widths in (a). The position of the dispersive wave (indicated by the arrows) can be predicted at near-zero crossings of the dispersion operator. Reprinted with permission from [76]. Copyright 2019 Optical Society of America.

spatial modes. In birefringent phase matching, $\Delta k = 0$ can be achieved by having one or more of the modes involved occupy a different polarization.

Since LN is a negative uniaxial material, the material index for light polarized along the ordinary axis at a particular frequency is always higher than that polarized along the extraordinary axis. Thus, the inequality $n_{\text{eff}}(\omega_3) > n_{\text{eff}}(\omega_2) > n_{\text{eff}}(\omega_1)$ can be broken by having one or both of ω_1 and ω_2 be polarized along the ordinary axis.

The polarization configuration in which both ω_1 and ω_2 are polarized along the ordinary axis, while ω_3 is polarized along the extraordinary axis, is known as type-I, whereas the configuration in which ω_1 is polarized along the ordinary axis while ω_2 and ω_3 are polarized along the extraordinary axis is known as type-II. Both configurations are commonly used to phase match $\chi^{(2)}$ frequency conversion in bulk crystals, and detailed treatments of how these are implemented in practice can be found in most textbooks on nonlinear optics, such as Ref. [288].

Birefringent phase matching is rarely used in LN integrated photonics, because it precludes frequency conversion mediated by the largest component of the $\chi^{(2)}$ tensor, $\chi^{(2)}_{zzz}$ or d_{33}, which is more than five times the second largest component of the $\chi^{(2)}$ tensor element. For interactions that make use of d_{33}, light at all of the three frequencies involved must be polarized along the extraordinary axis, i.e., type-0 polarization configuration, which can only be phase matched using other methods.

4.2b. Intermodal Phase Matching

One of the ways in which frequency conversion in the type-0 polarization configuration can be phase matched is through intermodal phase matching. Here, the inequality $n_{\text{eff}}(\omega_3) > n_{\text{eff}}(\omega_2) > n_{\text{eff}}(\omega_1)$ is broken by having one of the modes feature a different spatial profile, rather than polarization.

Intermodal phase matching is typically achieved by having light at ω_3 occupy a higher-order spatial mode, which will have a lower n_{eff} than the fundamental mode due to weaker confinement. Dispersion engineering by varying waveguide dimensions is employed to achieve intermodal phase matching for a specific set of frequencies. Intermodal phase SHG in the type-0 configuration has been demonstrated in both etched LN waveguides [117] and resonators [170] (see Fig. 25). Because of symmetry, the overlap integral of even and odd modes will be 0. As a result, fundamental and third-order modes are often used, such as that used in Fig. 25. This restriction can be removed by breaking the symmetry of the nonlinear material (e.g., replacing half of waveguides with a different material) [296]. Additionally, intermodal phase matching in other polarization configurations (e.g., type-I) has also been demonstrated [297] (see Subsection 4.3a).

4.2c. Quasi-Phase Matching

While intermodal phase matching can enhance frequency conversion efficiency by allowing the use of the largest $\chi^{(2)}$ tensor component, it incurs a significant penalty from smaller mode overlap between the higher-order spatial mode(s) and the fundamental spatial mode(s) [31]. Thus, for optimal $\chi^{(2)}$ frequency conversion efficiency, two conditions must be satisfied: first, light at all three interacting frequencies must occupy the same polarization and spatial mode, and, second, the process must be phase matched. However, these two conditions are in tension, since, as previously noted, phase matching requires that at least one of the interacting frequencies occupies a different spatial and/or polarization mode. One solution to this dilemma is to employ QPM rather than to attempt true phase matching via either birefringent or modal phase matching.

In QPM, $\Delta k \neq 0$ for the three-wave mixing process, allowing for the interacting frequencies to occupy the same polarization and spatial mode. However, the efficient power transfer between the pump and target wavelength(s) is recovered by inverting the sign of the relevant $\chi^{(2)}$ tensor component with period $\Lambda = \frac{2\pi}{|\Delta k|}$. Thus, the sign of $\chi^{(2)}$ is inverted every $\Lambda/2$ of propagation distance, thereby preventing energy backflow into the pump. Equivalently, one can think of inverting $\chi^{(2)}$ as imparting an additional grating momentum $K = 2\pi/\Lambda$ that is equal, and opposite, to the intrinsic momentum mismatch Δk to achieve momentum conservation.

Periodic poling. Quasi-phase matching can be achieved in ferroelectric materials, where the orientation of the ferroelectric domains (and thus $\chi^{(2)}$) can be inverted by applying high voltage pulses in a process called poling. Popular nonlinear-optical materials that can be periodically poled include LN, lithium tantalate (LiTaO$_3$), and potassium titanyl phosphate (KTP).

The techniques for fabricating bulk PPLN are mature and have been commercialized. However, since bulk PPLN fabrication techniques rely on being able to pattern electrodes on the $\pm z$ faces of LN, techniques for PPLN fabrication on thin-film LNOI are somewhat more complicated and have only been explored in recent years.

The coercive field required for poling LN varies with material composition and doping. In general, congruently grown undoped LN typically requires a higher coercive field for domain inversion [298–300], as compared to near-stoichiometric undoped LN [299]. Doping with magnesium oxide (MgO) decreases the coercive field in both congruent and stoichiometric LN [298]. It has been reported that thin-film LN requires a higher coercive field than the corresponding bulk crystals [17,18,301,302]. It was thought that the increased coercive field could be caused by the bonding interface between the thin-film LN and buried SiO$_2$ [17], which hinders the domain inversion, or due to the Li$^+$ out-diffusion during the annealing process in LNOI fabrication [303], which reduces the Li concentration and increases the coercive field.

In Z-cut LNOI, there are two methods for PPLN fabrication: (1) poling before bonding LN to the carrier substrate and (2) direct poling on thin-film LN. In the first case, bulk LN is poled with standard bulk LN poling techniques, and then sliced and bonded onto a carrier substrate using the Smart-Cut process. This method was used in one of the earliest demonstrations of thin-film PPLN [35] and several other demonstrations

Figure 25
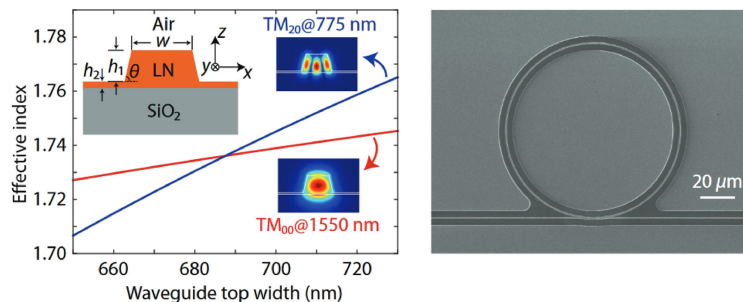
Intermodal phase matching in a microring resonator between the fundamental TM$_{00}$ spatial mode at the fundamental frequency and TM$_{20}$ higher-order spatial mode at the second harmonic. Left, dispersion curve and mode profile; right, scanning electron micrograph of the ring resonator. Figures 1(b) and 1(d) reprinted with permission from Luo *et al.*, Phys. Rev. Appl. **11**, 034026 (2019) [170]. Copyright 2019 by the American Physical Society.

subsequently [168,304–306]. Poling directly on thin-film LN has also been demonstrated recently. One way is to use an atomic force microscope (AFM) tip to apply a high local electric field for domain inversion [161]. This method can achieve feature size down to 100 nm. The other way is to pattern electrodes on top of the thin film (with some buffer dielectric material), and pole through the LN/oxide/handler wafer stack at an elevated temperature [167].

In X/Y-cut LNOI, PPLN fabrication is typically done with surface electrodes in the form of coplanar gratings. While developed initially for a hybrid platform with rib-loaded waveguides [17,18], this method has since been used to fabricate PPLN ridge waveguides. Poling in these cases is typically done before waveguide fabrication [29], though poling after waveguide fabrication has also been demonstrated with hybrid waveguides [307] and shallowly etched monolithic ridge waveguides [308]. The latter case allows active monitoring of the poling process using the generated optical signal at the waveguide output [308]. The former case requires more complex imaging setups to achieve real-time monitoring of the poling process, such as *in situ* confocal second-harmonic microscopy [309]. Poling periods as short as 600 nm have recently been demonstrated [310]. It is worth mentioning that X/Y-cut PPLN only allows the poling grating to be along one direction, as the domain inversion needs to be in the Z axis, while Z-cut PPLN allows arbitrary directions in the xy plane (e.g., radial gratings for poled ring).

There are three main methods to visualize poled domains: (1) selective etching, (2) piezoresponse force microscopy (PFM), and (3) second-harmonic microscopy.

Selective etching is a common technique for verifying poled domain structures [311]. This method uses HF to etch the exposed faces normal to the poling direction (Z face). Differently poled regions etch at different rates, resulting in a set of "hillocks" that indicate different domains and can be imaged conventionally. Figure 26(a) shows an example of selective etching of a poled waveguide [302], where a focused ion beam was used to mill a trench in the X-cut sample to expose the Z faces, and an HF etch was applied. The left image shows incompletely poled domains that do not reach the bottom of the LN film, while the right image shows completely poled domains. While this method provides information about the three-dimensional structure of the poled domains (including depth into the crystal), its major drawbacks are its destructive nature and the amount of time required to expose the relevant faces, etch them, and then image them.

PFM is a non-invasive domain imaging technique. A probe is touched to the surface of a sample and an AC electrical field is applied, which induces surface oscillations due to the converse piezoelectric effect [313]. Domains of different polarization have a different electromechanical response, providing the contrast mechanism. While this method gives high-resolution data on the shapes of poled domains at the surface of the material [see Fig. 26(b)], it does not provide depth information, and image acquisition is relatively slow, on the order of tens of seconds.

Second-harmonic microscopy to evaluate poling quality has the advantage of speed while delivering adequate resolution. Second-harmonic light from domains of opposite polarization is fully out of phase, resulting in destructive interference at the boundaries between domains and thus dark regions in the second-harmonic image. Due to resonance effects in the layer structure, the degree of contrast may depend on the wavelength [314]. Figure 26(c) shows an example of a second-harmonic microscopy image of a periodically poled X-cut waveguide [312]. Detailed simulations of

the second-harmonic signal have opened up the possibility of non-destructively infer-ring poling depth from second-harmonic microscope images, though the resolution is limited [34].

Indirect optical poling diagnostic methods have also been exploited by monitoring the output optical signal from the waveguides while poling. One way is to monitor phase modulation in the waveguide [307]. In principle, at 50% duty cycle, no phase modulation should be observed when an electric field is applied (through a sepa-rate set of electrodes than the poling electrodes) across the waveguide (along the Z crystal axis). The average poling duty cycle can be inferred from the change in phase of the out-coupled light. This method can be utilized while poling and provides path-averaged information that can be complemented by examination of local poling quality using second-harmonic microscopy. Another *in situ* monitoring technique is to inject CW light into a waveguide and monitor the second-harmonic signal in the out-coupled light as poling proceeds. This has been used to optimize poling schedules by, e.g., poling and depoling a waveguide multiple times until the second-harmonic signal was saturated [308].

4.2d. Other Phase-Matching Approaches

Cyclic phase matching. Cyclic phase matching (CPM) [315] is often used in ring or microdisk cavities to achieve type-I phase matching. When the crystallographic axis is not the symmetry axis, for example, on a X/Y-cut LN thin film, the effective nonlinearity and the refractive index of in-plane polarized light are changing as light propagates in the microring resonator ([315–317]). In a type-I SHG process, there are

---

Figure 26
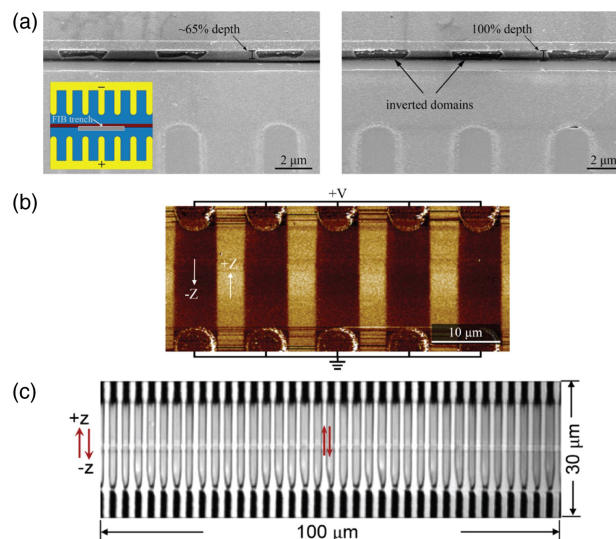
Characterization of poled domains in LN. (a) Selective etching [302], where focused ion beam was used to mill a trench in the X-cut waveguide to expose the Z faces followed by HF etching. (b) Piezoresponse force microscopy [302]. This method can provide detailed information on the surface but without poling depth information. (c) Second-harmonic microscopy [312], where the domain boundaries appear as dark lines and the brightness of the poled region infers poling depth. The faint gray hori-zontal line across the image is a shallow-etched waveguide. (a), (b) Reprinted with permission from [302]. Copyright 2019 Optical Society of America under the terms of the OSA Open Access Publishing Agreement. (c) Reprinted with permission from [312]. Copyright 2020 Optical Society of America under the terms of the OSA Open Access Publishing Agreement.

four positions along the ring in which phase matching can be achieved. Compared to type-I SHG when the Z axis is the symmetry axis, CPM can enable a much broader phase-matching bandwidth (only certain discrete wavelengths would satisfy phase matching within this bandwidth) but at a sacrifice of conversion efficiency. In addition, the modulated effective nonlinearity must also be included in the model, and the fact that SHG in different phase-matched regions can constructively or destructively interfere leads to a wavelength-dependent gain profile [315]. SHG with a normalized conversion efficiency of 0.1%/mW was demonstrated in a double-resonant X-cut LN whispering gallery microresonator [146], and CPM-based spontaneous parametric downconversion (SPDC) has been reported in a X-cut LN microdisk resonator [158]. A CPM-based process generally suffers from lower conversion efficiency as compared to a QPM-based one given the same resonance condition.

It is also possible to achieve type-0 effective QPM in such a cyclic fashion. For example, all participating waves can be in quasi-TE modes inside an X-cut microdisk [150]. As they circulate around the microdisk, they experience an effective nonlinear coefficient with a sign inversion every half cycle, mimicking QPM in PPLN. At the same time, the effective indices for all participating waves vary at different azimuthal angles. Similar to CPM, this produces a wide range of Δk and results in a broader phase-matching bandwidth but with sacrificed efficiency as compared to standard QPM in PPLN.

Metasurface-assisted phase-matching-free SHG. Dielectric metasurfaces can be used to achieve phase-matching-free SHG [318]. This method utilizes Si nanoantennas fabricated on the top surface of a LN waveguide to create a unidirectional phase gradient. When the pump light at ω_0 in the fundamental TE mode is converted to its second harmonic at $2\omega_0$ in the fundamental TE mode, the gradient metasurface couples the $2\omega_0$ light into its higher-order spatial modes. The unidirectional effective wavevector created by the dielectric metasurface prevents these $2\omega_0$ signals from converting back to their fundamental spatial modes, and the small mode overlap between these higher-order $2\omega_0$ modes and fundamental pump modes prevents them from downconverting to ω_0. Therefore, even in the absence of phase matching, the power transfer from the pump to the second harmonic is unidirectional, which results in broadband enhancement of SHG efficiency. A normalized conversion efficiency of 1,660% /W·cm^2 has been achieved at telecom wavelengths. The drawback of this approach is that collecting the higher-order spatial modes is generally inefficient.

Periodically grooved quasi-phase matching. Besides periodic poling, periodically perturbing the waveguide width in the form of grooves can also achieve QPM [117,319]. This change of the waveguide width induces periodic modulation in both the effective index and the nonlinear coefficient along the propagation direction, providing a momentum "kick" that compensates for the phase mismatch. The added grooves, however, cause Bloch scattering loss. In general, deeper grooves result in higher nonlinear conversion efficiency due to tighter confinement, but also cause larger Bloch loss.

4.3. Second-Order Nonlinear Wavelength Conversion

Second-order nonlinearity enables frequency generation and wavelength conversion through SFG, DFG, SHG, and optical parametric oscillation. Moreover, it can also be used to generate non-classical states of light through SPDC. These operations have been accomplished in bulk LN crystal or microscale waveguides, with much based on periodic poling. Here, we review recent demonstrations in thin-film LN waveguides and microcavities, especially with periodic poling, which are continuously pushing the nonlinear efficiency to higher records.

4.3a. Traveling-Wave Processes

As discussed, the efficiency of the aforementioned parametric frequency conversion processes is greatly enhanced in nanophotonic PPLN waveguides compared to their bulk counterpart. This is because the normalized conversion efficiency of, for instance, SHG, scales as $\frac{P_2}{P_1^2} \propto (\frac{\zeta}{(A_1\sqrt{A_2})^{1/3}})^2$, where P is the power, A is the mode area, subscripts 1 and 2 denote the fundamental wave and second harmonic, respectively, and ζ is the mode overlap between the fundamental and second-harmonic waves; details on calculating ζ, A_1, and A_2 can be found in Ref. [297]. Since mode areas A_1 and A_2 can be more than an order of magnitude smaller in nanophotonic waveguides compared to bulk waveguides, the conversion efficiency can be much higher in nanophotonic waveguides if all other parameters are held equal. Thus, nanophotonic PPLN waveguides allow one to achieve conversion efficiencies comparable to those of bulk waveguides with a much shorter length. This is desirable not only for its compactness, but also because the phase-matching bandwidth will be broader, as the phase-matching bandwidth is inversely proportional to the interaction length.

Since the absolute (quasi-)phase matched SHG conversion efficiency in PPLN waveguides scales as $P_2/P_1 \propto P_1/L^2$, where L is the length of the waveguide, the figure of merit for (quasi-)phase matched SHG is typically given in terms of the normalized conversion efficiency $\eta = \frac{P_2}{P_1^2 L^2}$, which has units of $W^{-1}\,m^{-2}$ and is commonly expressed in %/W·cm^2.

To date, ultra-high normalized conversion efficiencies have been achieved in both SiN$_x$ loaded waveguides and monolithic LN ridge waveguides via type-0 QPM. In the former case, high normalized conversion efficiency of 1160%/W·cm^2 was achieved in a 5 mm SiN$_x$ loaded waveguide on PPLN by engineering the waveguide cross section to limit leakage of the fundamental TE mode to TM slab modes [320]. In the latter case, ultra-high normalized conversion efficiency of 4600%/W·cm^2 was achieved in a 300-µm-long LN ridge waveguide through the use of active monitoring of the second-harmonic signal to achieve optimal poling [308]. Longer PPLN ridge waveguides up to 4 mm have also been demonstrated [29,32], albeit with lower normalized conversion efficiencies (<3000%/W·cm^2) due to a non-optimal poling duty cycle (i.e., <50% duty cycle) and non-uniform poling. Figure 27 shows some typical poling setups for X-cut LNOI PPLN waveguides.

Additionally, $\chi^{(2)}$ frequency conversion has also been demonstrated in unpoled LN ridge waveguides with type-I modal phase matching [297]. Such a configuration sacrifices conversion efficiency as it uses a smaller component of the $\chi^{(2)}$ tensor, and has lower mode overlap ζ, but has a higher thermal tuning range than phase matching done in the type-0 polarization configuration. Improvements to conversion efficiency while retaining broad thermal tunability can likely be achieved by using type-I QPM rather than type-I modal phase matching for higher mode overlap.

Table 5 summarizes some representative works on non-resonant based second-harmonic generation in thin-film LN waveguides.

4.3b. Resonant Processes

Optical cavities can strongly enhance these parametric conversion processes given the same optical pump power. Taking SHG ($\omega_1 \rightarrow \omega_2$) in a ring resonator as an example, to achieve optimal conversion efficiency, the following conditions need to be satisfied: (1) energy conservation and multi-resonance, $\omega_2 = 2\omega_1$, with both frequencies on resonance, where the subscripts 1 and 2 indicate fundamental and second harmonics; (2) momentum conservation, $m_2 = 2m_1$, where $m_{1/2}$ are the azimuthal mode numbers; (3) large effective second-order nonlinear susceptibility; (4) large mode overlap inside the nonlinear material; (5) small effective mode area;

(6) small cavity length (i.e., small mode volume); (7) high intrinsic quality factors; and (8) critical coupling. Detailed derivation and mathematical formulas can be found in Refs. [170,321]. Ideally, one would prefer all participating waves to be in their fundamental transverse modes, polarized along the Z crystal axis to utilize $d_{33}(\chi_{zzz})$ and tightly confined in the resonator with maximum modal overlap. However, material dispersion often compromises phase matching. This problem can be alleviated by QPM through periodical poling, where the momentum conservation requirement is relaxed to $m_2 = 2m_1 + M$ with $M = 2\pi R/\Lambda$ being the domain period number, R being the ring radius, and Λ being the poling period. Most importantly, the key advantage of resonance-enhanced wavelength conversion relies on its capability of circulating the optical waves. Under doubly resonant and critically coupled conditions, the conversion efficiency enhancement can scale as $\sim Q_1^2 Q_2$, where Q_1 and Q_2 are the Q-factors of the fundamental and second-harmonic modes.

In microring resonators, the dispersion can be engineered similarly to that in waveguides by adjusting the waveguide width, etch depth, and film thickness as well as crystal cut. Without periodic poling, modal phase matching is often adopted [169,170]. For example, in Z-cut microrings, the fundamental wave is usually the

Figure 27
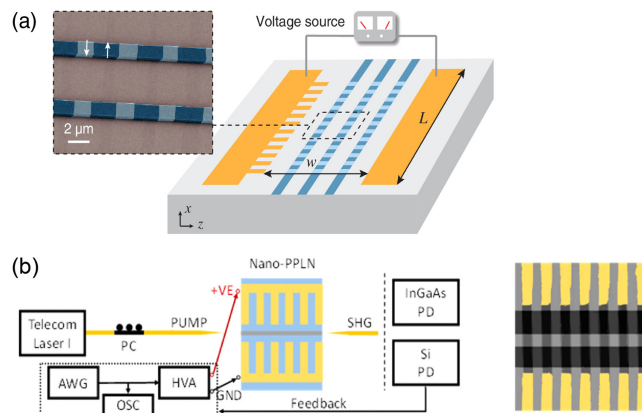
PPLN waveguide frequency converters. (a) Poling schematic for X-cut LN film before waveguide etching, and false color SEM of resultant etched waveguides with duty cycle of $\sim(39 \pm 3)$%. (b) Schematic for actively monitored poling of etched LN nanophotonic waveguide and false color AFM image of resultant 50% domain duty cycle. (a) Reprinted with permission from [29]. Copyright 2018 Optical Society of America. (b) Reprinted with permission from [308]. Copyright 2019 Optical Society of America.

Table 5.   Representative Works on Non-Resonant-Based Second-Harmonic Generation in Thin-Film LN

| Device Type	Crystal Cut	Phase Matching	Normalized Conversion Efficiency (%/W · cm²)	Year	Ref.
SiNx loaded waveguide	X	Type-0 QPM	160	2016	[17]
SiNx loaded waveguide	X	Type-0 QPM	1,160	2019	[320]
Etched waveguide	X	Metasurface assisted	0.4	2017	[318]
Etched waveguide	Z	Type-I intermodal	22.2	2018	[297]
Etched waveguide	X	Type-0 intermodal	41	2017	[117]
Etched waveguide	X	Type-0 (periodically grooved)	6.8	2017	[117]
Etched waveguide	X	Type-0 QPM	2,200	2019	[32]
Etched waveguide	X	Type-0 QPM	2,600	2018	[29]
Etched waveguide	X	Type-0 QPM	4,600	2019	[308]

fundamental quasi-TM (TM_{00}) mode, and the second harmonic can be a higher-order quasi-TM (e.g., TM_{20}) mode. This conversion thus utilizes the largest nonlinear coefficient d_{33}. Note that mode symmetries need to be conserved to ensure non-zero overlap. With this approach, Luo *et al*. demonstrated telecom to visible SHG with a conversion efficiency of 1.5%/mW as well as DFG at telecom wavelengths (here, the efficiency is no longer normalized by length for cavity-based processes) [170]. It is worth mentioning that temperature can also be used to effectively fine tune the phase matching [169].

Recent progress on PPLN microrings and racetracks has brought SHG conversion efficiencies to an unprecedented level. In 2019, Chen *et al*. demonstrated a periodically poled racetrack resonator on an X-cut MgO-doped LN thin film [30] [see Fig. 28(a)]. The poling is applied on one of the 300-μm-long straight waveguide sections. This configuration allows all waves to be in their fundamental quasi-TE modes and utilizes the largest nonlinear coefficient d_{33}. Quasi-phase-matched SHG with conversion efficiency of 230%/mW is achieved, corresponding to an efficiency of 10^{-6} per single photon. The equivalent single-photon efficiency is calculated as $\eta_s = \eta E_{ph}/\tau$, where η is the conversion efficiency in units of W^{-1}, E_{ph} is the pump photon energy, and τ is the cavity lifetime. In the same year, Lu *et al*. demonstrated radially poled, Z-cut microring [31] [see Fig. 28]. A single pulley waveguide was designed to efficiently couple both the infrared and visible frequency bands. Due to fabrication-limited poling period, $TE_{00}-to-TM_{00}$ SHG was adopted, utilizing d_{31}. Nonetheless, an ultra-high on-chip SHG efficiency of 250%/mW was achieved. More recently, the same group further improved the Z-cut PPLN microring and realized a more ideal poling period of 2.95 μm [167]. This allowed for QPM SHG with all waves in their fundamental quasi-TM modes to utilize d_{33}. As a result, a record-high SHG efficiency of 5,000%/mW was achieved in the low-power regime, reaching a single-photon nonlinearity approaching 1%.

Besides racetrack and microring cavities, on-chip whispering gallery resonators (including microdisks and wide-waveguide ring-shaped resonators) and photonic crystal cavities have also been studied extensively for $\chi^{(2)}$ nonlinear wavelength conversion.

In high-Q microdisks, various $\chi^{(2)}$-nonlinear processes have been demonstrated, including SHG [140,152,157], SFG [151,159], and SPDC [158]. Furthermore, effective third-order nonlinear phenomena have been observed as a result of cascaded $\chi^{(2)}$

Figure 28
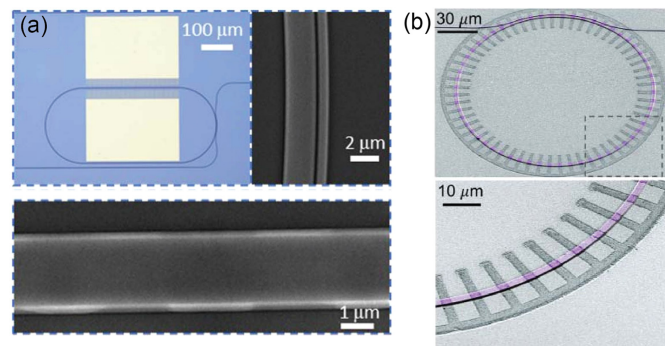
PPLN racetrack and microrings. (a) PPLN racetrack resonator in X-cut LNOI, where the poling was applied along the straight section of the racetrack. (b) Radially poled Z-cut microring resonator. (a), (b) Reprinted with permission from [30,31]. Copyright 2019 Optical Society of America.

processes. For example, third-harmonic generation (THG) has been demonstrated through cascaded SHG and SFG [149,150]; effective four-wave mixing has been demonstrated as a result of cascaded SHG and DFG [160].

Microdisks support abundant resonance modes, differing by their polarization states, as well as azimuthal and radial mode numbers. It is thus convenient to satisfy the multi-resonance condition, where the wavelengths involved in the wave-mixing processes coincide with cavity resonances. However, efficient phase matching is nontrivial. Most $\chi^{(2)}$ processes demonstrated in Z-cut LN microdisks rely on modal phase matching [140,149,160], where the largest nonlinear tensor element d_{33} is not used. In X-cut LN microdisks, CPM is commonly involved [146,152,158], where the fundamentals are quasi-TE modes and the second harmonic is at a quasi-TM mode. An effective QPM can also be achieved in X-cut microdisks when all waves are at quasi-TE modes, interacting through d_{33} but with an oscillating sign. Under this scheme, SHG with an efficiency of 9.9%/mW and THG with an efficiency of 1.05%/mW^2 were measured [150]. Recently, periodic poling has also been applied to Z-cut LN microdisks [161]. With a bottom layer acting as a poling electrode, PFM was used to achieve a poling period of ~ 2 μm. Using the PFM method, the same group further demonstrated dual-period poling with unit domain size as small as 90 nm in width, and observed SHG, THG, and even fourth-harmonic generation [162]. However, the conversion efficiency remains moderate (0.05%/mW) due to limited Q and non-optimal mode overlap and confinement.

In addition, in high-Q (3×10^6 at 976 nm), large (200 μm diameter), and wide (7 μm) ring-shaped whispering gallery resonators, a mixture of nonlinear processes was observed, including SHG of the pump light, cascaded stimulated Raman scattering, SHG of the Raman signal, and SFG between the pump and Raman signal [94]. Periodic poling was also applied to this Z-cut on-chip whispering gallery resonator, which showed improved SHG efficiency of 0.09%/mW [168], limited by the nonideal poling configuration and external coupling.

Photonic crystals support a high Q-factor ($\sim 10^5$) while maintaining ultra-small mode volume $\sim (\lambda/n)^3$. They strongly enhance optical interactions and are ideal for nonlinear photonic applications. The first SHG in LN photonic crystals was demonstrated in free-standing L3 (three missing air holes) LN photonic crystals fabricated from bulk LN substrate [178]. Subsequently, LNOI wafers were utilized to realize both 1D [179] and 2D photonic crystals [142] and to demonstrate SHG as well as SFG. So far, the conversion efficiency remains low (current record of 0.078%/W [142]), since the fundamentals and harmonics (or sum frequency) are not on resonance simultaneously. In fact, it has been a big challenge to achieve multiple resonances simultaneously in such a different wavelength regime (i.e., IR and visible). Recent progress on doubly resonant photonic crystal cavities may solve this problem [322] and lead to ultra-efficient nonlinear conversions or even single-photon nonlinearity. Another challenge is that photonic crystals are more susceptible to photorefractive effects due to the strong local field intensity. This problem will limit its use in classical applications but may be less prominent in the quantum regime, where only single or few photons are in the cavity.

In Table 6, to give context to cavity-enhanced frequency conversion using LNOI, we summarize recent work on cavity-based SHG, mentioning the cavity type, crystal cut, phase-matching type, and conversion efficiency.

4.3c. Spontaneous Parametric Downconversion

In addition to demonstrations of classical $\chi^{(2)}$ wavelength conversion processes, SPDC, an exclusively quantum process in which a pair of photons is generated from

a single pump photon, has also been demonstrated on the thin-film LN platform in microdisks [158], PPLN waveguides [32–34,323], and PPLN rings [324]. A high coincidence-to-accidental ratio (CAR) of 668 ± 7 has been achieved at a pair generation rate of 12 MHz in Ref. [34] in a 5 mm PPLN waveguide on X-cut LNOI. Photons generated via SPDC in PPLN waveguides generally exhibit strong energy-time entanglement, which can be leveraged to produce entangled photon pairs in multiple wavelength channels to enable frequency-domain multiplexing; this has been demonstrated in a submillimeter PPLN waveguide with signal–idler pairs generated over a coarse wavelength division multiplexing grid separated by more than 120 nm [33]. Entangled photon pairs generated via SPDC can also be used as sources of heralded single photons, though the spectral purity of the heralded photon has yet to be precisely evaluated in experiments [34,325].

4.4. Cascaded Second-Order Nonlinearity

In addition to the intrinsic cubic third-order nonlinearity, phase-mismatched second-order processes can induce an effective Kerr nonlinearity due to back-action of the second-harmonic (SH) wave at 2ω on the fundamental wave (FW) at ω. It originates from the occurrence of two successive second-order nonlinear processes: upconversion to SH at 2ω via SHG and then downconversion back to the FW at ω, which results in a nonlinear phase shift of the FW that is proportional to $[\chi^{(2)}]^2$ [326]. In the presence of phase mismatch Δk between the FW and SH, this effective third-order nonlinearity $\chi_{\mathrm{eff}}^{(3)}$ is approximately proportional to $-[\chi^{(2)}]^2/\Delta k$. More importantly, $\chi_{\mathrm{eff}}^{(3)}$ can be tuned to either a positive or negative value by engineering the QPM condition in PPLN waveguides ($\Delta k = k_{\mathrm{SH}} - 2k_{\mathrm{FW}} - k_{\mathrm{QPM}}$). Soliton generation might be possible in the visible spectral range, where the normal GVD of the material is typically too large to be overcome by the waveguide dispersion on integrated platforms. In addition, at near-phase-matching condition, a giant $\chi^{(3)}$, which equals $\chi_{\mathrm{Kerr}}^{(3)} + \chi_{\mathrm{eff}}^{(3)}$, can be achieved to significantly reduce the pump power for third-order nonlinear frequency conversion, such as four-wave mixing [149,327]. Jankowski *et al.* achieved $\chi_{\mathrm{eff}}^{(3)} \sim 200$ times higher than the intrinsic $\chi_{\mathrm{Kerr}}^{(3)}$ of LN at 2050 nm using an integrated PPLN waveguide [295]. The nonlinear parameter $\gamma \sim \chi^{(3)}/A_{\mathrm{eff}}$, where A_{eff} is the effective mode area, defines the strength of a Kerr nonlinear interaction, and is largely enhanced in nanophotonic waveguides. Therefore, thin-film-LN-based cascaded second-order processes open up exciting opportunities, including realizing dynamical processes typically associated with $\chi^{(3)}$ nonlinearities using extremely low pump

Table 6.   Representative Works on Cavity-Based SHG in Thin-Film LN

| Device Type	LN Crystal Cut	Phase Matching	Conversion Efficiency (%/W)	Year	Ref.
Microdisk	Z	Intermodal	0.28	2017	[149]
Microdisk	Z	Intermodal	10.9	2014	[140]
Microdisk	X	Cyclic	0.36	2017	[158]
Microdisk	X	Cyclic	2.3	2018	[152]
Microdisk	X	Cyclic	110.6	2016	[146]
Microdisk	X	Cyclic	990	2019	[150]
Ring-shaped WGM resonator	Z	Type-0 QPM	0.9	2018	[168]
Microdisk	Z	Type-0 QPM	1.44	2020	[161]
Microdisk	Z	Type -0 QPM	51	2020	[162]
Racetrack	X	Type-0 QPM	230,000	2019	[30]
Microring	Z	Type-I QPM	250,000	2019	[31]
Microdisk	Z	–	1.35	2015	[157]
Microring	Z	Type-0 QPM	5,000,000	2020	[167]
Photonic crystal L3 cavity	X	–	0.012	2016	[178]
1D photonic crystal	X	–	0.0004	2018	[179]
2D photonic crystal	X	–	0.078	2019	[142]

powers. Recent demonstration [295] reports a multi-octave-spanning supercontinuum spectrum with a few pJ of pulse energy.

This capability of tailoring the effective nonlinearity offers incredible flexibility for controlling nonlinear dynamics when combined with dispersion engineering of integrated photonics. For example, group-velocity mismatching (GVM, $\Delta k'$) or the temporal walk-off between the FW and SH is the dominant factor of the SHG bandwidth ($\Delta \lambda \sim 1/|\Delta k'|L$, where L is the PPLN waveguide length). Realization of cascaded second-order processes in a group-velocity-matched regime ($\Delta k' \sim 0$) would tremendously boost both Kerr-based spectral broadening and the conversion bandwidth of SH light. Reference [295] has shown efficient QPM SHG with less than 100 fJ pulse energy, and a 3-dB SHG bandwidth $>$ 110 nm, an order of magnitude broader than using conventional PPLN technologies (Fig. 29). In addition, there is still a rich group of nonlinear dynamics that can be explored in dispersion-engineered PPLN waveguides, such as large nonlinear phase shift, laser mode-locking, soliton compression, spatial soliton waves, Cherenkov radiation, nonlinear mirrors, GVM-induced Raman radiation, and Kerr microcombs [326,328–334]. Almost all of the nonlinear interactions will benefit from the extra degree of freedom in control of GVM, PM, GVD at both FW and SH, and even higher-order dispersion terms. For example, cascaded phase shifts through interaction with femtosecond pulses can be operated under both the stationary and nonstationary regimes [328], which is determined by the GVM characteristic length, the SHG coherence length, and the SH GVD length [335]. These regimes have been intensively studied for cascaded quadratic soliton compressors [328,329] and frequency shifting using controllable Raman-like nonlinearities [334]. Further study of the many dynamical processes that can be accessed by engineering the waveguide dispersion in conjunction with QPM is the subject of ongoing research.

4.5. Kerr Comb

Optical frequency combs have a wide range of applications, such as precision spectroscopy, frequency metrology, and optical communications. While they are traditionally produced through pulse trains emitted by a mode-locked laser, microresonator frequency comb generation, wherein the comb teeth are formed at the resonator mode frequencies via nonlinear processes in the cavity, is quickly maturing as a field. The most common process is Kerr frequency comb generation, which makes use of the $\chi^{(3)}$ optical nonlinearity and high circulating optical power to generate comb lines through four-wave mixing. Locking to Kerr solitary waves (solitons), which balance

Figure 29
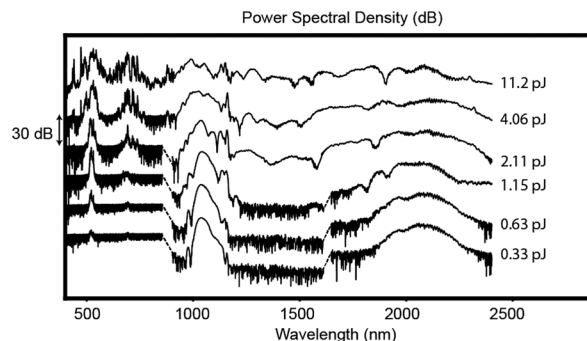
Supercontinuum spectra at various pulse energies, assisted by cascaded second-order nonlinearity in a PPLN waveguide. Reprinted with permission from [295]. Copyright 2020 Optical Society of America.

third-order nonlinearity and dispersion, as well as cavity loss and gain [336], can often produce octave-spanning combs for $f - 2f$ referencing.

Kerr frequency comb generation promises a compact, low-footprint comb source, and when utilized carefully, the Kerr process can produce highly coherent low-noise spectra. Thin-film LN is of particular interest for chip-based frequency comb generation due to its capability of hosting an entire photonic circuit on a single chip [Fig. 30(a)]. Included in the photonic circuit are various components, such as EO resonance tuning and on-chip self-referencing, that leverage LN's EO and $\chi^{(2)}$ properties. These properties are usually missing in other material platforms used for frequency comb generation, leading to the need for bulky off-chip components for full functionality.

Kerr combs spanning 700 nm were demonstrated on the LNOI platform using X-cut LN wafers [28]. The waveguide geometry was engineered for anomalous dispersion in both TE and TM modes, and frequency combs were successfully demonstrated on both. For the crystal cut used in this work, the TE mode was favorable, as it can utilize r_{33} of LN. However, we see in the TE comb spectrum [Fig. 30(b)] many peaks from the strong Raman effect in this polarization, corresponding to scattering off of various phonon branches. The Raman effect is strongest when the light is polarized along the crystal's Z axis [172] and competes with the four-wave-mixing process used to generate the comb.

The combination of optimized $\chi^{(2)}$ performance and maximized Raman gain in the same polarization has caused a conundrum in functional Kerr comb generation, as the strong Raman effect can prevent soliton mode-locking. To mitigate the interference of Raman, frequency combs can be generated along the non-polar axis of the material or around a longer optical wavelength where the Raman effect is known to be weaker, or with a larger FSR to avoid overlapping with the highest Raman gain wavelength. The former two solutions have been used to achieve stable soliton combs using the TE mode of Z-cut LN [27,171]. Furthermore, a soliton microcomb spanning > 200 nm at 1.5 μm [Fig. 30(c)] and > 300 nm at 2 μm has been achieved by avoiding Raman scattering effects [Fig. 30(d)].

Figure 30
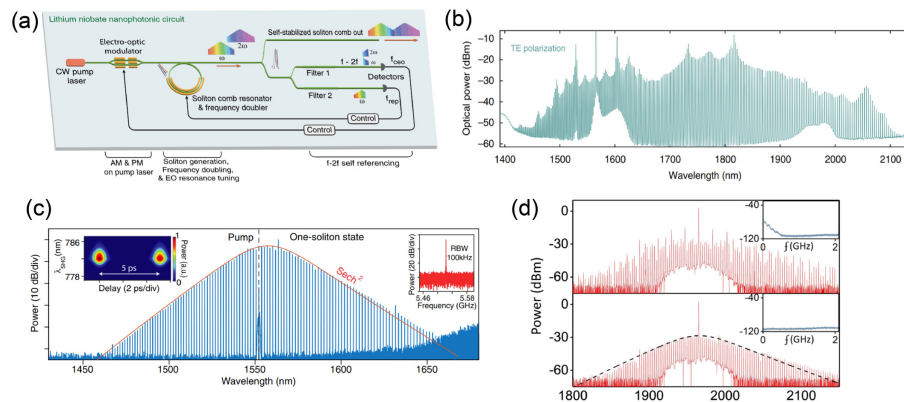
(a) Conceptual schematic of a full LN nanophotonic circuit for Kerr comb generation on chip, including soliton pulse formation, resonator tuning, frequency doubling, and f-2f self-referencing [27]. (b) Raman–Kerr combs demonstrated on X-cut LN [28]. (c) Soliton comb on Z-cut LN at 1.5 μm [27]. (d) Soliton Kerr combs on Z-cut LN generated at 2 μm in order to mitigate strong Raman gain [171]. (a), (c), (d) Reprinted with permission from [27,171]. Copyright 2019 Optical Society of America. (b) Reprinted by permission from Macmillan Publishers Ltd.: Wang *et al.*, Nat. Commun. **10**, 978 (2019) [28]. Copyright 2019.

There are a number of challenges unique to Kerr frequency combs on the LNOI platform that must be considered before octave-spanning combs can be realized. Most importantly, a means of mitigating or bypassing the strong Raman effect along the crystal polar axis to achieve soliton formation remains to be demonstrated. Additionally, at high optical powers required for Kerr comb generation, the photorefractive and thermo-optic effects in LN act in opposition to each other, requiring careful consideration to the tuning procedures for locking onto the soliton state. Recently, 4/5 octave-spanning Kerr combs have been reported in a-Z-cut LN microresonator with a 335 GHz line spacing [337]. It is achieved by engineering the waveguide-ring coupling to raise the Raman oscillation threshold [338] and utilizing a relatively large FSR. There are also recent studies on controlling the photorefractive effect by thermal annealing and cladding removal, which could help stabilize the cavity resonance at high optical powers [339].

4.6. Raman Lasing

Raman spectroscopy is a common way of investigating the structural information of LN through analysis of its vibrational transitions. It is also commonly used to obtain the crystallinity, surface quality, doping, strain, and other properties of LN crystal [340–344]. Raman scattering has various configurations depending on the propagation directions and polarization of both the pump and Stokes light with respect to the crystal axis of LN [345–348]. There are two branches of Raman-active phonon modes, which are A symmetry and E symmetry. The A mode is polarized along the Z crystal axis, and the E mode polarized in the X–Y plane [349]. There are both longitude and transverse modes in A and E symmetries. In addition, there exist both forward and backward scattering processes, and forward Raman scattering corresponds to a polariton effect where photons and phonons are strongly mixed and leads to electromagnetic radiation [350].

While Raman spectroscopy is an indispensable tool for material study, Raman oscillation plays an important role in nonlinear dynamics in LN crystals, and has been observed in LN microdisks and whispering gallery resonators [152,351]. A detailed study of Raman oscillations is reported in monolithic X-cut LN microring and racetrack cavities pumped by a CW laser [172]. The dominant stimulated Raman scattering was found to be counterpropagating with respect to the pump, and several scattering configurations were explored [Fig. 31(a)]. Here, the strongest Raman gain was found when the polarization of the pump was parallel to the Z crystal axis, where both the EO and $\chi^{(2)}$ are the largest. This potentially leads to a strong energy transfer from the pump to the Stokes light if high optical power is used in LN nonlinear-optical and EO devices. Figure 31(b) shows the competition between four-wave mixing and Raman oscillations in a CW pumped LN microresonator [171].

We note that there exist discrepancies of Raman oscillation strength among the work in thin-film LN devices [27,171,172]. The variation in the wavelength and linewidth of Raman peaks could be attributed to differences in fabrication processes of the thin-film LN devices, such as annealing [341], RIE, electron-beam lithography, and the Li/Nb concentration ratio of the material. The study of stimulated Raman scattering in the thin-film LN waveguides is of importance to building LN nonlinear photonic circuits.

4.7. Supercontinuum Generation

Supercontinuum generation is a nonlinear-optical interaction in which an input optical pulse undergoes enormous spectral broadening in a waveguide due to various processes including self-phase modulation, cross-phase modulation, four-wave mixing,

and dispersive-wave generation [352]. Over the past decade, there has been tremendous development of integrated photonic platforms that enable supercontinuum with moderate pump powers [353–361]. In particular, integrated photonics is well suited for the generation of coherent broadband optical spectra, as the high material nonlinearity, along with tight optical confinement, allows for efficient supercontinuum generation with sufficiently short pulses using a short waveguide length [362–366]. The generation of a coherent, octave-spanning spectrum is critical for applications in time and frequency metrology, and optical clocks, where a fully stabilized frequency comb source is required. Many of these comb sources rely on the stabilization of the repetition rate and the carrier-envelope offset frequency (f_{CEO}) of a mode-locked laser [367]. The f_{CEO} can be detected using a self-referencing technique based on $f - 2f$ interferometry, which needs a coherent, octave-spanning spectrum [368–370], and this broadband spectrum is achieved through supercontinuum generation. While on-chip supercontinuum technology has become mature, the $f - 2f$ interferometry is usually performed off-chip using bulk optics. In recent years, there have been demonstrations of f_{CEO} detection using on-chip $f - 2f$ interferometry, which leverages simultaneous supercontinuum and second-harmonic generation in a single waveguide [371–373].

In thin-film LN, through dispersion engineering, a strong second-harmonic signal along with a broadband coherent supercontinuum can be generated simultaneously due to the large intrinsic $\chi^{(2)}$ and $\chi^{(3)}$ nonlinearities [76,374]. Accordingly, coherent two-octave-spanning supercontinuum generation and f_{CEO} detection through the spectral overlap of the generated second harmonic and supercontinuum spectrum were achieved [76]. Numerical modeling of the pulse propagation [293] dynamics in the LN waveguide showed that the system can be described using a reduced scalar nonlinear envelope equation [375–377]

$$\left[\frac{\partial}{\partial z} - i \sum_{n \geq 2} \frac{\beta_n}{n!} \left(i \frac{\partial}{\partial t} \right)^n + \frac{\alpha}{2} \right] E(z, t) = i \frac{\omega_0}{2 n_0 c \varepsilon_0} \left(1 + i \tau_{\mathrm{sh}} \frac{\partial}{\partial \tau} \right) P_{\mathrm{NL}}(z, t), \quad \textbf{(6)}$$

Figure 31
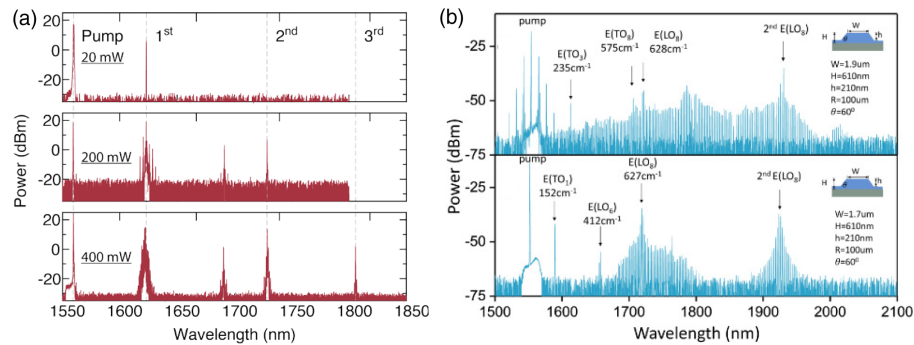
Raman oscillations in LN microresonators. (a) Three Raman spectra at different pump powers of 20, 200, and 400 mW [172]. The polarization of both the Stokes and pump light is along LN's Z axis. The Raman oscillation is found to be dominant in the backward propagating direction with respect to the pump. (b) Optical spectrum of Raman–Kerr combs generated in LN microresonators, where the corresponding phonon modes are labeled [171]. No evidence of soliton formation is observed while scanning the pump laser across the resonance. (a) Reprinted with permission from Yu *et al.*, Light Sci Appl **9**, 9 (2020) [172]. Copyright the Authors(s) 2020, licensed under a Creative Commons Attribution 4.0 International License. (b) Reprinted with permission from [171]. Copyright 2019 Optical Society of America.

where β_n corresponds to the nth-order dispersion coefficient, α is the linear propagation loss, ω_0 corresponds to the pump frequency, $\tau_{\text{sh}} = 1/\omega_0 - \partial[\ln(n(\omega))]/\partial\omega|_{\omega=\omega_0}$ is the optical shock time, $P_{\text{NL}} = \varepsilon_0[\chi^{(2)}E^2 + \chi^{(3)}E^3]$ is the total nonlinear polarization with contribution from only non-negative frequencies, τ is the local time in the moving frame, and $E(z, t)$ is the field at position z and time t. This equation can model the dynamics of light in LN waveguides spanning multi-octave bandwidths through the combined $\chi^{(2)}$ and $\chi^{(3)}$ nonlinearities, taking into account the birefringent nature of LN in solving the effective refractive index and nonlinearity [378]. Figure 32 shows the simulated pulse propagation dynamics in a 0.5-cm-long dispersion-engineered LN waveguide fabricated from a 800-nm-thick X-cut LN thin film [293]. Here, the pump was a 90 fs pulse train centered at 1560 nm with a pulse energy of 107 pJ. As the pulse propagates in the waveguide, the second-harmonic and third-harmonic components were immediately generated. The main pulse undergoes spectral broadening through self-phase modulation. For $z > 4$ cm, a dispersive-wave component is generated near 860 nm that continues to blue shift due to phase matching and approaches the second-harmonic component. Dispersive-wave generation is a phase-matched nonlinear process in which energy from the pump is transferred across a zero-GVD point, and is commonly used to extend the overall generated spectral bandwidth [379–381]. The position of the dispersive wave can be approximated by considering the zero crossing of the dispersion operator $\hat{D} = \sum_{n\geq 2} \frac{\beta_n(\omega_0)}{n!}(\omega - \omega_0)^2$.

An integrated LN $f - 2f$ interferometer is demonstrated for stabilizing the f_{CEO} of a mode-locked fiber laser [293]. The waveguide output was directly sent to a Si avalanche photodiode for f_{CEO} detection, and a feedback loop was implemented for stabilization. Figure 33 shows (a) the generated supercontinuum spectrum and (b) the single-sideband phase noise of the measured f_{CEO} beat note. This approach drastically simplified the conventional approach for $f - 2f$ interferometry, which consists of a bulk PPLN with a temperature controller and a delay line for compensation of the temporal walk-off between the f and $2f$ spectral components, and offers promise towards the realization of a fully integrated frequency comb source.

Figure 32
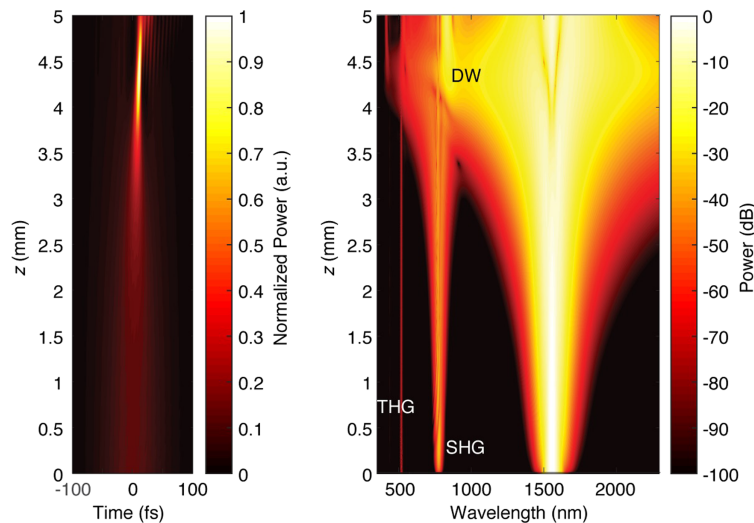
Numerical modeling of pulse propagation dynamics in a 0.5-cm-long LN waveguide. Plot shows temporal (left) and spectral (right) evolution. The waveguide cross section is 800×1250 nm. DW, dispersive wave; SHG, second-harmonic generation; THG, third-harmonic generation. Reprinted with permission from [293]. Copyright 2020 Optical Society of America.

Furthermore, the extension of the spectral bandwidth, through a combination of dispersive-wave generation, harmonic generation, and DFG, yielded an ultrabroadband supercontinuum generation spanning 0.35 to 4.1 μm with 240 pJ pulse energy in Ref. [294]. Specifically, the spectral components in the visible were generated through SHG and SFG, along with cascaded SHG, which allowed for spectral generation down to the UV regime. In addition, the spectrum extended into the mid-IR regime via DFG. The generation light from UV to mid-IR wavelengths in a single LN device promises the development of an integrated ultrabroadband source for spectroscopy applications.

Lastly, there has been a demonstration of a novel approach for broadband supercontinuum generation in an integrated PPLN waveguide via cascaded nonlinearities [295]. This approach utilizes quasi-phase matched $\chi^{(2)}$ interactions to enable broadband SHG with 3 dB bandwidths >110 nm and effective self-phase modulation with nonlinearities that are 200 times larger than the intrinsic $\chi^{(3)}$ nonlinearity in LN. Such large nonlinearities allow for the generation of a supercontinuum spectrum spanning 2.5 octaves with pulse energies as low as 10 pJ. Further details are given in Subsection 4.4.

5. PIEZO-OPTOMECHANICS

Optomechanics [382] provides an efficient interface between light and elastic waves, via photoelastic and moving boundary interactions. The recent development of piezo-optomechanics further links elastic waves and microwaves on thin-film piezoelectric materials. Such integrated piezo-optomechanical devices utilize electrically driven acoustic waves to deflect, modulate, and frequency control the light while demonstrating superior performance to conventional bulk acousto-optic components.

An ideal material for piezo-optomechanics should possess strong piezoelectricity and photoelasticity, as well as low mechanical and optical losses. Commonly used

Figure 33
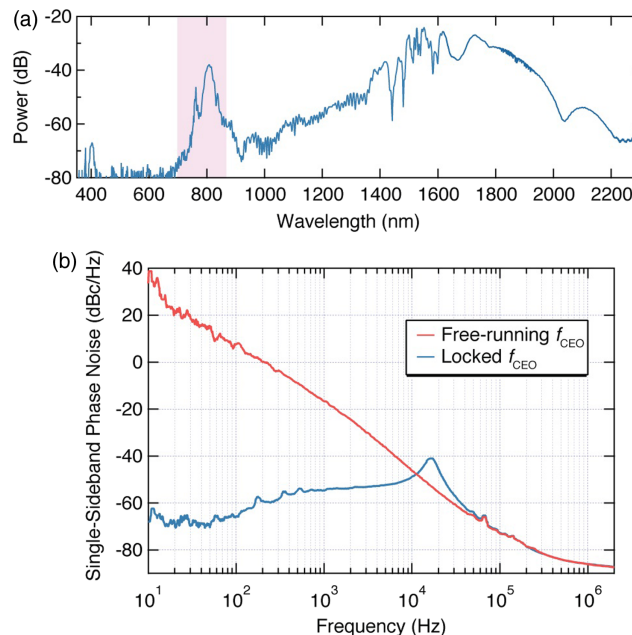
On-chip $f - 2f$ interferometer. (a) Experimental supercontinuum spectrum. The region shaded in pink is used for $f - 2f$ interferometry. (b) Single-sideband phase noise of the $f_{\rm CEO}$ for free-running (red) and locked (blue) states. Reprinted with permission from [293]. Copyright 2020 Optical Society of America.

piezoelectric materials include zinc oxide (ZnO), AlN, GaAs, and LN, which are non-centrosymmetric materials. While all of these materials have similar photoelasticity, and have been used to demonstrate high-Q optical cavities, LN shows the highest piezoelectric coefficient.

Other piezoelectric materials with stronger piezoelectricity and/or photoelasticity, such as lead zirconate titanate (PZT) and tellurium dioxide (TeO$_2$), could further improve the efficiency of piezo-optomechanical devices, should high-quality thin films with low optical loss be available. TeO$_2$ is widely used in bulk acousto-optic modulators (AOMs), but nanofabrication of TeO$_2$ is challenging and needs further development [383,384].

Heterostructures, which use one material for piezoelectric coupling and another material for optimized optomechanical coupling, have also been explored for piezo-optomechanics. For example, acoustic waves generated on bulk LN have been used to measure the elasto-optic coefficients of an arsenic trisulfide (As$_2$S$_3$) thin film over-laying on LN [385]. Piezo-optomechanical coupling between superconducting qubits and optical cavities using AlN on Si has been achieved [386], benefiting from the well-developed Si optomechanics platform.

Heterogeneous integration of LN thin film could also benefit piezo-optomechanics, and this is discussed further in Subsection 5.2. For example, taking advantage of the high acoustic velocity in diamond (19 km/s in bulk diamond, compared to 8 km/s in bulk LN), LN thin film on diamond could achieve mechanical frequencies of $>$40 GHz. Piezoelectrically generated acoustic waves in LN could efficiently drive the spin qubits of color centers in diamond. Similarly, point defects in SiC have also been explored for spin-acoustic wave interactions [387].

5.1. Piezoelectricity and Photoelasticity

Since the piezo-optomechanical coupling strength depends on both the piezoelectric and photoelastic tensors, the design of piezo-optomechanical devices is challenging. Control and manipulation of elastic waves in thin-film LN could be even more complicated. Fortunately, LN SAW technology has been developed for several decades for its use in mobile communication systems [388], which provides valuable experience and insight into the design of piezo-optomechanical devices.

Due to the anisotropy of LN, SAW devices use a variety of crystal orientations such as X, Z, 42°-Y, and 128°-Y. While optical fields in LN with X or Y polarization have the same ordinary refractive index, the acoustic phase velocities in the X, Y, and Z directions are all different. Therefore, the choice of crystal orientation significantly changes the performance of piezo-optomechanical devices. While most published work chooses the crystal orientation of LN thin film based on its commercial availability, the optimal device orientations might be different for piezoelectric and optomechanical couplings. Thus, piezo-optomechanical devices can have two parts with different orientations then connected using an acoustic waveguide [177]. This suggests that there is room for further investigation, and a comprehensive study of LN crystal orientations for piezo-optomechanical devices would be valuable to the community.

Determined by its point group of 3 m, the piezoelectric coefficient tensor d_{ij} of LN is given by

$$\begin{bmatrix} 0 & 0 & 0 & 0 & d_{15} & -2d_{22} \\ -d_{22} & d_{22} & 0 & d_{15} & 0 & 0 \\ d_{31} & d_{31} & d_{33} & 0 & 0 & 0 \end{bmatrix}, \tag{7}$$

and the photoelastic tensor is given by

$$
\begin{bmatrix}
p_{11} & p_{12} & p_{13} & p_{14} & 0 & 0 \\
p_{12} & p_{11} & p_{13} & -p_{14} & 0 & 0 \\
p_{31} & p_{31} & p_{33} & 0 & 0 & 0 \\
p_{41} & -p_{41} & 0 & p_{44} & 0 & 0 \\
0 & 0 & 0 & 0 & p_{44} & p_{41} \\
0 & 0 & 0 & 0 & p_{14} & p_{66}
\end{bmatrix}.
\tag{8}
$$

The experimentally measured values are included in Table 1.

Since the piezoelectricity of LN is strong, the secondary electro-optic effect, which is caused by the electric field generated by the elastic wave via piezoelectricity, plays a significant role in the overall coupling from microwaves to light. The contribution of this secondary electro-optic effect can be more than one third of the overall coupling.

5.2. Microwave Acoustic Modes

Several approaches based on LN have been pursued to implement piezo-optomechanical systems. General considerations include efficient piezoelectric excitation of acoustics waves, large optomechanical coupling, and low acoustic wave propagation loss. Figure 34 illustrates various acoustic waves used in LN piezo-optomechanical systems.

5.2a. Surface Acoustic Waves on Bulk LN

SAWs on bulk LN substrates are low-loss propagating elastic waves confined to the surface of LN, which can be efficiently generated by interdigital transducers (IDTs). The propagation loss is typically 1–7 dB/mm at gigahertz frequencies at room temperature, and about one order of magnitude lower at cryogenic temperatures [389–391]. However, bulk LN substrates cannot confine optical modes. Thus, Ti-indiffused layers, deposited higher optical index materials, or material-on-oxide layers are needed to guide the optical light on the chip.

Figure 34
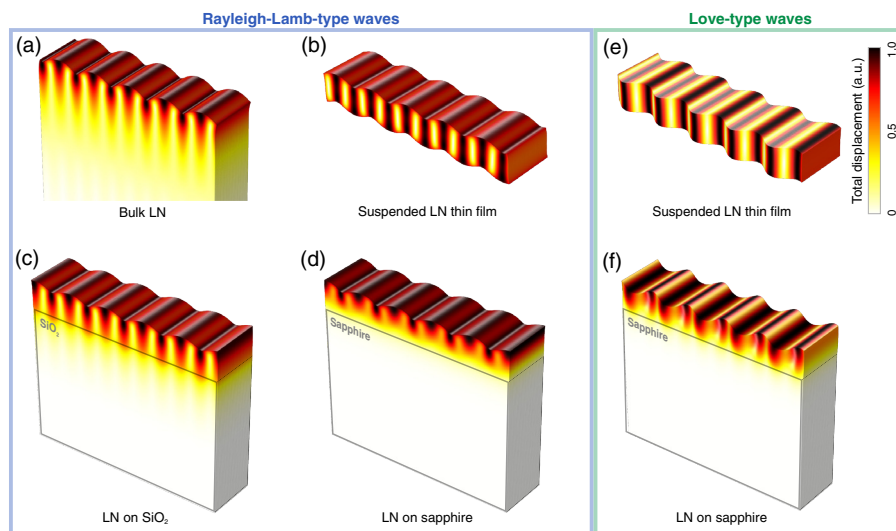
Total displacement profiles of typical acoustic waves used in LN piezo-optomechanics. There are (a)–(d) Rayleigh–Lamb-type and (e), (f) Love-type shear waves on (a) bulk LN substrate; (b), (e) suspended LN thin film; (c) LN on SiO_2; and (d), (f) LN on sapphire.

An acousto-optic frequency shifter (AOFS) has been demonstrated employing Ti-indiffused optical waveguides on bulk LN substrate [392]. Since there is almost no acoustic contrast between regions with and without Ti indiffusion, the optical waveguides defined by Ti indiffusion do not reflect SAW or scatter SAW into bulk acoustic waves. This is important for building integrated AOFSs or non-reciprocal optical devices, in which the unwanted SAWs would generate other unwanted side-bands or degrade the isolation. However, the optical contrast formed by Ti indiffusion is also limited, and thus the optical mode size is large, for example, $\sim 10{-}100\ \mu m^2$. For high-frequency applications, with the acoustic frequency in the gigahertz range, the acoustic wavelength is $<1\ \mu m$, which results in reduced mode overlap and, hence, interaction between the optical and the acoustic waves. This limits the efficiency of the acousto-optic devices.

To improve interaction between optical and acoustic waves, overlay layers on bulk LN can be used to guide the light, while the generation and propagation of the SAW are still mainly in the LN substrate. Such devices do not rely on LNOI wafers, and feature a more robust and compatible fabrication that avoids etching of LN. The optomechanical coupling happens either in the overlaid optical waveguides, whose strain fields are driven by the SAW on LN substrate, or in the LN substrate by the evanescent optical fields.

This configuration provides an opportunity to achieve overall efficient piezo-optomechanical coupling by overlaying materials with high photoelastic coefficients for optical waveguides. However, it is challenging to form high-Q acoustic resonators using this approach, since the top optical waveguide inevitably scatters the SAW into bulk acoustic waves, especially when the acoustic wavelengths are comparable to the size of optical waveguides.

5.2b. Surface Acoustic Waves on LNOI

As both the optical and acoustic indices (inverse phase velocities) of LN are higher than the SiO_2 layer underneath, thin-film LN-on-oxide can simultaneously confine optical and acoustic modes. Compared to suspended thin-film LN, LNOI can handle larger RF powers. For example, using similar IDT structures, up to $\sim 100\ mW$ microwave power can be delivered to suspended LN thin films, while more than 1 W of microwave power can be delivered when thin-film LN is on top of an oxide layer [393].

With optical waveguides defined by etching thin-film LN, waveguide-based AOMs have been demonstrated [Figs. 35(f) and 35(g)] [394–396]. However, similar to the overlaid waveguides on bulk LN substrate, the optical waveguide structure defined on the LN thin film can scatter acoustic waves, especially when the acoustic wavelength becomes comparable to the structure feature sizes (e.g., etch depth). Thus, such devices usually work at sub-gigahertz acoustic frequencies and have limited Q and fQ products for the acoustic resonances.

Ti-indiffused waveguides on thin-film LN could potentially be used to reduce the acoustic scattering while providing optical waveguiding. Alternatively, optical confinement in the lateral dimension could be eliminated (while maintaining vertical confinement provided by thin-film LN), thus allowing light to propagate as a 2D "free-space" beam (a slab-waveguide mode). Recently developed integrated LN AOFSs [393,398] employ such "free-space" regions and achieve high-purity frequency shifting.

LNOI also has some limitations for piezo-optomechanics. Since the acoustic contrast between LN and oxide is small, thin-film LN-on-oxide only confines a few

acoustic wave modes, for example Rayleigh-like modes. However, Rayleigh modes are not the most effective modes for optomechanical coupling due to their strain profile (see Fig. 34). The top of the thin film sees a tensile strain, and the bottom sees a compressive strain, and the induced optical index changes would be partially cancelled out in the overlap integration with the optical mode. Also, oxide is not a good thermal conductor, and thus limits the stability of devices under high RF power inputs.

5.2c. LN on Sapphire

Since the acoustic velocity of sapphire is much higher than LN, LN on sapphire supports more interesting acoustic modes than LN on oxide [390]. For example, X-cut LN on sapphire supports shear waves (Love waves) propagating in the crystal Y direction. Unlike the aforementioned Rayleigh mode, shear modes create strain from top to bottom of the thin film with the same sign, and thus the induced optical index change adds constructively in the overlap with the optical mode. This particular shear acoustic mode, whose major strain component is e_{YZ} (index 4 in the reduced representation), employs the high piezoelectric coefficient $d_{24} = d_{15}$,

Figure 35
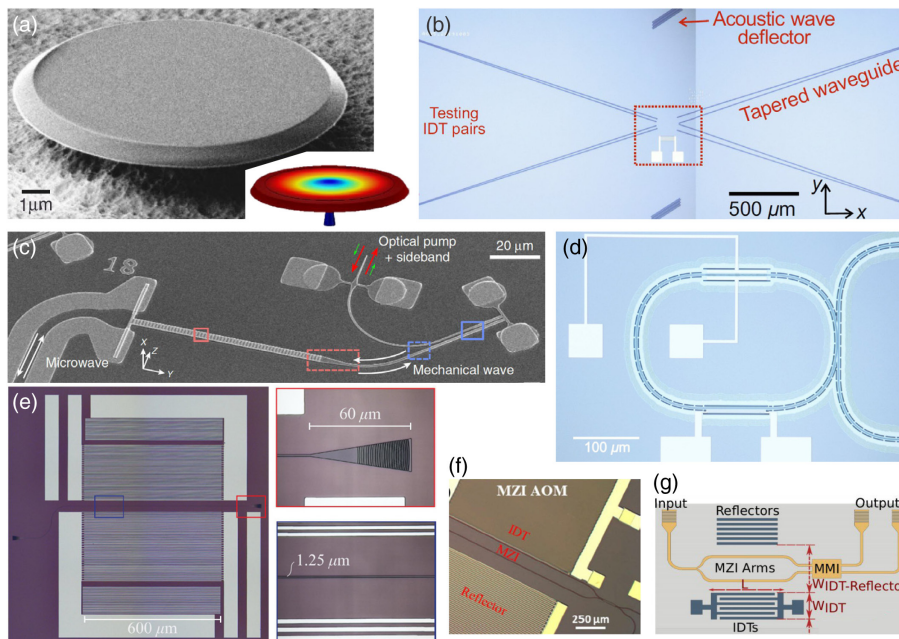
LN optomechanical devices. (a) Suspended optomechanical disk cavity (inset: simulated mechanical mode). (b) Acousto-optic frequency shifter on LNOI. (c) Suspended piezo-optomechanical cavity. (d) Acousto-optic modulator on LNOI. (e) Acousto-optic waveguide, as well as IDT and grating coupler, on LN on sapphire. (f), (g) Hybrid LN acousto-optic modulators. (a) Reprinted by permission from Macmillan Publishers Ltd.: Jiang and Lin, Sci. Rep. **6**, 36920 (2016) [164]; licensed under a Creative Commons CC-BY license. Copyright 2016. (b) Reprinted with permission from [393]. Copyright 2020 Optical Society of America. (c) Reprinted by permission from Macmillan Publishers Ltd.: Jiang *et al.*, Nat. Commun. **11**, 1166 (2020) [177]; licensed under a Creative Commons CC-BY license. Copyright 2020. (d) Reprinted with permission from [165]. Copyright 2019 Optical Society of America. (e) Reprinted with permission from Sarabalis *et al.*, APL Photon. **5**, 086104 (2020) [397]. Copyright 2020 AIP Publishing LLC. (f) Reprinted with permission from [394]. Copyright 2019 Chinese Laser Press. (g) © 2019 IEEE. Reprinted, with permission, from Khan *et al.*, J. Lightwave Technol. **38**, 2053–2059 (2020) [385].

and a high photoelastic coefficient p_{14}. It also features a higher acoustic velocity than the Rayleigh-like modes, and thus increases the acoustic frequency of the devices.

However, sapphire is a hard material and challenging for fabrication. Currently, the major limitation is the availability of high-quality LN-on-sapphire wafers. Bubbles formed between the thin-film LN and sapphire substrate during the bonding process significantly impact the usable area of LN-on-sapphire wafer, to less than 50%. However, we believe that these difficulties will be overcome in the near future as more demand for high-quality LN-on-sapphire wafers will drive the technological advancements. Molecular beam epitaxy growth of LN on sapphire has been demonstrated [399], and it opens another pathway for high-quality LN on sapphire, although the current film quality is still not comparable with ones prepared by the Smart-Cut process.

5.2d. Suspended Thin-Film LN

As acoustic waves do not radiate into vacuum, suspended LN thin films are more flexible in design and could achieve higher acoustic frequency and larger Q-factors. Such suspended structures can be fabricated using LNOI, in which the oxide is removed by a wet etch with HF or using HF vapor etching to preserve the mechanical integrity of the structure. Alternatively, LN on Si could be used, where XeF_2 gas would be used to remove Si and release LN devices. XeF_2 gas etching does not etch LN and, being a dry process, does not suffer from surface tension issues that are common in liquid-phase approaches.

Suspended LN disks support both optical whispering gallery modes and mechanical modes [Fig. 35(a)], and have been used to achieve optomechanical coupling [164], but at a relatively low mechanical frequency of hundreds of megahertz. Optomechanical crystals [141,177,180] have also been developed on suspended LN. Periodic structures provide bandgaps for both light and acoustic waves, while resonators are formed by introducing defect modes within the bandgap, for example, by introducing a perturbation to the periodic unit cell. Optomechanical crystals feature small optical and acoustic mode volumes and large overlaps between the two modes. However, piezoelectrically driving such small acoustic modes is challenging. It can be done using electrodes directly deposited on the optomechanical crystals [180] or by employing an IDT on a suspended acoustic waveguide then guided to the crystals [177]. Due to the small size of electrodes, the demonstrated microwave-to-mechanical conversion efficiency is ∼0.1%. Efforts have also been made to guide the acoustic wave from large efficient IDTs to smaller sized waveguides [400].

On the other hand, efficient microwave-to-mechanical conversion has been demonstrated on suspended LN slabs with optical waveguides [165]. The microwave return loss from the acoustic resonator can be less than −10 dB [401]. The optical waveguides do not cause acoustic losses in the suspended structures. Thus, devices can achieve higher acoustic frequencies (in the gigahertz range) and acoustic Q-factors. Also, optical ring resonators defined by etched optical waveguides benefit from higher Q-factors than photonic crystals. However, the optomechanical coupling rate is compromised due to the large mode volumes.

Some of the concerns for suspended thin-film LN are robustness and high RF/optical power handling. About 1 W optical light has been successfully coupled from lensed fibers to suspended optical waveguides, and only about 100 mW RF power has been applied to the suspended LN acoustic cavities. Higher powers could damage the suspended LN structures, probably due to the localized heating.

5.3. Applications of Microwave Acoustic Modes

Various applications of acousto-optic devices have been discussed [402]. Recent developments in LN piezo-optomechanics have resulted in demonstrations of state-of-the-art devices (Fig. 35) for microwave-to-optical conversion, optical frequency shifting, optical gyroscopes [395], and non-reciprocal optical transmission. Here, we highlight a few applications that have attracted the most attention.

5.3a. Microwave-to-Optical Conversion

Compared to LN cavity electro-optic implementations, LN piezo-optomechanical implementations [165,177] demonstrate higher microwave-to-optical conversion efficiencies by taking advantage of higher Q-factors and smaller mode volumes of the mechanical resonances. The state-of-the-art implementation demonstrates a single microwave photon to optical photon conversion efficiency of 5% using piezo-optomechanical crystals [Fig. 35(c)] [177].

Piezo-optomechanical microwave-to-optical convertors are categorized into two groups—one employs a mechanical resonance and an optical resonance, and the other employs an extra microwave electromagnetic resonance to facilitate the microwave to mechanical conversion. Due to their strong piezoelectricity, LN devices demonstrate efficient microwave-to-mechanical conversion even without an electromagnetic resonator. Using IDTs, >80% of the microwave power has been successfully delivered to suspended LN slabs [Fig. 35(d)] [401].

In order to achieve microwave-to-optical conversion with unitary efficiency, there are a few strategies that could be considered. While LN features strong piezoelectricity, the optomechanical coupling rate of LN devices is smaller than that in the state-of-the-art Si devices. This is due to the lower photoelastic coefficients of LN compared to Si, and the limitations in LN fabrication. Hybrid devices that use LN and Si have the potential for higher microwave-to-optical conversion efficiencies, and such hybrid devices using AlN and Si have been recently demonstrated [386], though their efficiency is still limited.

Similar to double-ring cavity electro-optics (Subsections 3.5 and 3.6), employing a second optical resonance can enhance the microwave-to-optical conversion efficiency by the ratio between the microwave frequency and the optical linewidth. Such improvements are significant for high-Q optical cavities with linewidths of tens of megahertz. However, there is still a need to match the mechanical resonant frequency and the differential frequency between the optical resonances, which can be done, for example, by DC electro-optic tuning.

5.3b. Integrated Acousto-Optic Modulation and Frequency Shifting

Commercial bulk AOMs typically operate at acoustic frequencies below 100 MHz, though devices featuring gigahertz frequencies have been available with compromised performance (see Subsection 5.2a). Meanwhile, integrated AOMs have demonstrated even higher acoustic frequencies in the gigahertz regime. Among integrated devices, LN AOFSs [393,398] demonstrate frequency shifting efficiencies that are 10–100 times higher than those of the pioneering integrated AOFS developed on thin-film AlN [Fig. 35(b)]. However, the frequency shifting efficiencies are only a few percent, which is still quite low compared to the mature commercial bulk AOFSs. There are a few challenges for integrated AOFSs. First, the size of acousto-optic interaction regions for the integrated devices is limited to ~100 μm, while this can be a few centimeters in bulk devices. Second, the traveling acoustic waves in integrated devices are typically generated by IDTs, whose small feature sizes limit the RF power at about 1 W, while bulk AOFS can handle 10 W of RF power.

Several efforts are being made to improve the integrated realization of AOMs and AOFSs. One is to employ optical or acoustic resonances. Another is employing the LN-on-sapphire platform [Fig. 35(e)] [397] for better acoustic confinement and better substrate thermal conductivity to handle high RF power.

5.3c. Non-Reciprocal Optical Devices

Since the acoustic velocity is about 5 orders of magnitude smaller than the electromagnetic wave velocity, acoustic waves at microwave frequencies have wave numbers, k, that are 5 orders of magnitude larger than their electromagnetic counterparts. Through acousto-optic interaction, a traveling acoustic wave can thus result in a strong non-reciprocity between light traveling in opposite directions. Non-magnetic acousto-optic isolators or circulators are being developed, which are compatible with magnetic fields and desired for quantum systems. Such acousto-optic non-reciprocal devices have been developed on thin-film AlN [403,404] and LN [405]. However, the achieved efficiency is still much lower than the state-of-the-art magnetic bulk optical isolators and circulators.

6. HETEROGENEOUS INTEGRATION

Significant efforts have been made to achieve heterogeneous integrations of thin-film LN with other materials. On one hand, many mature PIC platforms, such as Si and SiN$_x$, lack $\chi^{(2)}$ nonlinearity and/or the capability of QPM. Integrating thin-film LN through flip-chip or wafer bonding can complement their functionality while leveraging their existing fabrication/manufacturing processes. On the other hand, thin-film LN is a promising platform for quantum information processing, but the material itself does not offer memories, detectors, and deterministic sources. Furthermore, integrated lasers, amplifiers, linear detectors, and driving electronics are desirable in some classical applications, but they are not provided natively by LN. Therefore, many works have been focused on integrating these missing elements on thin-film LN photonic circuits. In this section, we review hybrid modulators, detectors, single-photon emitters, and rare-earth-ion doping, and give some perspectives on III-V integration on thin-film LN.

6.1. Hybrid Modulators

EO modulators based on thin-film LN have been discussed generally in Subsections 3.2 and 3.3, with emphasis on monolithic, dry-etched approaches. Since hybrid EO modulators represent a considerable portion in the literature and have ignited significant interests [39,97], we dedicate this subsection to summarizing the rationale, approach, and current progress in hybrid modulators.

High-performance and scalable EO modulators are critical components for applications ranging from optical communications to quantum signal distribution. Current all-Si optical modulators, based on the plasma dispersion effects and free-carrier absorption, are pursued mainly due to the excellent scalability and low cost offered by their CMOS-compatible fabrication processes [406]. However, compared to EO modulators, their performance is largely limited in terms of bandwidth, extinction ratio, insertion loss, temperature stability, and working spectrum.

Hybrid LN/Si modulators can combine the scalability of silicon photonics with the excellent EO performance of LN. This approach relies on bonding of bare LN thin films on pre-patterned Si photonic circuits. It was first implemented in hybrid ring modulators [111–113] by bonding pieces of LN thin films prepared from ion slicing onto Si ring resonators. Later, LN/SOI hybrid traveling-wave modulators with 3 dB EO bandwidth exceeding 100 GHz were demonstrated [23]. The key design

point is to transition from the Si waveguide mode to the Si/LN supermode, and maximize confinement inside LN for the modulation region [see Fig. 36(a)]. Bonding of dry-etched thin-film LN modulators on Si photonic circuits was also achieved, where the splitters/combiners and grating couplers of the MZM were all Si, but the phase modulation sections, including the LN ridge waveguides and metal electrodes, were in LN thin films [22]. In this approach, full mode transition from a Si waveguide to a thin-film LN waveguide is possible [see Fig. 36(b)], which offers stronger field confinement in the LN compared to the bare-film-bonding approach. More recently, hybrid LN (unpatterned)/SiN_x MZMs have also been demonstrated, which are CMOS-compatible and aimed for future integration with Si photonics [200]. Theoretical studies of CMOS-compatible hybrid modulators were also carried out [225]. We expect such hybrid integration to soon flourish and make LN a popular component in larger integrated systems.

Another class of hybrid modulator uses LNOI as the base substrate, and adopts rib loading to form waveguides to avoid LN etching (see Subsection 2.3c). This approach has been successfully implemented using SiN_x, Ta_2O_5, chalcogenide glasses, and Si (as summarized in Table 3 and Table 4). Though rib-loaded modulators have not been able to fully utilize CMOS-fabrication facilities, they do reduce some process compatibility issues associated with LN etching, and can reach similar performance to monolithic ones [407]. Beyond standard EO modulators used for telecommunication, an integrated EO Fourier transform spectrometer has also been demonstrated based on SiN_x-loaded thin-film LN modulators [408].

6.2. Detectors

On-chip photon detection is crucial for scalable photonic information processing. Waveguide-integrated detectors are highly desirable—they eliminate the loss from fiber-to-chip couplings and are compact for large array integration [409]. For quantum applications, integrating single-photon detectors directly on LN waveguides

Figure 36
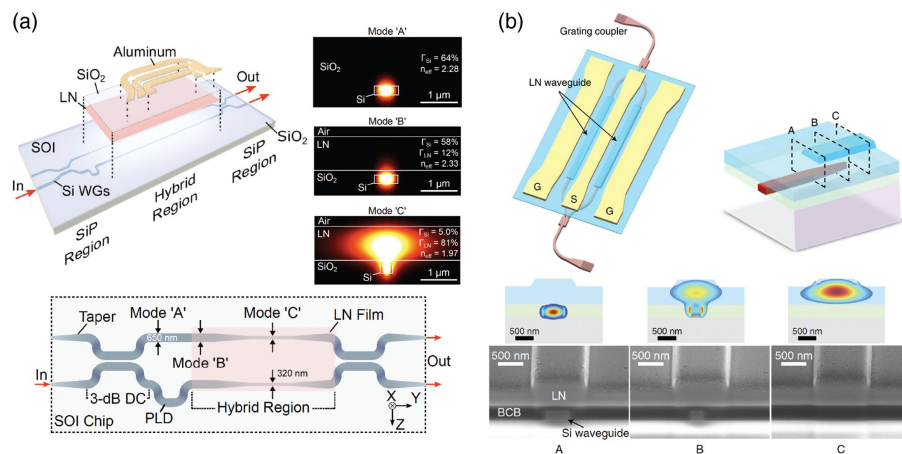
Hybrid LN/SOI modulators. (a) Bare LN thin film bonded on pre-patterned SOI waveguides [23]. In the hybrid region, the Si waveguide is designed to have large confinement in LN. (b) Dry-etched thin-film LN modulator bonded on SOI waveguides [22]. In this approach, the optical mode can transition completely from the Si waveguide to the LN waveguide. (a) Reprinted with permission from [23]. Copyright 2018 Optical Society of America. (b) Reprinted with permission from He *et al.*, Nat. Photonics **13**, 359–364 (2019) [22]. Copyright the Author(s), under exclusive license to Springer Nature Limited 2019.

would allow single-photon generation (through SPDC or integrated solid-state emitters), manipulation (through EO modulations/switching), and detection all on the same chip, promising a fully integrated quantum photonic processor.

Superconducting nanowire single-photon detectors (SNSPDs) and transition-edge sensors (TESs) are two leading single-photon detection technologies, especially at infrared wavelengths [410–413]. They are suitable for heterogeneous integration with photonic waveguides as they only require a single layer of material. On bulk LN substrates, SNSPDs based on polycrystalline NbN have been studied since 2012 [414,415]. On Ti-indiffused LN waveguides, integrated SNSPDs based on amorphous WSi as well as W TESs have both been demonstrated [416,417].

Very recently, direct integration of SNSPDs on thin-film LN waveguides has been successfully demonstrated [418,420] by overcoming a number of fabrication challenges. Figure 37(a) shows a scanning electron micrograph of a hairpin NbN SNSPD integrated on a LNOI waveguide. Conventionally, SNSPDs are patterned before waveguide fabrication, because the superconducting nanowires are highly sensitive to constrictions as well as inhomogeneities and are better done on a clean, flat substrate. However, thin-film LN waveguide fabrication involves aggressive dry etching and wet cleaning, which will damage the superconducting nanowires. It is, therefore, more suitable to pattern the SNSPD after waveguide fabrication, which makes the lithography step for SNSPDs particularly challenging. Furthermore, both demonstrations employed specially tailored deposition processes for the superconducting thin film to avoid excessive heating, which is incompatible with LN thin films [421,422]. From our own experience, on bulk LN, the pyroelectric effect tends to cause electrostatic discharge and damage the nanowires under rapid temperature change. However, this effect does not seem to be critical with LNOI waveguides. Besides fabrication yield, a noticeable problem is that the partially etched LN waveguide makes the absorption rate of the TE mode small ($\sim 0.1\,\text{dB/}\mu\text{m}$), which requires the nanowire length to be hundreds of micrometers long to reach near-unity on-chip efficiency. Future incorporation of photonic crystal mirrors/cavities [423,424] or microrings [425] may be used to enhance the absorption. Besides direct lithographical integration, another viable alternative is to use flip-chip transfer [426], which circumvents the challenging fabrication and improves the yield.

Figure 37
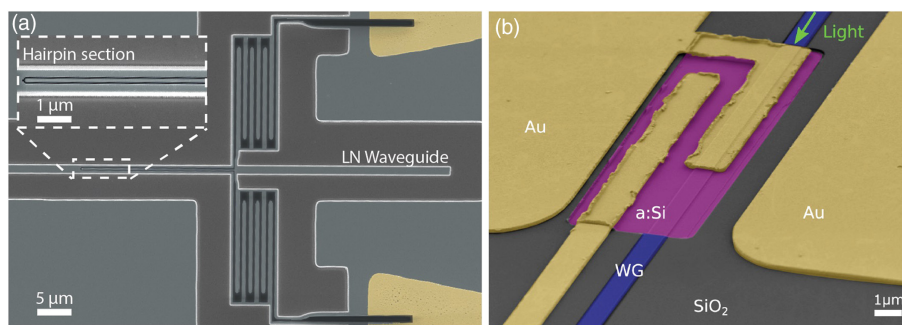
Heterogeneously integrated photodetectors on LNOI waveguides. (a) NbN superconducting nanowire single-photon detector on monolithically etched LNOI waveguide (inset shows the harpin nanowire on waveguide) [418]. (b) Amorphous Si photodetector on LNOI waveguide [419]. (a) Reprinted with permission from [418]. Copyright 2020 Optical Society of America. (b) Reprinted with permission from Desiatov and Lončar, Appl. Phys. Lett. 115, 121108 (2019) [419]. Copyright 2019 AIP Publishing LLC.

Besides single-photon detectors, the integration of classical detectors is equally important and is particularly useful for applications such as microwave photonics and large-scale neural networks [427]. On Ti-indiffused LN waveguides, GaAs detectors have been demonstrated [428]. On the thin-film platform, metal-semiconductor-metal photodetectors based on amorphous Si have been reported, featuring responsivity of 22 mA/W to 37 mA/W in the 635 nm to 850 nm wavelength range [419] [see Fig. 37(b)]. Note that the integrated SNSPDs [418,420] and amorphous Si detectors [419] discussed here can be fabricated by direct material deposition and patterning on LNOI waveguides. However, conventional semiconductor detectors, such as Si or III-V $p-n/p-i-n$ or avalanche photodiodes, will likely require flip-chip bonding. As an example, we will discuss III-V integration in Subsection 6.5.

6.3. Single-Photon Emitters

Similar to integrated single-photon detectors, on-chip single-photon sources are another critical component for photonic quantum information processing. While heralded single-photon sources can be produced through SPDC processes, their probabilistic nature poses significant challenges for scaling up.

Solid-state quantum emitters and quantum dots in 2D materials are excellent sources of on-demand single photons due to their small spatial footprint and good emission properties. Recently, several works have demonstrated the coupling of quantum-dot emitters to integrated on-chip Si-based photonic platforms [429–431]. The main drawback of Si is the lack of an effective and simple mechanism for cryogenically compatible EO modulation (both phase and amplitude). In 2018, direct integration of efficient single-photons sources in the telecom band with the LN photonic platform was demonstrated [432] with moderate coupling efficiency of 40.1%. Indium arsenide (InAs) quantum dots embedded in an InP nanobeam were transferred to a LN photonic circuit by the pick-and-place technique using a focused ion beam (Fig. 38) [429]. Future integration of various on-chip passive and active components in the LNOI platform, e.g., phase and amplitude modulators, beam splitters, and filters, will enable the demonstration of a reconfigurable integrated source of single photons on demand. Another promising platform to explore the deterministic generation of single photons includes quantum dots and color centers in 2D materials. Recently, 2D tungsten disulfide (WSe_2) flake was placed [433] on a facet of Ti-indiffused MZI in bulk LN for coupling of single photons to integrated photonic structures. This approach could be extended to the thin-film platform. These studies pave the way for the realization of on-chip, integrated, and multi-qubit quantum photonic circuits.

6.4. Rare-Earth Ions

Rare-earth-ion-doped (REI-doped) crystals have been used for several optical applications, going back decades. These include lasers, amplifiers, scintillators, sensors, and classical and quantum signal processing [434,435]. To exploit their properties within LN-based applications, REI-doped LN in bulk and waveguide geometries has been developed and utilized over several years [436]. However, it was only this past year that REIs, namely Tm^{3+}, Er^{3+}, and Yb^{3+}, were investigated in thin-film LN [133,437]. This is partially due to the fact that bonded LNOI has only recently became commercially available and that previous studies of REIs in modified crystals—ranging from polycrystalline to surface-doped bulk samples—revealed some non-ideal properties from those in crystals grown from the melt (e.g., using a Czochralski process) [438], in particular for the case of REI-doped LN [439]. We now summarize the results of Refs. [133,437], which were investigated mainly for quantum science applications. Note that similar studies have also been performed in Ref. [440].

In the work of Ref. [437], a Smart-Cut process was used to bond a 1% Tm-doped film of X-cut LN to SiO_2 on LN [see Fig. 39(a)]. The relatively low doping concentration is suitable for quantum processing, which often requires the suppression of REI–REI interactions to reduce decoherence. Partially etched grating couplers and single-mode waveguides at 794 nm were created and cladded in LN, while the wavelength and polarization of the optical mode were optimized for interaction with the $^3H_6 \rightarrow {}^3H_4$ optical transition of Tm^{3+}. Waveguides were also fabricated with orthogonal polarization for comparison.

The sample was cooled to 3.6 K along with a bulk crystal for comparison. Broadband absorption spectra were measured that were consistent with a reference bulk crystal.

Figure 38
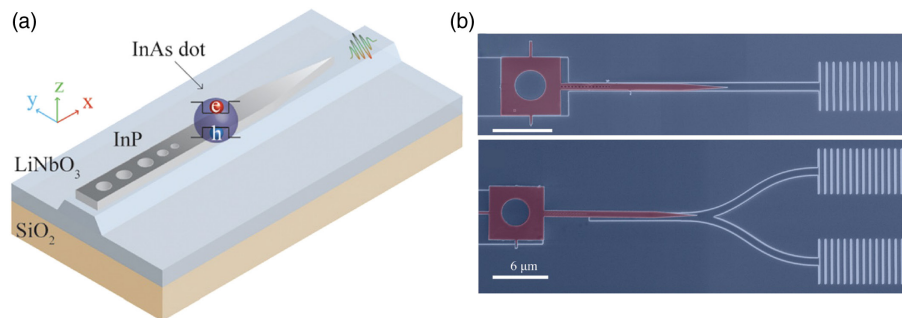
Integrated single-photon emitters on LN waveguides. (a) Schematic of InAs quantum dot embedded in an InP nanobeam sitting on top of a LNOI waveguide. (b) Scanning electron micrographs of the fabricated device, where the nanobeam with emitter is pick-and-placed on a grating-coupled waveguide (top) and beam splitter (bottom) for photon correlation measurement. Reprinted with permission from Aghaeimeidodi *et al.*, Appl. Phys. Lett. **113**, 221102 (2018) [432]. Copyright 2018 AIP Publishing LLC.

Figure 39
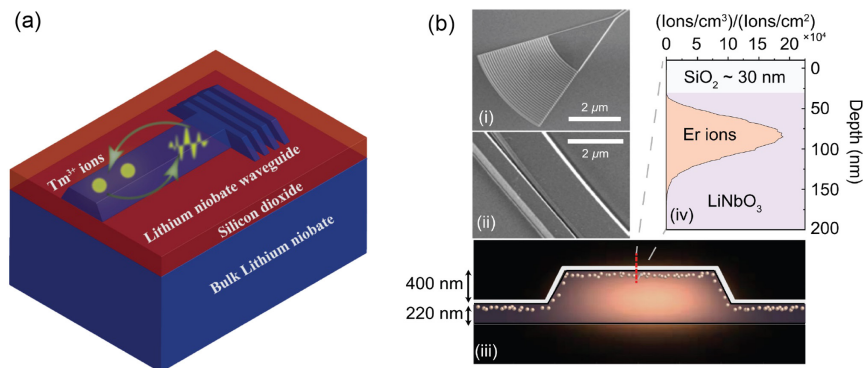
Rare-earth ions in LNOI integrated photonics. (a) Illustration of rare-earth ions (Tm^{3+} indicated) in etched thin-film LN on SiO2/LN. (b) SEM images of (i) grating coupler and (ii) bus-resonator coupling section on thin-film LN. (iii) Schematic cross section of a thin-film LN waveguide (transverse-electric mode) implanted with rare-earth ions. (iv) SRIM simulation of the implantation depth of Er^{3+} in SiO_2-coated LN under a 350 kV acceleration voltage and a flux of 1.14×10^{14} ions/cm^2. (a) Reprinted with permission from Dutta *et al.*, Nano Lett. **20**, 741–747 (2020) [437]. Copyright 2019 American Chemical Society. (b) Reprinted with permission from Wang *et al.*, Appl. Phys. Lett. **116**, 151103 (2020) [133]. Copyright 2020 AIP Publishing LLC.

Importantly, the polarization dependence of the transition dipole moment was also consistent despite variations in light polarization owing to their racetrack waveguide design, indicating that the Smart-Cut process did not add residual strain compared to the bulk crystal. A luminescence spectrum was also measured using the thin film and bulk crystal, showing comparable transition linewidths (0.7 nm) between these samples and the absence of background fluorescence from the thin film. This indicates that the Smart-Cut process does not create any additional fluorescent centers that absorb at the 773.4 nm excitation wavelength used here. Time-resolved luminescence further revealed consistent fluorescence lifetimes of 157 μs in both the thin film and bulk samples, suggesting that no additional non-radiative decay pathways were induced by the Smart Cut. Time-resolved spectral hole burning revealed hole widths and depths that were comparable to that of bulk Tm:LN measured under similar conditions, accounting for power broadening and spectral diffusion, and with two orders of magnitude lower laser power than Ti-indiffused waveguides owing to the small (0.07 μm^2) transverse area of the optical mode.

Despite these results, the uniformly doped wafer may not be ideal for low-loss integration at 794 nm. To potentially overcome this, and to operate in the desirable telecom C-band, Er^{3+} ions were implanted into etched off-the-shelf Z-cut LNOI. A similar spectroscopic study of the 1532 nm $^4I_{15/2} \to {}^4I_{13/2}$ transition of Er^{3+} was performed in Ref. [133]. Here, grating couplers as well as microring and centimeter-long waveguides were created and optimized to guide single-mode TE-polarized light at 1532 nm, which interact strongly with the Er^{3+} transition. See Fig. 39(b).

A thin cladding layer was deposited on the chip before the implantation of Er^{3+} ions (energy of 350 keV, fluence of 1.14×10^{14} ions/cm^2) likely to reduce channeling, with SRIM simulations indicating 50 nm penetration depth into the LN film. Post-implantation annealing was carried out for 5 h at 350°C to overcome implantation damage and recover transmission. Specifically, loaded Qs of 200,000 were measured at 1532 nm, owing to the absorption of Er, with loaded Qs of up to 1 million off resonant from the Er^{3+} transition at 1515 nm (average Q of 500,000).

The sample was cooled to 2.8 K, and resonance fluorescence was performed, revealing a fluorescence linewidth of 170 GHz, comparable to the literature value of 180 GHz, with the difference owing to imperfect wavelength calibration. The sample was further cooled to 1.7 K, and time-resolved excitation revealed a fluorescence lifetime of 3.2 ms, which is somewhat larger than the 2.0 ms population lifetime of the $^4I_{13/2}$ level measured in a bulk sample by spectral hole burning, with the difference to be investigated in future work. Supporting cavity-ion coupling, they also measure a reduction in fluorescence lifetime of 0.6 ms (corresponding to a Purcell enhancement of 3) of ions in the ring compared to the waveguide, consistent with the measured Qs, optical mode volumes, and field overlap with implanted ions.

Overall, these studies predominantly address the low-temperature spectra and fluorescence properties of REIs and are a step towards future REI-based quantum applications in thin-film LN. We note, however, that the bonding process used to realize thin-film LN may cause variations in the crystal properties, in particular near surfaces, in ways that are not revealed by the previous studies, and more measurements (e.g., coherence, sub-level properties, spectral diffusion) are needed.

On the classical end, very recently, on-chip waveguide amplifiers [441,442] and microdisk lasers [443–445] were demonstrated using Er^{3+}-doped thin-film LN. In these works, Er^{3+}-doped LN thin films were ion-sliced from uniformly doped bulk crystals. In Ref. [441], a 3.6-cm-long spiral LNOI waveguide was fabricated using the photolithography assisted chemo-mechanical etching technique (see

Subsection 2.3b), and a maximum net gain of 18 dB was observed in the small-signal-gain regime around 1530 nm. In Ref. [442], a dry-etched ridge waveguide was used, showing a 5 dB net gain with 5 mm length. In Refs. [443–445], high-Q microdisks were used as cavities, and lasing at telecom wavelengths was observed. A strong photorefractive effect was observed in these microdisk lasers, especially in the presence of a short-wavelength pump. This effect led to a pump-power-dependent emission wavelength [443] and reduced the pump efficiency [444]. Mitigation of the photorefractive effect, e.g., by co-doping MgO, is needed in future developments. These preliminary demonstrations show the potential of using REI doping to achieve gain and lasing on the LNOI platform.

6.5. III-V Materials

Integrated active photonic components, including lasers, amplifiers, and photodetectors, have been developed extensively in III-V materials with state-of-the-art performance. The integration of LN electro-optics and III-V components could open opportunities for optical communications, microwave photonics, and light detection and ranging (LIDAR). Such opportunities have been foreseen by several ongoing research programs supported by government funding agencies worldwide.

The integration of III-V with LN components could benefit from previous experiences in integration with other materials, such as LN on Si [446], as well as III-V on silicon-on-insulator (SOI) [447–449] and Si_3N_4 waveguides [450]. As LN is inert to most chemicals used in III-V fabrication, the III-V stack layers can be transferred to LN and then fabricated without damaging the LN waveguides. This approach could enable fabricating photodetectors directly on the LN waveguides. Alternatively, it is possible to transfer LN thin films to the III-V substrates, and then fabricate the LN devices. The transfer process could be similar to transferring LN thin films on SOI substrates [446]. For integration using overlaying materials, optical tapers are usually used to couple the light between these materials [446–450].

On the other hand, pick-and-place tools could enable direct placement of fabricated III-V components on the LN chips. This approach has been used to transfer III-V lasers on silicon photonic circuits [451]. In addition to the optical tapers, efficient butt-/end-fire coupling between III-V lasers and LN waveguides can be achieved by proper mode-size matching and accurate facet alignment. This approach could be more suitable for integrating high-power III-V lasers or optical amplifiers, as the III-V components can sit directly on the substrates (e.g., Si) with high thermal conductivity.

7. CHALLENGES AND OPPORTUNITIES

The field of integrated photonics on thin-film LN is advancing rapidly, promising many exciting opportunities in telecommunication, data communication, microwave photonics, and quantum photonics. To enable these, however, several important challenges need to be addressed. In this section, we discuss these challenges and outline several exciting near- and long-term opportunities.

7.1. Charge Carrier Effects

Mobile charge carriers in electro-optic materials can create a wide variety of optical and electro-optical effects, including photoconductivity [452], photorefractivity [453], and dielectric relaxation [454]. These are long-standing problems with LN material, and often limit the stability and power handling capability of LN devices. Recent measurements [181,339,455,456] suggest that these effects are stronger in LNOI than in comparable bulk devices, possibly due to the tighter optical confinement and higher crystal defect concentration in LNOI. These charge carrier effects

typically manifest as bias or detuning drift when operating electro-optic devices in LNOI, with timescales typically on the order of milliseconds to hours or longer [455]. While such drifts are an important practical challenge for the realization of highly stable LNOI devices, charge carrier effects may also be useful for *in situ* device tuning [457] or to create strong all-optical nonlinearities [181].

Photorefractive materials experience refractive index changes when exposed to optical power due to the excitation of charge carriers from crystal defect sites. Figure 40 schematically depicts this mechanism inside a LN ridge waveguide. More details on the photorefractive effect can be found elsewhere, for example, in Refs. [458,459].

The photorefractive effect provides both opportunities and challenges for the LNOI platform. Recent work has shown that the photorefractive effect in LNOI is stronger and responds at faster timescales than in bulk devices, especially in high-quality factor resonant photonic devices [455,456]. Indeed, resonance tuning of photonic crystal cavities in LNOI has been demonstrated using optical powers corresponding to just a few photons inside the cavity [181]. Photorefractive effects are particularly prominent in LNOI devices operating at visible wavelengths [15]. Such strong power-dependent detuning can make it more challenging to operate LNOI devices at high powers or when stable phase tuning is required [167,175,176]. Efforts to reduce photorefractive effects in LNOI have shown that photorefractive shifts can be reduced by annealing and using uncladded waveguides [339], but further work is required to understand the impact of material properties and device geometry on photorefraction in LNOI devices. Other methods of mitigation used in bulk LN devices include transition metal doping [460] and operating at elevated temperatures [461].

Dielectric relaxation is a process by which charge carriers in a dielectric material can migrate to shield an applied electric field. For the simple case of a uniform material with dielectric constant ϵ and resistivity ρ, this relaxation occurs at a rate given by the dielectric relaxation time $\tau_r = \epsilon\rho$. It is well known that such relaxation leads to drifts in the bias voltage required for electro-optic devices [454,462–464]. To our knowledge, these effects have yet to be studied directly in LNOI devices, but recent works have observed bias drift consistent with dielectric relaxation [465]. Thermo-optic tuning can be used as a drift-free method of bias control [16,466], but this requires tradeoffs in power dissipation and tuning bandwidth. We believe that understanding and mitigating dielectric relaxation in LNOI is a key challenge for creating stable electro-optic devices and networks in this platform.

7.2. Quantum Photonics

Optical photons have many properties of interest for the realization of quantum technologies: they exist under ambient conditions, are generally impervious to

Figure 40
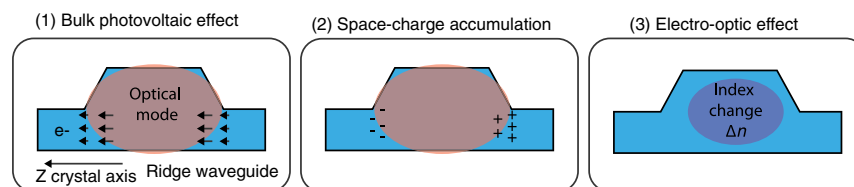
Schematic depiction of the mechanism of photorefraction in LNOI ridge waveguides. (1) Optical power excites charge carriers, which move preferentially along the Z crystal axis due to the bulk photovoltaic effect in LN; (2) excited charge carriers migrate and reach a steady-state spatial distribution; and (3) the resulting space-charge field perturbs the refractive index via the EO effect.

environmental noise, can travel long distances, and can be generated, manipulated, and detected relatively easily. While many important demonstrations have been realized using discrete optical components, including a recent demonstration of photonic quantum computational advantages [467], future quantum applications will require the integration of a large number of different functionalities on the same photonic platform [468]. Such integrated quantum photonics platforms will need to (i) be ultra-low loss in order to preserve fragile quantum states; (ii) enable precise control of the temporal and spectral profiles of photons; (iii) allow fast and low-loss optical switches to route quantum information; (iv) be able to operate in the visible wavelength range, where many single-photon sources and quantum memories operate, as well as the telecom wavelength range, where low-loss optical fibers exist; (v) feature strong nonlinearities for efficient frequency up- and down-conversion to bridge these wavelength ranges, as well as enable efficient quantum transduction and entangled photon-pair generation; and (vi) allow the integration of photodetectors and operating electronics. The thin-film LN photonic platform could simultaneously meet nearly all of these requirements and thus is an excellent candidate for integrated quantum photonics.

Among the most popular and arguably most advanced schemes for on-chip processing of single-photon quantum states are path-encoded schemes. In this approach, optical quantum information is encoded in the position (waveguide) in which a photon is present [468]. Quantum operations can be performed using low-loss optical waveguides, beam splitters, and phase shifters. With the growing complexity of optical circuits [469], additional challenges related to fabrication variation arise, which motivates active tuning of photonic devices [470]. As an example, beam splitters can be achieved by MZIs, which can be tuned to the desired operation point. This increases the number of active devices and optical phase shifters, but allows for compensating for defects and fabrication imperfections [471]. Among path-encoded quantum photonic realizations, the use of thermal phase shifters is very popular, as they can be implemented in many material platforms such as Si and SiN$_x$ and are very compact in size. However, thermal heaters draw electrical current, and with an increasing number of thermal phase shifters, the total power consumption also increases. Additionally, with denser packing of devices, thermal crosstalk and cooling becomes another issue that needs to be considered. Finally, thermal tuning is slow, which limits the clock rate of the circuit.

The low propagating loss achieved in thin-film LN is well suited for quantum optic applications, and the electro-optic effect allows low-loss phase shifters, which could drastically reduce the power consumption compared to the use of thermal phase shifters. Beyond this, the ability to perform fast modulation of light makes thin-film LN a promising platform for time- and frequency-encoded quantum operations. Energy-time entangled quantum states carry quantum information in temporal and spectral modes. The ability to process quantum information in the time domain has been widely used for quantum communication, where the temporal modes can propagate long distances in optical fibers [474], and frequency-domain quantum processing enables parallel and multiplexed operations [256,475,476]. Time-domain quantum processing employs fast switches, optical delay lines, as well as unbalanced interferometers as fundamental building blocks [477], while frequency-domain processing requires spectral filtering as well as frequency shifting achieved by, e.g., electro-optic modulation [478]. Thin-film LN could be suited for realizing these schemes [473].

Figure 41 shows some basic resources and elements for photonic quantum processing that are suited for the thin-film LN platform. For example, arrays of integrated PPLN SPDC sources can be multiplexed in time with the help of photon detection

in combination with fast EO switches [472,479] [Fig. 41(a)]. Similarly, these probabilistic sources can also be multiplexed in the frequency domain (a broadband source sliced into multiple frequency bins) using EO frequency shifters to produce a quasi-deterministic single-photon source [480] [see Fig. 41(b)]. Tunable EO-based frequency shifters as described in Subsection 3.5 can be conveniently used to realize gates for frequency-encoded qubits [Fig. 41(c)]. These can serve as the basis for frequency-domain quantum computing [473] [Fig. 41(d)].

7.3. Nonlinear Photonics

The thin-film LN platform provides exciting new directions for the realization of advanced schemes for nonlinear photonics. These include novel frequency comb generation, the deterministic generation of chimera states and band solitons in addition to Kerr and Pockels solitons, the study of co- and counter-propagating mode coupling, and high-dimensional topological effects. These directions exploit the large strong $\chi^{(2)}$ and $\chi^{(3)}$ optical nonlinearities and the phase modulation capability of LN.

Solitons can be utilized within a microresonator to produce broad and coherent frequency comb spectra. Because it has both $\chi^{(2)}$ and $\chi^{(3)}$ optical nonlinearities, thin-film LN is a promising platform for both Kerr (produced via $\chi^{(3)}$) [336] and Pockels (produced via $\chi^{(2)}$) [481] soliton generation. Furthermore, the strong EO effect in LN shows promise for the experimental demonstration of other stable and more

Figure 41
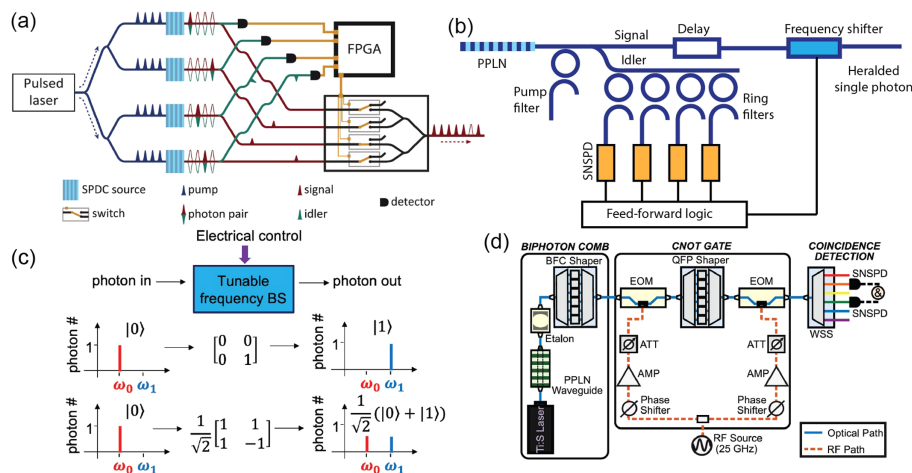
Resources and elements for photonic quantum processing that are well-suited for thin-film LN integrated photonics. (a) Time-multiplexed single-photon sources based on SPDC and fast-optical switches [472]. (b) Frequency-multiplexed single-photon sources. (c) Encoding qubit in the frequency domain and single-qubit gate based on tunable frequency shifters. (d) General purpose quantum frequency processor (QFP) can be implemented using EO modulators and wave shapers [473]. A tunable frequency beam splitter (BS) can greatly simplify the scheme and reduce the required resources. All of these essential components and their subunits, such as PPLN SPDC sources, fast switches, frequency shifters, single-photon detectors, filters, and wave shapers, can be implemented on the thin-film LN platform. (a) Reprinted with permission from Slussarenko and Pryde, Appl. Phys. Rev. **6**, 041303 (2019) [472]. Copyright the Author(s) 2019; licensed under a Creative Commons Attribution (CC BY) license. (d) Reprinted with permission from Lu *et al.*, npj Quantum Inf. **5**, 24 (2019) [473]. Copyright the Author(s) 2019; licensed under a Creative Commons Attribution 4.0 International License.

exotic resonator states, including chimera-like states with purely local coupling [482], corresponding to a chaotic state circulating in the resonator with no expansion or contraction, and band solitons [483], dispersionless and coherent structures occurring in the modulation instability regions under high modulation strength and anomalous dispersion.

However, the role of strong Raman gain observed in LN needs to be understood and engineered since it may play an important role in the overall nonlinear dynamics of the resonator. The combined effects of Raman scattering, four-wave mixing, and EO modulation can result in a broad spectrum of small EO combs around lines formed by Raman and Kerr effects [484]. Such a broad, stable frequency comb with low repetition rates could be used for applications such as optical frequency synthesizers and high-resolution comb spectroscopy. Additionally, the strong Raman oscillation in LN manifests in the counterpropagating direction with respect to the pump field [172], effectively coupling the clockwise and counterclockwise modes in the resonator. The role of Raman and the dynamics of counterpropagating EO fields remains largely unstudied, and the thin-film LN platform presents a promising avenue for exploring more complex nonlinear dynamics.

7.4. Magnetic-Free Non-Reciprocity and Optical Isolation

Lorentz reciprocity is a fundamental principle in electromagnetics. It holds true in linear, time-invariant media with symmetric permittivity and permeability tensors. However, non-reciprocal devices, such as isolators and circulators, are critical for signal routing and blocking, as well as laser protection. The conventional method to realize non-reciprocity is to use magnetized materials, whose permittivity is non-symmetric. In integrated photonics, heterogeneous integration of magneto-optical materials has been pursued. However, it is generally difficult to fabricate, incompatible with large-scale integration, and associated with high insertion loss. In LN, there are multiple approaches to achieve magnetic-free non-reciprocity and on-chip optical isolation.

First, reciprocity can be broken through optical nonlinearity, such as wavelength conversion [485]. LNOI PPLN waveguides are well suited for this approach. The key principle is based on the fact that wave-mixing processes are highly directional due to the stringent phase-matching requirements. Recently, such an optical isolator was achieved based on DFG in PPLN waveguides [see Fig. 42(a)] [486]. In this work, in the presence of an optical pump, signal light propagating in the same direction as the pump will undergo efficient DFG and pass a set of properly arranged frequency filters. Back propagating waves, however, will not experience efficient DFG and will be blocked by the filters. As the fabrication precision, quality, and yield of LNOI PPLN waveguides continue to improve, we expect the conversion efficiency and insertion loss to reach a level that satisfies the requirement of practical applications. Future work may include integrating filters directly on chip, or involving different polarization modes to facilitate on-chip filtering.

The second way to break reciprocity is to break time-reversal symmetry through EO modulation [488]. In fact, a simple traveling-wave modulator is naturally non-reciprocal—it only modulates efficiently in one direction. This can be utilized to implement optical isolators. For example, in a traveling-wave phase modulator, a proper driving voltage can be chosen so that when the light and microwave are co-propagating, the optical carrier frequency will be completely converted into sidebands and then filtered, while the reverse would not be modulated at all.

Another elegant approach for implementing optical isolation through EO modulation is to introduce an interband photonic transition. The two photonic bands can be

even/odd and TE/TM modes in a single waveguide, or symmetric/asymmetric modes in coupled waveguides [489–491]. In the case of an indirect interband transition, as illustrated in Fig. 42(b) [487], an input photon will be frequency up-/down-converted only in one direction due to momentum/phase mismatch. It is worth mentioning that when photons gain/lose energies from microwave fields, they also gain/lose the phase of the microwave field. Using this property, it is possible to construct an effective magnetic field using a pair of such modulators driven by microwave fields with different phases [283], which could also lead to optical isolation.

Similar to the case of EO modulation, acousto-optic modulation is also able to break time-reversal symmetry and achieve non-reciprocity by using phonons to scatter the input photons (as discussed in Subsection 5.3c). Photons modulated by acoustic waves will absorb or emit phonons and therefore achieve similar transitions to the EO modulation process. Compared to EO modulation, the advantage of the acousto-optic approach is the large momentum carried by the phonons due to the short wavelength of acoustic waves, which can lead to larger phase mismatch and thus better suppression of undesired transitions. This non-reciprocal process of acousto-optic modulation has been demonstrated in AlN [492] and Si [493], and can be readily adapted to integrated LN systems.

7.5. Microwave Photonics

Microwave photonics utilizes optical components to generate, transmit, and process high-frequency RF signals, achieving tasks that are difficult using conventional electronics. Specifically, upconverting microwave signals to the optical domain allows low-loss signal transport and flexible spectral tailoring over ultra-wide bandwidths. A generic microwave photonics system consists of laser sources, optical modulators, optical signal processors, and photodetectors. Central to a microwave photonic system are high-performance EO components that have large bandwidth, good linearity, and negligible insertion losses, and can handle large optical power. Traditional


Figure 42
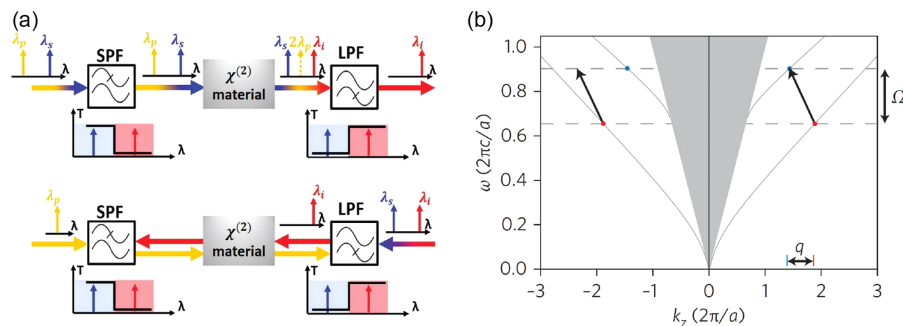
Magnetic-free optical isolation. (a) Optical isolator based on χ^2 wavelength conversion [486]. λ_p, λ_s, and λ_i are pump, signal, and idler wavelengths, respectively. SPF, short-pass filter; LPF, long-pass filter. (b) Non-reciprocal photonic interband transition through time modulation, which can lead to optical isolation [487]. The gray curves represent the dispersions of two modes in a waveguide, and black arrows indicate the photonic transition induced by RF modulation, where Ω is the modulation frequency and a is a unit length (taken as 1 μm here) used to normalize relevant physical parameters (e.g., frequency and wavevectors). (a) Reprinted with permission from [486]. Copyright 2020 Optical Society of America. (b) Reprinted with permission from Yu and Fan, Nat. Photonics 3, 91–94 (2009) [487]. Copyright 2009 Springer Nature.

microwave photonics are based on discrete fiber-optic components that combine bulk LN EO modulators and high-power III-V lasers and detectors. This approach is not scalable due to the large footprint and increased insertion losses when daisy-chaining. In the past decade, significant effort has been devoted to integrated microwave photonics [494,495]. However, existing material platforms, namely SOI, SiN_x, and InP, are facing particular challenges, especially in realizing high-performance EO components. In particular, SiN_x does not allow optical modulation; Si suffers from two-photon absorption and does not offer low-loss and high-bandwidth modulators; and InP enables various active and passive components, but its waveguides have relatively high losses and its modulator has limited linearity.

LNOI is well-suited for microwave photonics. It not only has a large transparency window and ultra-low linear loss, but also offers EO modulators with performance (> 100 GHz, few-volt V_π, < 0.5 dB on-chip insertion loss, and ∼ 100 dB $Hz^{2/3}$ SFDR) that to date few other material platforms can compete with. Furthermore, it allows narrow resonant filters (MHz) with EO and thermal tunability. As discussed earlier, it offers broadband frequency comb sources for multi-band operation, and magnetic-free isolators to facilitate the integration of on-chip lasers. However, the LN platform lacks native light sources, amplifiers, and detectors. To realize a fully integrated microwave photonic transceiver, heterogeneous integration of III-V (e.g., InP and InGaAs) photonic components is a promising direction (see Subsection 6.5). Figure 43 shows a proposed microwave photonic receiver (based on the concept in Ref. [496]) that integrates III-V lasers, amplifiers, and detectors with thin-film LN photonics. In this proposed receiver, beating between two EO frequency combs of different line spacings (referred as signal and reference combs) slices a 50-GHz microwave signal into multiple low-bandwidth channels that can be detected in parallel using a de-multiplexer (DEMUX) followed by an array of photodetectors. A high-bandwidth microwave signal can be decomposed and processed by employing broadband and flat-top EO combs, which can be realized by cascading an intensity modulator with three phase modulators (as described in Subsection 3.4a). With such effort of multi-function/material integration, we expect thin-film LN to play a major role in future integrated microwave photonics.

Figure 43
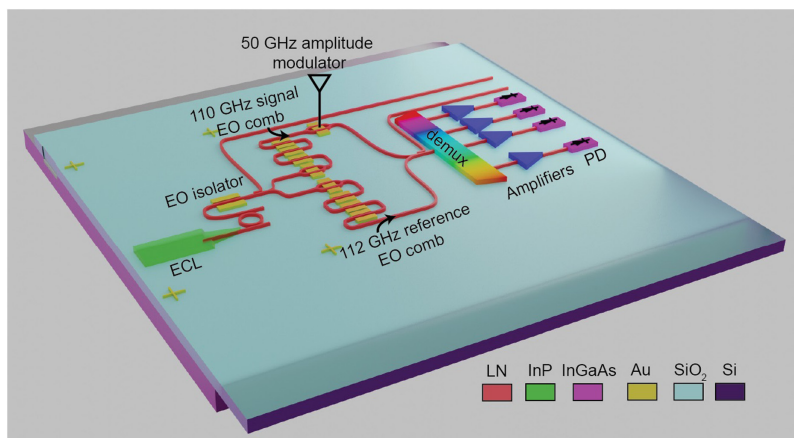
Proposed integrated microwave photonic receiver. It combines LNOI passive (waveguides, high-Q resonators, arrayed waveguides/demux) and EO (modulators, isolators, frequency combs) devices with heterogeneously integrated III-V lasers and high-speed detectors. This figure is adapted from a grant proposal funded under the DARPA LUMOS program. ECL, external cavity laser; PD, photodetector.

7.6. Wafer-Scale Lithium-Niobate Photonic Integration

Among the key advantages of silicon photonics is the compatibility with CMOS fabrication techniques, which enable large-scale and low-cost production of integrated photonic components at high volumes. Consequently, a large variety of foundries are already offering commercial tape-outs of silicon photonic chips with guaranteed performance, which significantly reduces the cost and enables broad access to a very advanced technology platform. Unfortunately, LN is not compatible with current CMOS or silicon photonics processes due to material contamination issues, mainly caused by lithium diffusion or residues from the etching process. Additionally, low-roughness etching of LN, required for low-loss optical waveguides, has only been achieved very recently, and is not yet broadly available. For this reason, almost all thin-film LN devices were achieved using chip-scale proof-of-concept realizations, often relying on electron-beam lithography for pattern definition.

In order to drastically increase the innovation speed, foundry access to wafer-scale LN photonics would be highly desirable. There are different paths to advance thin-film LN from chip-scale demonstrations to wafer-scale processes, mainly focusing on either heterogeneous or monolithic integration. In the approach of heterogeneous integration, LN is bonded to other materials, such as SiN_x [110], to enable wafer-scale processing. Recently it was proposed that LN could be bonded as the final step in standard CMOS silicon photonics processing, where Si waveguides, as well as electrodes, are defined in a scalable process before LN is added. This approach eliminates the risk of contamination and makes LN compatible with standard Si photonics

Figure 44
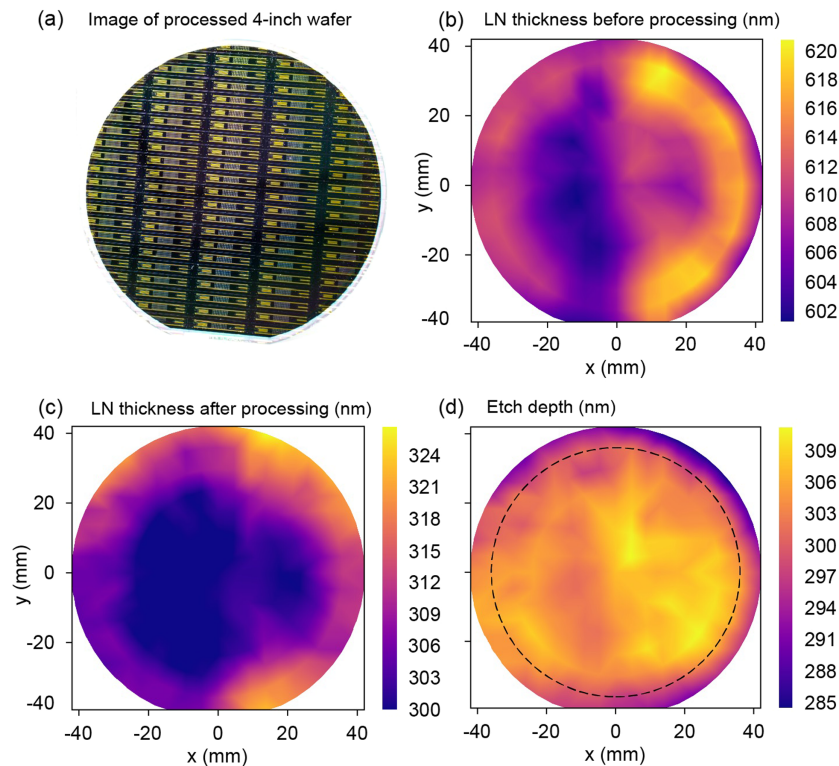
Wafer-scale LNOI fabrication. (a) Image of a processed LNOI wafer including metal electrodes. (b) Thickness of the LN thin film before processing. (c) Film thickness after etching. (d) Etch depth variation across the wafer, showing below 6 nm variation within the dashed circle. Reprinted with permission from [497]. Copyright 2020 Optical Society of America.

foundry processes [225]. In such an approach, it is, however, not possible to pattern or process the LN thin films, which could lead to a reduction in performance.

Alternatively, monolithic wafer-scale processing of thin-film LN has been shown to also be a possibility [497]. While LN is not compatible with CMOS processes, it can be processed at large scales and low cost using existing microelectromechanical systems (MEMS) or even dedicated future lithium-niobate photonics foundries. The advantage of the monolithic approach is reduced process complexity as no bonding to other materials is required and potentially higher performance could be achieved as the LN can be etched and processed directly without process limitations. Wafer-scale processing of 4-inch and 6-inch monolithic thin-film LNOI wafers has recently been demonstrated [497] using scalable deep-UV lithography; see Fig. 44. Wafer-scale LN etching was achieved, resulting in a final film thickness variation of the etched wafer of below 6 nm, limited by both the film thickness uniformity of the initial wafer and the etch. While these thicknesses and etch variations are much larger than currently achievable in silicon photonics, they are already sufficient for large-scale and low-cost manufacturing of high-performance LN photonic chips, and show that scalable wafer processing is possible.

Due to the high potential and performance of thin-film LN, as well as the already demonstrated ability to perform heterogeneous integration as well as monolithic wafer-scale processing, we hope and expect that in the future foundry services will become available, which would significantly accelerate the development of this highly promising photonics platform.

8. CONCLUSION

In this review, we attempted to cover the various aspects of integrated thin-film LN photonics as comprehensively as possible—from the materials and passive optical components to active components based on electro-optics, all-optical nonlinearity, and piezo-optomechanics, as well as heterogeneous integration. We also identified some challenges that need to be overcome to realize the exciting opportunities that lie ahead for this material platform.

Overall, thin-film LN integrated photonics, building on the half-century legacy of discrete components realized in LN crystals, is rapidly revolutionizing a broad range of applications, from its traditional uses in telecommunications and nonlinear optics, to emerging fields such as quantum photonics, cavity electro-optics, and piezo-optomechanics. Within the past few years, thin-film LN modulators have significantly outperformed their widely used bulk counterparts in power consumption, bandwidth, and size, which are key metrics for next-generation optical communication systems. Among many promising new material platforms, such as polymers, plasmonics, or barium titanate, LN is neither the smallest in footprint nor possesses the highest EO efficiency. However, its well-balanced material properties and adequate integrability with decades of industry-proven operation will result in rapid deployment. Such potential in volume applications is key to catalyze LN technology development and could enable scaling-up and cost reduction for the LN thin-film platform at the foundry level. Besides modulators, thin-film LN is breeding a new collection of powerful integrated nonlinear-optical devices. Thin-film nonlinear wavelength converters and downconversion sources have shown orders-of-magnitude higher efficiencies than those using diffusion-based waveguides. In addition, frequency combs, supercontinuum generation, Raman lasing, microwave-optical transduction, and AOMs with impressive metrics have all been demonstrated on this platform. Furthermore, integration with superconducting detectors, quantum-dot single-photon emitters, and rare-earth ions is promising for fully integrated quantum processors. Moreover,

investment and involvement from industry and national facilities are pushing integrated thin-film LN photonics from laboratory proof-of-concept demonstrations to high-yield, wafer-scale productions.

Future optimization in material preparation (e.g., less expensive and higher quality wafers or use of stoichiometric LN), device fabrication (etching, poling, doping, annealing), and system integration (optical and RF packaging) will immediately improve device performance. Studies of photorefraction, charge accumulation, power handling, and loss mechanisms are urgently needed and essential for many applications including achieving extreme optical nonlinearities and operating EO devices at high power, in harsh environments and with long-term stability.

The immediate future of thin-film LN is clear and bright. Its versatility and complexity are fascinating and intriguing. We expect it to soon become a strong contender and indispensable player in the league of integrated photonics—and, more importantly, to make an impact on our daily lives.

DISCLOSURES

MZ,CR: HyperLight Corporation (I,E,P); ML: HyperLight Corporation (F,I,C).

REFERENCES

1. B. Jalali and S. Fathpour, "Silicon photonics," J. Lightwave Technol. **24**, 4600–4615 (2006).

2. M. Smit, K. Williams, and J. van der Tol, "Past, present, and future of InP-based photonic integration," APL Photon. **4**, 050901 (2019).

3. D. J. Moss, R. Morandotti, A. L. Gaeta, and M. Lipson, "New CMOS-compatible platforms based on silicon nitride and Hydex for nonlinear optics," Nat. Photonics **7**, 597–607 (2013).

4. J. Wang, A. Santamato, P. Jiang, D. Bonneau, E. Engin, J. W. Silverstone, M. Lermer, J. Beetz, M. Kamp, S. Höfling, M. G. Tanner, C. M. Natarajan, R. H. Hadfield, S. N. Dorenbos, V. Zwiller, J. L. O'Brien, and M. G. Thompson, "Gallium arsenide (GaAs) quantum photonic waveguide circuits," Opt. Commun. **327**, 49–55 (2014).

5. C. Xiong, W. H. P. Pernice, X. Sun, C. Schuck, K. Y. Fong, and H. X. Tang, "Aluminum nitride as a new material for chip-scale optomechanics and nonlinear optics," New J. Phys. **14**, 095014 (2012).

6. T.-J. Lu, M. Fanto, H. Choi, P. Thomas, J. Steidle, S. Mouradian, W. Kong, D. Zhu, H. Moon, K. Berggren, J. Kim, M. Soltani, S. Preble, and D. Englund, "Aluminum nitride integrated photonics platform for the ultraviolet to visible spectrum," Opt. Express **26**, 11147–11160 (2018).

7. D. M. Lukin, C. Dory, M. A. Guidry, K. Y. Yang, S. D. Mishra, R. Trivedi, M. Radulaski, S. Sun, D. Vercruysse, G. H. Ahn, and J. Vučković, "4H-silicon-carbide-on-insulator for integrated quantum and nonlinear photonics," Nat. Photonics **14**, 330–334 (2020).

8. M. Levy, R. M. Osgood, Jr., R. Liu, L. E. Cross, G. S. Cargill, III, A. Kumar, and H. Bakhru, "Fabrication of single-crystal lithium niobate films by crystal ion slicing," Appl. Phys. Lett. **73**, 2293–2295 (1998).

9. M. Levy and R. M. Osgood, Jr., "Crystal ion-slicing of single-crystal films," USPTO patent 6120597 (September 19, 2000).

10. P. Rabiei and P. Gunter, "Optical and electro-optical properties of submicrometer lithium niobate slab waveguides prepared by crystal ion slicing and wafer bonding," Appl. Phys. Lett. **85**, 4603–4605 (2004).

11. M. Zhang, C. Wang, R. Cheng, A. Shams-Ansari, and M. Lončar, "Monolithic ultra-high-Q lithium niobate microring resonator," Optica **4**, 1536–1537 (2017).

12. R. Wu, M. Wang, J. Xu, J. Qi, W. Chu, Z. Fang, J. Zhang, J. Zhou, L. Qiao, Z. Chai, J. Lin, and Y. Cheng, "Long low-loss-litium niobate on insulator waveguides with sub-nanometer surface roughness," Nanomaterials (Basel) **8**, 910 (2018).

13. R. Wolf, I. Breunig, H. Zappe, and K. Buse, "Scattering-loss reduction of ridge waveguides by sidewall polishing," Opt. Express **26**, 19815–19820 (2018).

14. T. Ding, Y. Zheng, and X. Chen, "On-chip Solc-type polarization control and wavelength filtering utilizing periodically poled lithium niobate on insulator (PPLNOI) ridge waveguide," J. Lightwave Technol. **37**, 1296–1300 (2019).

15. B. Desiatov, A. Shams-Ansari, M. Zhang, C. Wang, and M. Lončar, "Ultra-low-loss integrated visible photonics using thin-film lithium niobate," Optica **6**, 380–384 (2019).

16. M. Xu, M. He, H. Zhang, J. Jian, Y. Pan, X. Liu, L. Chen, X. Meng, H. Chen, Z. Li, X. Xiao, S. Yu, S. Yu, and X. Cai, "High-performance coherent optical modulators based on thin-film lithium niobate platform," Nat. Commun. **11**, 3911 (2020).

17. L. Chang, Y. Li, N. Volet, L. Wang, J. Peters, and J. E. Bowers, "Thin film wavelength converters for photonic integrated circuits," Optica **3**, 531–535 (2016).

18. A. Rao, M. Malinowski, A. Honardoost, J. R. Talukder, P. Rabiei, P. Delfyett, and S. Fathpour, "Second-harmonic generation in periodically-poled thin film lithium niobate wafer-bonded on silicon," Opt. Express **24**, 29941–29947 (2016).

19. S. Y. Siew, E. J. H. Cheung, H. Liang, A. Bettiol, N. Toyoda, B. Alshehri, E. Dogheche, and A. J. Danner, "Ultra-low loss ridge waveguides on lithium niobate via argon ion milling and gas clustered ion beam smoothening," Opt. Express **26**, 4421–4430 (2018).

20. A. J. Mercante, P. Yao, S. Shi, G. Schneider, J. Murakowski, and D. W. Prather, "110 GHz CMOS compatible thin film $LiNbO_3$ modulator on silicon," Opt. Express **24**, 15590–15595 (2016).

21. C. Wang, M. Zhang, X. Chen, M. Bertrand, A. Shams-Ansari, S. Chandrasekhar, P. Winzer, and M. Lončar, "Integrated lithium niobate electro-optic modulators operating at CMOS-compatible voltages," Nature **562**, 101–104 (2018).

22. M. He, M. Xu, Y. Ren, J. Jian, Z. Ruan, Y. Xu, S. Gao, S. Sun, X. Wen, L. Zhou, L. Liu, C. Guo, H. Chen, S. Yu, L. Liu, and X. Cai, "High-performance hybrid silicon and lithium niobate Mach–Zehnder modulators for 100 Gbit s^{-1} and beyond," Nat. Photonics **13**, 359–364 (2019).

23. P. O. Weigel, J. Zhao, K. Fang, H. Al-Rubaye, D. Trotter, D. Hood, J. Mudrick, C. Dallo, A. T. Pomerene, A. L. Starbuck, C. T. DeRose, A. L. Lentine, G. Rebeiz, and S. Mookherjea, "Bonded thin film lithium niobate modulator on a silicon photonics platform exceeding 100 GHz 3-dB electrical modulation bandwidth," Opt. Express **26**, 23728–23739 (2018).

24. A. J. Mercante, S. Shi, P. Yao, L. Xie, R. M. Weikle, and D. W. Prather, "Thin film lithium niobate electro-optic modulator with terahertz operating bandwidth," Opt. Express **26**, 14810–14816 (2018).

25. A. Rao, A. Patil, P. Rabiei, A. Honardoost, R. DeSalvo, A. Paolella, and S. Fathpour, "High-performance and linear thin-film lithium niobate Mach–Zehnder modulators on silicon up to 50 GHz," Opt. Lett. **41**, 5700–5703 (2016).

26. M. Zhang, B. Buscaino, C. Wang, A. Shams-Ansari, C. Reimer, R. Zhu, J. M. Kahn, and M. Lončar, "Broadband electro-optic frequency comb generation in a lithium niobate microring resonator," Nature **568**, 373–377 (2019).

27. Y. He, Q.-F. Yang, J. Ling, R. Luo, H. Liang, M. Li, B. Shen, H. Wang, K. Vahala, and Q. Lin, "Self-starting bi-chromatic $LiNbO_3$ soliton microcomb," Optica **6**, 1138–1144 (2019).

28. C. Wang, M. Zhang, M. Yu, R. Zhu, H. Hu, and M. Loncar, "Monolithic lithium niobate photonic circuits for Kerr frequency comb generation and modulation," Nat. Commun. **10**, 978 (2019).

29. C. Wang, C. Langrock, A. Marandi, M. Jankowski, M. Zhang, B. Desiatov, M. M. Fejer, and M. Lončar, "Ultrahigh-efficiency wavelength conversion in nanophotonic periodically poled lithium niobate waveguides," Optica **5**, 1438–1441 (2018).

30. J.-Y. Chen, Z.-H. Ma, Y. M. Sua, Z. Li, C. Tang, and Y.-P. Huang, "Ultra-efficient frequency conversion in quasi-phase-matched lithium niobate microrings," Optica **6**, 1244–1245 (2019).

31. J. Lu, J. B. Surya, X. Liu, A. W. Bruch, Z. Gong, Y. Xu, and H. X. Tang, "Periodically poled thin-film lithium niobate microring resonators with a second-harmonic generation efficiency of 250,000%/W," Optica **6**, 1455–1460 (2019).

32. J.-Y. Chen, Y. M. Sua, Z.-H. Ma, C. Tang, Z. Li, and Y.-P. Huang, "Efficient parametric frequency conversion in lithium niobate nanophotonic chips," OSA Continuum **2**, 2914–2924 (2019).

33. B. S. Elkus, K. Abdelsalam, A. Rao, V. Velev, S. Fathpour, P. Kumar, and G. S. Kanter, "Generation of broadband correlated photon-pairs in short thin-film lithium-niobate waveguides," Opt. Express **27**, 38521–38531 (2019).

34. J. Zhao, C. Ma, M. Rüsing, and S. Mookherjea, "High quality entangled photon pair generation in periodically poled thin-film lithium niobate waveguides," Phys. Rev. Lett. **124**, 163603 (2020).

35. G. Poberaj, H. Hu, W. Sohler, and P. Günter, "Lithium niobate on insulator (LNOI) for micro-photonic devices," Laser Photon. Rev. **6**, 488–503 (2012).

36. M. Bazzan and C. Sada, "Optical waveguides in lithium niobate: recent developments and applications," Appl. Phys. Rev. **2**, 040603 (2015).

37. A. Boes, B. Corcoran, L. Chang, J. Bowers, and A. Mitchell, "Status and potential of lithium niobate on insulator (LNOI) for photonic integrated circuits," Laser Photon. Rev. **12**, 1700256 (2018).

38. M. Sumets, *Thin Films of Lithium Niobate: Potential Applications, Synthesis Methods, Structure and Properties* (IOP Publishing, 2018).

39. M. Rüsing, P. O. Weigel, J. Zhao, and S. Mookherjea, "Towards 3D integrated photonics including lithium niobate thin films," IEEE Nanotechnol. Mag. **13**(4), 18–33 (2019).

40. Y. Qi and Y. Li, "Integrated lithium niobate photonics," Nanophotonics **9**, 1287–1320 (2020).

41. A. Honardoost, K. Abdelsalam, and S. Fathpour, "Rejuvenating a versatile photonic material: thin-film lithium niobate," Laser Photon. Rev. **14**, 2000088 (2020).

42. C. Wang, M. Zhang, and M. Lončar, "High-Q lithium niobate microcavities and their applications," in *Ultra-High-Q Optical Microcavities* (World Scientific, 2020).

43. R. S. Weis and T. K. Gaylord, "Lithium niobate: summary of physical properties and crystal structure," Appl. Phys. A **37**, 191–203 (1985).

44. "*Polarization reversal and ferroelectric domains in LiNbO$_3$ crystals*," in Lithium Niobate, Springer Series in Materials Science (Springer, 2008), pp. 153–212.

45. V. Gopalan, V. Dierolf, and D. A. Scrymgeour, "Defect–domain wall interactions in trigonal ferroelectrics," Annu. Rev. Mater. Res. **37**, 449–489 (2007).

46. L. Moretti, M. Iodice, F. G. Della Corte, and I. Rendina, "Temperature dependence of the thermo-optic coefficient of lithium niobate, from 300 to 515 K in the visible and infrared regions," J. Appl. Phys. **98**, 036101 (2005).

47. S. T. Popescu, A. Petris, and V. I. Vlad, "Interferometric measurement of the pyroelectric coefficient in lithium niobate," J. Appl. Phys. **113**, 043101 (2013).

48. Y. Sakashita and H. Segawa, "Preparation and characterization of LiNbO$_3$ thin films produced by chemical-vapor deposition," J. Appl. Phys. **77**, 5995–5999 (1995).

49. X. Lansiaux, E. Dogheche, D. Remiens, M. Guilloux-Viry, A. Perrin, and P. Ruterana, "LiNbO$_3$ thick films grown on sapphire by using a multistep sputtering process," J. Appl. Phys. **90**, 5274–5277 (2001).

50. Y. Nakata, S. Gunji, T. Okada, and M. Maeda, "Fabrication of LiNbO$_3$ thin films by pulsed laser deposition and investigation of nonlinear properties," Appl. Phys. A **79**, 1279–1282 (2004).

51. J. Yoon and K. Kim, "Growth of highly textured LiNbO$_3$ thin film on Si with MgO buffer layer through the sol-gel process," Appl. Phys. Lett. **68**, 2523–2525 (1996).

52. F. Gitmans, Z. Sitar, and P. Günter, "Growth of tantalum oxide and lithium tantalate thin films by molecular beam epitaxy," Vacuum **46**, 939–942 (1995).

53. M. Bruel, "Silicon on insulator material technology," Electron. Lett. **31**, 1201–1202 (1995).

54. M. Levy and A. M. Radojevic, "Single-crystal lithium niobate films by crystal ion slicing," in *Wafer Bonding*, Springer Series in Materials Science (Springer, 2004), pp. 417–450.

55. A. Guarino, G. Poberaj, D. Rezzonico, R. Degl'Innocenti, and P. Günter, "Electro-optically tunable microring resonators in lithium niobate," Nat. Photonics **1**, 407–410 (2007).

56. H. Hu, R. Ricken, and W. Sohler, "Large area, crystal-bonded LiNbO$_3$ thin films and ridge waveguides of high refractive index contrast," in *Proc. Topical Meeting "Photorefractive Materials, Effects, and Devices-Control of Light and Matter"(PR09)*, Bad Honnef, Germany (2009).

57. H. Hu, L. Gui, R. Ricken, and W. Sohler, "Towards nonlinear photonic wires in lithium niobate," Proc. SPIE **7604**, 76040R (2010).

58. F. Chen, X.-L. Wang, and K.-M. Wang, "Development of ion-implanted optical waveguides in optical materials: a review," Opt. Mater. **29**, 1523–1542 (2007).

59. J. Lv, Y. Cheng, W. Yuan, X. Hao, and F. Chen, "Three-dimensional femtosecond laser fabrication of waveguide beam splitters in LiNbO$_3$ crystal," Opt. Mater. Express **5**, 1274–1280 (2015).

60. M. F. Volk, S. Suntsov, C. E. Rüter, and D. Kip, "Low loss ridge waveguides in lithium niobate thin films by optical grade diamond blade dicing," Opt. Express **24**, 1386–1391 (2016).

61. G. Ulliac, B. Guichardaz, J.-Y. Rauch, S. Queste, S. Benchabane, and N. Courjal, "Ultra-smooth LiNbO$_3$ micro and nano structures for photonic applications," Microelectron. Eng. **88**, 2417–2419 (2011).

62. N. Courjal, B. Guichardaz, G. Ulliac, J.-Y. Rauch, B. Sadani, H.-H. Lu, and M.-P. Bernal, "High aspect ratio lithium niobate ridge waveguides fabricated by optical grade dicing," J. Phys. D **44**, 305101 (2011).

63. R. Takigawa, E. Higurashi, T. Kawanishi, and T. Asano, "Lithium niobate ridged waveguides with smooth vertical sidewalls fabricated by an ultra-precision cutting method," Opt. Express **22**, 27733–27738 (2014).

64. J. Lin, J. Zhou, R. Wu, M. Wang, Z. Fang, W. Chu, J. Zhang, L. Qiao, and Y. Cheng, "High-precision propagation-loss measurement of single-mode optical waveguides on lithium niobate on insulator," Micromachines (Basel) **10**, 612 (2019).

65. M. Wang, R. Wu, J. Lin, J. Zhang, Z. Fang, Z. Chai, and Y. Cheng, "Chemo-mechanical polish lithography: a pathway to low loss large-scale photonic integration on lithium niobate on insulator," Quantum Eng. **1**, e9 (2019).

66. R. Wu, J. Lin, M. Wang, Z. Fang, W. Chu, J. Zhang, J. Zhou, and Y. Cheng, "Fabrication of a multifunctional photonic integrated chip on lithium niobate on insulator using femtosecond laser-assisted chemomechanical polish," Opt. Lett. **44**, 4698–4701 (2019).

67. J.-X. Zhou, R.-H. Gao, J. Lin, M. Wang, W. Chu, W.-B. Li, D.-F. Yin, L. Deng, Z.-W. Fang, J.-H. Zhang, R.-B. Wu, and Y. Cheng, "Electro-optically switchable optical true delay lines of meter-scale lengths fabricated on lithium niobate on insulator using photolithography assisted chemo-mechanical etching," Chin. Phys. Lett. **37**, 084201 (2020).

68. H. Hu, R. Ricken, W. Sohler, and R. B. Wehrspohn, "Lithium niobate ridge waveguides fabricated by wet etching," IEEE Photon. Technol. Lett. **19**, 417–419 (2007).

69. R. Geiss, S. Saravi, A. Sergeyev, S. Diziain, F. Setzpfandt, F. Schrempel, R. Grange, E.-B. Kley, A. Tünnermann, and T. Pertsch, "Fabrication of nanoscale

lithium niobate waveguides for second-harmonic generation," Opt. Lett. **40**, 2715–2718 (2015).

70. R. Geiss, J. Brandt, H. Hartung, A. Tünnermann, T. Pertsch, E.-B. Kley, and F. Schrempel, "Photonic microstructures in lithium niobate by potassium hydroxide-assisted ion beam-enhanced etching," J. Vac. Sci. Technol. B **33**, 010601 (2015).

71. L. Cai, Y. Wang, and H. Hu, "Low-loss waveguides in a single-crystal lithium niobate thin film," Opt. Lett. **40**, 3013–3016 (2015).

72. L. Cai, Y. Kang, and H. Hu, "Electric-optical property of the proton exchanged phase modulator in single-crystal lithium niobate thin film," Opt. Express **24**, 4640–4647 (2016).

73. L. Cai, R. Kong, Y. Wang, and H. Hu, "Channel waveguides and y-junctions in x-cut single-crystal lithium niobate thin film," Opt. Express **23**, 29211–29221 (2015).

74. S.-M. Zhang, Y.-P. Jiang, and Y. Jiao, "Clean waveguides in lithium niobate thin film formed by He ion implantation," Appl. Phys. B **123**, 220 (2017).

75. M. L. Bortz, L. A. Eyres, and M. M. Fejer, "Depth profiling of the d_{33} nonlinear coefficient in annealed proton exchanged $LiNbO_3$ waveguides," Appl. Phys. Lett. **62**, 2012–2014 (1993).

76. M. Yu, B. Desiatov, Y. Okawachi, A. L. Gaeta, and M. Lončar, "Coherent two-octave-spanning supercontinuum generation in lithium-niobate waveguides," Opt. Lett. **44**, 1222–1225 (2019).

77. H. Hu, A. P. Milenin, R. B. Wehrspohn, H. Hermann, and W. Sohler, "Plasma etching of proton-exchanged lithium niobate," J. Vac. Sci. Technol. A **24**, 1012–1015 (2006).

78. H. Nagata, N. Mitsugi, K. Shima, M. Tamai, and E. M. Haga, "Growth of crystalline LiF on CF_4 plasma etched $LiNbO_3$ substrates," J. Cryst. Growth **187**, 573–576 (1998).

79. Z. Ren, P. J. Heard, J. M. Marshall, P. A. Thomas, and S. Yu, "Etching characteristics of $LiNbO_3$ in reactive ion etching and inductively coupled plasma," J. Appl. Phys. **103**, 034109 (2008).

80. D. Jun, J. Wei, C. E. Png, S. Guangyuan, J. Son, H. Yang, and A. J. Danner, "Deep anisotropic $LiNbO_3$ etching with SF_6/Ar inductively coupled plasmas," J. Vac. Sci. Technol. B **30**, 011208 (2012).

81. G. Si, A. J. Danner, S. L. Teo, E. J. Teo, J. Teng, and A. A. Bettiol, "Photonic crystal structures with ultrahigh aspect ratio in lithium niobate fabricated by focused ion beam milling," J. Vac. Sci. Technol. B **29**, 021205 (2011).

82. F. Lacour, N. Courjal, M.-P. Bernal, A. Sabac, C. Bainier, and M. Spajer, "Nanostructuring lithium niobate substrates by focused ion beam milling," Opt. Mater. **27**, 1421–1425 (2005).

83. F. Chen, "Photonic guiding structures in lithium niobate crystals produced by energetic ion beams," J. Appl. Phys. **106**, 081101 (2009).

84. E. Saitoh, Y. Kawaguchi, K. Saitoh, and M. Koshiba, "A design method of lithium niobate on insulator ridge waveguides without leakage loss," Opt. Express **19**, 15833–15842 (2011).

85. C. Wang, M. Zhang, B. Stern, M. Lipson, and M. Lončar, "Nanophotonic lithium niobate electro-optic modulators," Opt. Express **26**, 1547–1555 (2018).

86. I. Krasnokutska, J.-L. J. Tambasco, X. Li, and A. Peruzzo, "Ultra-low loss photonic circuits in lithium niobate on insulator," Opt. Express **26**, 897–904 (2018).

87. L. Cai, A. Mahmoud, and G. Piazza, "Low-loss waveguides on Y-cut thin film lithium niobate: towards acousto-optic applications," Opt. Express **27**, 9794–9802 (2019).

88. J. Ling, Y. He, R. Luo, M. Li, H. Liang, and Q. Lin, "Athermal lithium niobate microresonator," Opt. Express **28**, 21682–21691 (2020).
89. G. Ulliac, V. Calero, A. Ndao, F. I. Baida, and M.-P. Bernal, "Argon plasma inductively coupled plasma reactive ion etching study for smooth sidewall thin film lithium niobate waveguide application," Opt. Mater. **53**, 1–5 (2016).
90. H. Hui, R. Ricken, and W. Sohler, "Etching of lithium niobate: from ridge waveguides to photonic crystal structures," in *ECIO*, Eindhoven, The Netherlands (2008).
91. L. Gui, H. Hu, M. Garcia-Granda, and W. Sohler, "Local periodic poling of ridges and ridge waveguides on X- and Y-Cut LiNbO$_3$ and its application for second harmonic generation," Opt. Express **17**, 3923–3928 (2009).
92. P. Ferraro, S. Grilli, and P. D. Natale, eds., *Ferroelectric Crystals for Photonic Applications: Including Nanoscale Fabrication and Characterization Techniques* (Springer, 2009).
93. V. S. Ilchenko, A. A. Savchenkov, A. B. Matsko, and L. Maleki, "Nonlinear optics and crystalline whispering gallery mode cavities," Phys. Rev. Lett. **92**, 043903 (2004).
94. R. Wolf, I. Breunig, H. Zappe, and K. Buse, "Cascaded second-order optical nonlinearities in on-chip micro rings," Opt. Express **25**, 29927–29933 (2017).
95. D. T. Spencer, J. F. Bauters, M. J. R. Heck, and J. E. Bowers, "Integrated waveguide coupled Si$_3$N$_4$ resonators in the ultrahigh-Q regime," Optica **1**, 153–157 (2014).
96. S. Jin, L. Xu, H. Zhang, and Y. Li, "LiNbO$_3$ thin-film modulators using silicon nitride surface ridge waveguides," IEEE Photon. Technol. Lett. **28**, 736–739 (2015).
97. A. Rao and S. Fathpour, "Heterogeneous thin-film lithium niobate integrated photonics for electrooptics and nonlinear optics," IEEE J. Sel. Top. Quantum Electron. **24**, 8200912 (2018).
98. A. N. R. Ahmed, S. Shi, M. Zablocki, P. Yao, and D. W. Prather, "Tunable hybrid silicon nitride and thin-film lithium niobate electro-optic microresonator," Opt. Lett. **44**, 618–621 (2019).
99. K. K. Mehta, G. N. West, and R. J. Ram, "SiN-on-LiNbO$_3$ integrated optical modulation at visible," in *Conference on Lasers and Electro-Optics* (OSA, 2017).
100. S. Li, L. Cai, Y. Wang, Y. Jiang, and H. Hu, "Waveguides consisting of single-crystal lithium niobate thin film and oxidized titanium stripe," Opt. Express **23**, 24212–24219 (2015).
101. T. Jin, J. Zhou, and P. T. Lin, "Mid-infrared electro-optical modulation using monolithically integrated titanium dioxide on lithium niobate optical waveguides," Sci. Rep. **9**, 15130 (2019).
102. A. Rao, A. Patil, J. Chiles, M. Malinowski, S. Novak, K. Richardson, P. Rabiei, and S. Fathpour, "Heterogeneous microring and Mach-Zehnder modulators based on lithium niobate and chalcogenide glasses on silicon," Opt. Express **23**, 22746–22752 (2015).
103. P. Rabiei, J. Ma, S. Khan, J. Chiles, and S. Fathpour, "Heterogeneous lithium niobate photonics on silicon substrates," Opt. Express **21**, 25573–25581 (2013).
104. Y. Wang, Z. Chen, L. Cai, Y. Jiang, H. Zhu, and H. Hu, "Amorphous silicon-lithium niobate thin film strip-loaded waveguides," Opt. Mater. Express **7**, 4018–4028 (2017).
105. L. Cao, A. Aboketaf, Z. Wang, and S. Preble, "Hybrid amorphous silicon (a-Si:H)–LiNbO$_3$ electro-optic modulator," Opt. Commun. **330**, 40–44 (2014).
106. Z. Yu, X. Xi, J. Ma, H. K. Tsang, C.-L. Zou, and X. Sun, "Photonic integrated circuits with bound states in the continuum," Optica **6**, 1342–1348 (2019).

107. Z. Yu, Y. Tong, H. K. Tsang, and X. Sun, "High-dimensional communication on etchless lithium niobate platform with photonic bound states in the continuum," Nat. Commun. **11**, 2602 (2020).

108. C.-L. Zou, J.-M. Cui, F.-W. Sun, X. Xiong, X.-B. Zou, Z.-F. Han, and G.-C. Guo, "Guiding light through optical bound states in the continuum for ultrahigh-Q microresonators," Laser Photon. Rev. **9**, 114–119 (2015).

109. L. Chen and R. M. Reano, "Compact electric field sensors based on indirect bonding of lithium niobate to silicon microrings," Opt. Express **20**, 4032–4038 (2012).

110. L. Chang, M. H. P. Pfeiffer, N. Volet, M. Zervas, J. D. Peters, C. L. Manganelli, E. J. Stanton, Y. Li, T. J. Kippenberg, and J. E. Bowers, "Heterogeneous integration of lithium niobate and silicon nitride waveguides for wafer-scale photonic integrated circuits on silicon," Opt. Lett. **42**, 803–806 (2017).

111. Y. S. Lee, G.-D. Kim, W.-J. Kim, S.-S. Lee, W.-G. Lee, and W. H. Steier, "Hybrid Si-LiNbO$_3$ microring electro-optically tunable resonators for active photonic devices," Opt. Lett. **36**, 1119–1121 (2011).

112. L. Chen, M. G. Wood, and R. M. Reano, "12.5 pm/V hybrid silicon and lithium niobate optical microring resonator with integrated electrodes," Opt. Express **21**, 27003–27010 (2013).

113. L. Chen, Q. Xu, M. G. Wood, and R. M. Reano, "Hybrid silicon and lithium niobate electro-optical ring modulator," Optica **1**, 112–118 (2014).

114. J. D. Witmer, J. A. Valery, P. Arrangoiz-Arriola, C. J. Sarabalis, J. T. Hill, and A. H. Safavi-Naeini, "High-Q photonic resonators and electro-optic coupling using silicon-on-lithium-niobate," Sci. Rep. **7**, 46313 (2017).

115. S. Jin, L. Xu, H. Zhang, and Y. Li, "LiNbO$_3$ thin-film modulators using silicon nitride surface ridge waveguides," IEEE Photon. Technol. Lett. **28**, 736–739 (2016).

116. M. Jin, J.-Y. Chen, Y. M. Sua, and Y.-P. Huang, "High-extinction electro-optic modulation on lithium niobate thin film," Opt. Lett. **44**, 1265–1268 (2019).

117. C. Wang, X. Xiong, N. Andrade, V. Venkataraman, X.-F. Ren, G.-C. Guo, and M. Lončar, "Second harmonic generation in nano-structured thin-film lithium niobate waveguides," Opt. Express **25**, 6963–6973 (2017).

118. H. Hu, R. Ricken, and W. Sohler, "Lithium niobate photonic wires," Opt. Express **17**, 24261–24268 (2009).

119. L. He, M. Zhang, A. Shams-Ansari, R. Zhu, C. Wang, and M. Loncar, "Low-loss fiber-to-chip interface for lithium niobate photonic integrated circuits," Opt. Lett. **44**, 2314–2317 (2019).

120. I. Krasnokutska, R. J. Chapman, J.-L. J. Tambasco, and A. Peruzzo, "High coupling efficiency grating couplers on lithium niobate on insulator," Opt. Express **27**, 17681–17685 (2019).

121. J. Jian, P. Xu, H. Chen, M. He, Z. Wu, L. Zhou, L. Liu, C. Yang, and S. Yu, "High-efficiency hybrid amorphous silicon grating couplers for sub-micron-sized lithium niobate waveguides," Opt. Express **26**, 29651–29658 (2018).

122. G. Qian, L. Huang, F. Zhou, J. Tang, X. Chen, Y. Kong, and T. Chen, "Design and fabrication of cantilevered fiber-to-waveguide mode size converter for thin-film lithium niobate photonic integrated circuits," Proc. SPIE **11455**, 1145587 (2020).

123. N. Yao, J. Zhou, R. Gao, J. Lin, M. Wang, Y. Cheng, W. Fang, and L. Tong, "Efficient light coupling between an ultra-low loss lithium niobate waveguide and an adiabatically tapered single mode optical fiber," Opt. Express **28**, 12416–12423 (2020).

124. Y. Li, T. Lan, J. Li, and Z. Wang, "High-efficiency edge-coupling based on lithium niobate on an insulator wire waveguide," Appl. Opt. **59**, 6694–6701 (2020).

125. I. Krasnokutska, J.-L. J. Tambasco, and A. Peruzzo, "Nanostructuring of LNOI for efficient edge coupling," Opt. Express **27**, 16578–16585 (2019).

126. Y. Pan, S. Sun, M. Xu, M. He, S. Yu, and X. Cai, "Low fiber-to-fiber loss, large bandwidth and low drive voltage lithium niobate on insulator modulators," in *Conference on Lasers and Electro-Optics* (OSA, 2020).

127. C. Hu, A. Pan, T. Li, X. Wang, Y. Liu, S. Tao, C. Zeng, and J. Xia, "High-efficient and polarization independent edge coupler for thin-film lithium niobite waveguide devices," arXiv:2009.02855 (2020).

128. Z. Chen, R. Peng, Y. Wang, H. Zhu, and H. Hu, "Grating coupler on lithium niobate thin film waveguide with a metal bottom reflector," Opt. Mater. Express **7**, 4010–4017 (2017).

129. Z. Chen, Y. Wang, Y. Jiang, R. Kong, and H. Hu, "Grating coupler on single-crystal lithium niobate thin film," Opt. Mater. **72**, 136–139 (2017).

130. A. Kar, M. Bahadori, S. Gong, and L. L. Goddard, "Realization of alignment-tolerant grating couplers for z-cut thin-film lithium niobate," Opt. Express **27**, 15856–15867 (2019).

131. M. S. Nisar, X. Zhao, A. Pan, S. Yuan, and J. Xia, "Grating coupler for an on-chip lithium niobate ridge waveguide," IEEE Photon. J. **9**, 6600208 (2017).

132. M. A. Baghban, J. Schollhammer, C. Errando-Herranz, K. B. Gylfason, and K. Gallo, "Bragg gratings in thin-film LiNbO$_3$ waveguides," Opt. Express **25**, 32323–32332 (2017).

133. S. Wang, L. Yang, R. Cheng, Y. Xu, M. Shen, R. L. Cone, C. W. Thiel, and H. X. Tang, "Incorporation of erbium ions into thin-film lithium niobate integrated photonics," Appl. Phys. Lett. **116**, 151103 (2020).

134. T. G. Tiecke, K. P. Nayak, J. D. Thompson, T. Peyronel, N. P. de Leon, V. Vuletić, and M. D. Lukin, "Efficient fiber-optical interface for nanophotonic devices," Optica **2**, 70–75 (2015).

135. S. Khan, S. M. Buckley, J. Chiles, R. P. Mirin, S. W. Nam, and J. M. Shainline, "Low-loss, high-bandwidth fiber-to-chip coupling using capped adiabatic tapered fibers," APL Photon. **5**, 056101 (2020).

136. Y. Ding, C. Peucheret, H. Ou, and K. Yvind, "Fully etched apodized grating coupler on the SOI platform with -0.58 dB coupling efficiency," Opt. Lett. **39**, 5348–5350 (2014).

137. X. Yin, J. Jin, M. Soljačić, C. Peng, and B. Zhen, "Observation of topologically enabled unidirectional guided resonances," Nature **580**, 467–471 (2020).

138. J. C. C. Mak, W. D. Sacher, H. Ying, X. Luo, P. G.-Q. Lo, and J. K. S. Poon, "Multi-layer silicon nitride-on-silicon polarization-independent grating couplers," Opt. Express **26**, 30623–30633 (2018).

139. R. Marchetti, C. Lacava, L. Carroll, K. Gradkowski, and P. Minzioni, "Coupling strategies for silicon photonics integrated chips," Photon. Res. **7**, 201–239 (2019).

140. C. Wang, M. J. Burek, Z. Lin, H. A. Atikian, V. Venkataraman, I.-C. Huang, P. Stark, and M. Lončar, "Integrated high quality factor lithium niobate microdisk resonators," Opt. Express **22**, 30924–30933 (2014).

141. H. Liang, R. Luo, Y. He, H. Jiang, and Q. Lin, "High-quality lithium niobate photonic crystal nanocavities," Optica **4**, 1251–1258 (2017).

142. M. Li, H. Liang, R. Luo, Y. He, and Q. Lin, "High-Q 2D lithium niobate photonic crystal slab nanoresonators," Laser Photon. Rev. **13**, 1800228 (2019).

143. L. Wang, C. Wang, J. Wang, F. Bo, M. Zhang, Q. Gong, M. Lončar, and Y.-F. Xiao, "High-Q chaotic lithium niobate microdisk cavity," Opt. Lett. **43**, 2917–2920 (2018).

144. J. Wang, F. Bo, S. Wan, W. Li, F. Gao, J. Li, G. Zhang, and J. Xu, "High-Q lithium niobate microdisk resonators on a chip for efficient electro-optic modulation," Opt. Express **23**, 23072–23078 (2015).

145. J. Lin, Y. Xu, Z. Fang, M. Wang, J. Song, N. Wang, L. Qiao, W. Fang, and Y. Cheng, "Fabrication of high-Q lithium niobate microresonators using femtosecond laser micromachining," Sci. Rep. **5**, 8072 (2015).

146. J. Lin, Y. Xu, J. Ni, M. Wang, Z. Fang, L. Qiao, W. Fang, and Y. Cheng, "Phase-matched second-harmonic generation in an on-chip $LiNbO_3$ microresonator," Phys. Rev. Appl. **6**, 014002 (2016).

147. M. Wang, Y. Xu, Z. Fang, Y. Liao, P. Wang, W. Chu, L. Qiao, J. Lin, W. Fang, and Y. Cheng, "On-chip electro-optic tuning of a lithium niobate microresonator with integrated in-plane microelectrodes," Opt. Express **25**, 124–129 (2017).

148. Z. Fang, Y. Xu, M. Wang, L. Qiao, J. Lin, W. Fang, and Y. Cheng, "Monolithic integration of a lithium niobate microresonator with a free-standing waveguide using femtosecond laser assisted ion beam writing," Sci. Rep. **7**, 45610 (2017).

149. S. Liu, Y. Zheng, and X. Chen, "Cascading second-order nonlinear processes in a lithium niobate-on-insulator microdisk," Opt. Lett. **42**, 3626–3629 (2017).

150. J. Lin, N. Yao, Z. Hao, J. Zhang, W. Mao, M. Wang, W. Chu, R. Wu, Z. Fang, L. Qiao, W. Fang, F. Bo, and Y. Cheng, "Broadband quasi-phase-matched harmonic generation in an on-chip monocrystalline lithium niobate microdisk resonator," Phys. Rev. Lett. **122**, 173903 (2019).

151. X. Ye, S. Liu, Y. Chen, Y. Zheng, and X. Chen, "Sum-frequency generation in lithium-niobate-on-insulator microdisk via modal phase matching," Opt. Lett. **45**, 523–526 (2020).

152. R. Wu, J. Zhang, N. Yao, W. Fang, L. Qiao, Z. Chai, J. Lin, and Y. Cheng, "Lithium niobate micro-disk resonators of quality factors above 107," Opt. Lett. **43**, 4116–4119 (2018).

153. Z. Fang, S. Haque, J. Lin, R. Wu, J. Zhang, M. Wang, J. Zhou, M. Rafa, T. Lu, and Y. Cheng, "Real-time electrical tuning of an optical spring on a monolithically integrated ultrahigh Q lithium nibote microresonator," Opt. Lett. **44**, 1214–1217 (2019).

154. J. Zhang, Z. Fang, J. Lin, J. Zhou, M. Wang, R. Wu, R. Gao, and Y. Cheng, "Fabrication of crystalline microresonators of high quality factors with a controllable wedge angle on lithium niobate on insulator," Nanomaterials (Basel) **9**, 1218 (2019).

155. T.-J. Wang, J.-Y. He, C.-A. Lee, and H. Niu, "High-quality $LiNbO_3$ microdisk resonators by undercut etching and surface tension reshaping," Opt. Express **20**, 28119–28124 (2012).

156. L. Zhang, D. Zheng, W. Li, F. Bo, F. Gao, Y. Kong, G. Zhang, and J. Xu, "Microdisk resonators with lithium-niobate film on silicon substrate," Opt. Express **27**, 33662–33669 (2019).

157. J. Lin, Y. Xu, Z. Fang, M. Wang, N. Wang, L. Qiao, W. Fang, and Y. Cheng, "Second harmonic generation in a high-Q lithium niobate microresonator fabricated by femtosecond laser micromachining," Sci. China. Ser. G **58**, 114209 (2015).

158. R. Luo, H. Jiang, S. Rogers, H. Liang, Y. He, and Q. Lin, "On-chip second-harmonic generation and broadband parametric down-conversion in a lithium niobate microresonator," Opt. Express **25**, 24531–24539 (2017).

159. Z. Hao, J. Wang, S. Ma, W. Mao, F. Bo, F. Gao, G. Zhang, and J. Xu, "Sum-frequency generation in on-chip lithium niobate microdisk resonators," Photon. Res. **5**, 623–628 (2017).

160. S. Liu, Y. Zheng, Z. Fang, X. Ye, Y. Cheng, and X. Chen, "Effective four-wave mixing in the lithium niobate on insulator microdisk by cascading quadratic processes," Opt. Lett. **44**, 1456–1459 (2019).

161. Z. Hao, L. Zhang, W. Mao, A. Gao, X. Gao, F. Gao, F. Bo, G. Zhang, and J. Xu, "Second-harmonic generation using d_{33} in periodically poled lithium niobate microdisk resonators," Photon. Res. **8**, 311–317 (2020).

162. L. Zhang, Z. Hao, Q. Luo, A. Gao, R. Zhang, C. Yang, F. Gao, F. Bo, G. Zhang, and J. Xu, "Dual-periodically poled lithium niobate microcavities supporting multiple coupled parametric processes," Opt. Lett. **45**, 3353–3356 (2020).

163. M. Eichenfield, *Reduced Dimensionality Lithium Niobate Microsystems* (Sandia National Lab, 2017).

164. W. C. Jiang and Q. Lin, "Chip-scale cavity optomechanics in lithium niobate," Sci. Rep. **6**, 36920 (2016).

165. L. Shao, M. Yu, S. Maity, N. Sinclair, L. Zheng, C. Chia, A. Shams-Ansari, C. Wang, M. Zhang, K. Lai, and M. Lončar, "Microwave-to-optical conversion using lithium niobate thin-film acoustic resonators," Optica **6**, 1498–1505 (2019).

166. S. Y. Siew, S. S. Saha, M. Tsang, and A. J. Danner, "Rib microring resonators in lithium niobate on insulator," IEEE Photon. Technol. Lett. **28**, 573–576 (2016).

167. J. Lu, M. Li, C. Zou, A. A. Sayem, and H. Tang, "Towards 1% single photon nonlinearity with periodically-poled lithium niobate microring resonators," Optica **7**, 1654–1659 (2020).

168. R. Wolf, Y. Jia, S. Bonaus, C. S. Werner, S. J. Herr, I. Breunig, K. Buse, and H. Zappe, "Quasi-phase-matched nonlinear optical frequency conversion in on-chip whispering galleries," Optica **5**, 872–875 (2018).

169. J.-Y. Chen, Y. M. Sua, H. Fan, and Y.-P. Huang, "Modal phase matched lithium niobate nanocircuits for integrated nonlinear photonics," OSA Continuum **1**, 229–242 (2018).

170. R. Luo, Y. He, H. Liang, M. Li, J. Ling, and Q. Lin, "Optical parametric generation in a lithium niobate microring with modal phase matching," Phys. Rev. Appl. **11**, 034026 (2019).

171. Z. Gong, X. Liu, Y. Xu, M. Xu, J. B. Surya, J. Lu, A. Bruch, C. Zou, and H. X. Tang, "Soliton microcomb generation at 2 μm in z-cut lithium niobate microring resonators," Opt. Lett. **44**, 3182–3185 (2019).

172. M. Yu, Y. Okawachi, R. Cheng, C. Wang, M. Zhang, A. L. Gaeta, and M. Lončar, "Raman lasing and soliton mode-locking in lithium niobate microresonators," Light Sci Appl **9**, 9 (2020).

173. M. Zhang, C. Wang, Y. Hu, A. Shams-Ansari, T. Ren, S. Fan, and M. Lončar, "Electronically programmable photonic molecule," Nat. Photonics **13**, 36–40 (2019).

174. Y. Hu, M. Yu, D. Zhu, N. Sinclair, A. Shams-Ansari, L. Shao, J. Holzgrafe, E. Puma, M. Zhang, and M. Loncar, "Reconfigurable electro-optic frequency shifter," arXiv:2005.09621 (2020).

175. J. Holzgrafe, N. Sinclair, D. Zhu, A. Shams-Ansari, M. Colangelo, Y. Hu, M. Zhang, K. K. Berggren, and M. Lončar, "Cavity electro-optics in thin-film lithium niobate for efficient microwave-to-optical transduction," Optica **7**, 1714–1720 (2020).

176. T. P. McKenna, J. D. Witmer, R. N. Patel, W. Jiang, R. Van Laer, P. Arrangoiz-Arriola, E. Alex Wollack, J. F. Herrmann, and A. H. Safavi-Naeini, "Cryogenic

microwave-to-optical conversion using a triply-resonant lithium niobate on sapphire transducer," Optica **7**, 1737–1745 (2020).

177. W. Jiang, C. J. Sarabalis, Y. D. Dahmani, R. N. Patel, F. M. Mayor, T. P. McKenna, R. Van Laer, and A. H. Safavi-Naeini, "Efficient bidirectional piezo-optomechanical transduction between microwave and optical frequency," Nat. Commun. **11**, 1166 (2020).

178. S. Diziain, R. Geiss, M. Zilk, F. Schrempel, E.-B. Kley, A. Tünnermann, and T. Pertsch, "Second harmonic generation in free-standing lithium niobate photonic crystal L3 cavity," Appl. Phys. Lett. **103**, 051117 (2013).

179. H. Jiang, H. Liang, R. Luo, X. Chen, Y. Chen, and Q. Lin, "Nonlinear frequency conversion in one dimensional lithium niobate photonic crystal nanocavities," Appl. Phys. Lett. **113**, 021104 (2018).

180. W. Jiang, R. N. Patel, F. M. Mayor, T. P. McKenna, P. Arrangoiz-Arriola, C. J. Sarabalis, J. D. Witmer, R. Van Laer, and A. H. Safavi-Naeini, "Lithium niobate piezo-optomechanical crystals," Optica **6**, 845–853 (2019).

181. M. Li, H. Liang, R. Luo, Y. He, J. Ling, and Q. Lin, "Photon-level tuning of photonic nanocavities," Optica **6**, 860–863 (2019).

182. M. Li, J. Ling, Y. He, U. A. Javid, S. Xue, and Q. Lin, "Lithium niobate photonic-crystal electro-optic modulator," Nat. Commun. **11**, 4123 (2020).

183. R. W. Boyd, *Nonlinear Optics* (Elsevier, 2019).

184. H. A. Haus, *Waves and Fields in Optoelectronics* (Prentice-Hall, 1984).

185. A. Yariv and P. Yeh, *Photonics: Optical Electronics in Modern Communications*, The Oxford Series in Electrical and Computer Engineering (Oxford University, 2006).

186. C. Qin, H. Lu, B. Ercan, S. Li, and S. J. B. Yoo, "Single-tone optical frequency shifting and nonmagnetic optical isolation by electro-optical emulation of a rotating half-wave plate in a traveling-wave lithium niobate waveguide," IEEE Photon. J. **9**, 6600913 (2017).

187. C. Y. Huang, C. H. Lin, Y. H. Chen, and Y. C. Huang, "Electro-optic Ti:PPLN waveguide as efficient optical wavelength filter and polarization mode converter," Opt. Express **15**, 2548–2554 (2007).

188. L. Fan, C.-L. Zou, R. Cheng, X. Guo, X. Han, Z. Gong, S. Wang, and H. X. Tang, "Superconducting cavity electro-optics: a platform for coherent photon conversion between superconducting and photonic circuits," Sci. Adv. **4**, eaar4994 (2018).

189. A. A. Savchenkov, W. Liang, A. B. Matsko, V. S. Ilchenko, D. Seidel, and L. Maleki, "Tunable optical single-sideband modulator with complete sideband suppression," Opt. Lett. **34**, 1300–1302 (2009).

190. R. C. Alferness, "Waveguide electrooptic modulators," IEEE Trans. Microw. Theory Tech. **30**, 1121–1137 (1982).

191. E. L. Wooten, K. M. Kissa, A. Yi-Yan, E. J. Murphy, D. A. Lafaw, P. F. Hallemeier, D. Maack, D. V. Attanasio, D. J. Fritz, G. J. McBrien, and D. E. Bossi, "Review of lithium niobate modulators for fiber-optic communications systems," IEEE J. Sel. Top. Quantum Electron. **6**, 69–82 (2000).

192. D. Janner, D. Tulli, M. García-Granda, M. Belmonte, and V. Pruneri, "Microstructured integrated electro-optic LiNbO$_3$ modulators," Laser Photon. Rev. **3**, 301–313 (2009).

193. T. Ren, M. Zhang, C. Wang, L. Shao, C. Reimer, Y. Zhang, O. King, R. Esman, T. Cullen, and M. Lončar, "An integrated low-voltage broadband lithium niobate phase modulator," IEEE Photon. Technol. Lett. **31**, 889–892 (2019).

194. L. J. Wright, M. Karpiński, C. Söller, and B. J. Smith, "Spectral shearing of quantum light pulses by electro-optic phase modulation," Phys. Rev. Lett. **118**, 023601 (2017).

195. M. Izutsu, S. Shikama, and T. Sueta, "Integrated optical SSB modulator/frequency shifter," IEEE J. Quantum Electron. **17**, 2225–2227 (1981).

196. J. Jian, M. Xu, L. Liu, Y. Luo, J. Zhang, L. Liu, L. Zhou, H. Chen, S. Yu, and X. Cai, "High modulation efficiency lithium niobate Michelson interferometer modulator," Opt. Express **27**, 18731–18739 (2019).

197. M. Xu, W. Chen, M. He, X. Wen, Z. Ruan, J. Xu, L. Chen, L. Liu, S. Yu, and X. Cai, "Michelson interferometer modulator based on hybrid silicon and lithium niobate platform," APL Photon. **4**, 100802 (2019).

198. A. Rao and S. Fathpour, "Compact lithium niobate electrooptic modulators," IEEE J. Sel. Top. Quantum Electron. **24**, 3400114 (2018).

199. A. Honardoost, R. Safian, A. Rao, and S. Fathpour, "High-speed modeling of ultracompact electrooptic modulators," J. Lightwave Technol. **36**, 5893–5902 (2018).

200. N. Boynton, H. Cai, M. Gehl, S. Arterburn, C. Dallo, A. Pomerene, A. Starbuck, D. Hood, D. C. Trotter, T. Friedmann, C. T. DeRose, and A. Lentine, "A heterogeneously integrated silicon photonic/lithium niobate travelling wave electro-optic modulator," Opt. Express **28**, 1868–1884 (2020).

201. A. N. R. Ahmed, S. Nelan, S. Shi, P. Yao, A. Mercante, and D. W. Prather, "Subvolt electro-optical modulator on thin-film lithium niobate and silicon nitride hybrid platform," Opt. Lett. **45**, 1112–1115 (2020).

202. M. Bahadori, L. L. Goddard, and S. Gong, "Fundamental electro-optic limitations of thin-film lithium niobate microring modulators," Opt. Express **28**, 13731–13749 (2020).

203. P. Kharel, C. Reimer, K. Luke, L. He, and M. Zhang, "Breaking voltage-bandwidth limits in integrated lithium niobate modulators using micro-structured electrodes," arXiv:2011.13422 (2020).

204. J. P. Salvestrini, L. Guilbert, M. Fontana, M. Abarkan, and S. Gille, "Analysis and control of the DC drift in $LiNbO_3$-based Mach-Zehnder modulators," J. Lightwave Technol. **29**, 1522–1534 (2011).

205. H. Nagata, N. F. O'Brien, W. R. Bosenberg, G. L. Reiff, and K. R. Voisine, "DC-voltage-induced thermal shift of bias point in $LiNbO_3$ optical modulators," IEEE Photon. Technol. Lett. **16**, 2460–2462 (2004).

206. R. Spickermann, S. R. Sakamoto, and N. Dagli, "In traveling wave modulators which velocity to match?" in *Conference Proceedings LEOS'96 9th Annual Meeting IEEE Lasers and Electro-Optics Society* (1996), Vol. **2**, pp. 97–98.

207. K. Aoki, J. Kondou, O. Mitomi, and M. Minakata, "Velocity-matching conditions for ultrahigh-speed optical $LiNbO_3$ modulators with traveling-wave electrode," Jpn. J. Appl. Phys. Part 1 **45**, 8696–8698 (2006).

208. W. W. Rigrod and I. P. Kaminow, "Wide-band microwave light modulation," Proc. IEEE **51**, 137–140 (1963).

209. D. M. Pozar, *Microwave Engineering* (Wiley, 2005).

210. J. Shin, C. Ozturk, S. R. Sakamoto, Y. J. Chiu, and N. Dagli, "Novel T-rail electrodes for substrate removed low-voltage high-speed GaAs/AlGaAs electrooptic modulators," IEEE Trans. Microw. Theory Tech. **53**, 636–643 (2005).

211. G. Ghione, "Chapter 6: Modulators," in *Semiconductor Devices for High-Speed Optoelectronics* (Cambridge University, 2009).

212. J. A. I. Fuste and M. C. S. Blanco, "Bandwidth–length trade-off figures of merit for electro-optic traveling wave modulators," Opt. Lett. **38**, 1548–1550 (2013).

213. A. Chowdhury and L. McCaughan, "Figure of merit for near-velocity-matched traveling-wave modulators," Opt. Lett. **26**, 1317–1319 (2001).

214. A. N. P. An, C. H. U. Hangran, C. H. Z. Eng, and J. I. X. Ia, "Fundamental mode hybridization in a thin film lithium niobate ridge waveguide," Opt. Express **27**, 35659–35669 (2019).

215. L. Chen, J. Chen, J. Nagy, and R. M. Reano, "Highly linear ring modulator from hybrid silicon and lithium niobate," Opt. Express **23**, 13255–13264 (2015).

216. A. Karim and J. Devenport, "Noise figure reduction in externally modulated analog fiber-optic links," IEEE Photon. Technol. Lett. **19**, 312–314 (2007).

217. P. Rabiei and W. H. Steier, "Lithium niobate ridge waveguides and modulators fabricated using smart guide," Appl. Phys. Lett. **86**, 161115 (2005).

218. J. Chiles and S. Fathpour, "Mid-infrared integrated waveguide modulators based on silicon-on-lithium-niobate photonics," Optica **1**, 350–355 (2014).

219. A. N. R. Ahmed, S. Shi, S. Nelan, A. J. Mercante, P. Yao, and D. W. Prather, "Low-voltage modulators using thin-film lithium niobate," Proc. SPIE **11286**, 112860U (2020).

220. V. Stenger, J. Toney, A. Pollick, J. Busch, J. Scholl, P. Pontius, and S. Sriram, "Engineered thin film lithium niobate substrate for high gain-bandwidth electro-optic modulators," in *CLEO* (Optical Society of America, 2013), paper CW3O.3.

221. V. E. Stenger, J. Toney, A. PoNick, D. Brown, B. Griffin, R. Nelson, and S. Sriram, "Low loss and low Vpi thin film lithium niobate on quartz electro-optic modulators," in *European Conference on Optical Communication (ECOC)* (2017), pp. 1–3.

222. V. Stenger, A. Pollick, and C. Acampado, "Integrable thin film lithium niobate (TFLNTM) on silicon electro-optic modulators," in *Optical Fiber Communication Conference (OFC)* (Optical Society of America, 2019), paper Tu2H.6.

223. Y. Zhang, M. Xu, H. Zhang, M. Li, J. Jian, M. He, L. Chen, L. Wang, X. Cai, X. Xiao, and S. Yu, "220 Gbit/s optical PAM4 modulation based on lithium niobate on insulator modulator," in *45th European Conference on Optical Communication (ECOC)* (2019), pp. 1–4.

224. X. P. Li, K. X. Chen, and L. F. Wang, "Compact and electro-optic tunable interleaver in lithium niobate thin film," Opt. Lett. **43**, 3610–3613 (2018).

225. R. Safian, M. Teng, L. Zhuang, and S. Chakravarty, "Foundry-compatible thin film lithium niobate modulator with RF electrodes buried inside the silicon oxide layer of the SOI wafer," Opt. Express **28**, 25843–25857 (2020).

226. V. E. Stenger, J. Toney, A. PoNick, D. Brown, B. Griffin, R. Nelson, and S. Sriram, "Low loss and low vpi thin film lithium niobate on quartz electro-optic modulators," in *European Conference on Optical Communication (ECOC)* (IEEE, 2017).

227. E. A. Douglas, P. Mahony, A. Starbuck, A. Pomerene, D. C. Trotter, and C. T. DeRose, "Effect of precursors on propagation loss for plasma-enhanced chemical vapor deposition of SiNx:H waveguides," Opt. Mater. Express **6**, 2892–2903 (2016).

228. A. Yariv, "Universal relations for coupling of optical power between microresonators and dielectric waveguides," Electron. Lett. **36**, 321–322 (2000).

229. W. D. Sacher and J. K. S. Poon, "Dynamics of microring resonator modulators," Opt. Express **16**, 15741–15753 (2008).

230. R. Stabile, A. Albores-Mejia, A. Rohit, and K. A. Williams, "Integrated optical switch matrices for packet data networks," Microsyst. Nanoeng. **2**, 15042 (2016).

231. M. J. R. Heck, "Highly integrated optical phased arrays: photonic integrated circuits for optical beam shaping and beam steering," Nanophotonics **6**, 93–107 (2017).

232. T. Baba, "Slow light in photonic crystals," Nat. Photonics **2**, 465–473 (2008).

233. M. Xu, M. He, S. Yu, and X. Cai, "Thin-film lithium niobate modulator based on distributed Bragg grating resonators," in *Asia Communications and Photonics Conference (ACPC)* (Optical Society of America, 2019), paper S4D.5.

234. M. R. Escalé, D. Pohl, A. Sergeyev, and R. Grange, "Extreme electro-optic tuning of Bragg mirrors integrated in lithium niobate nanowaveguides," Opt. Lett. **43**, 1515–1518 (2018).

235. A. Parriaux, K. Hammani, and G. Millot, "Electro-optic frequency combs," Adv. Opt. Photon. **12**, 223–287 (2020).

236. T. Ohara, H. Takara, T. Yamamoto, H. Masuda, T. Morioka, M. Abe, and H. Takahashi, "Over-1000-channel ultradense WDM transmission with supercontinuum multicarrier source," J. Lightwave Technol. **24**, 2311–2317 (2006).

237. C.-B. Huang, Z. Jiang, D. Leaird, J. Caraquitena, and A. Weiner, "Spectral line-by-line shaping for optical and microwave arbitrary waveform generations," Laser Photon. Rev. **2**, 227–248 (2008).

238. V. R. Supradeepa, C. M. Long, R. Wu, F. Ferdous, E. Hamidi, D. E. Leaird, and A. M. Weiner, "Comb-based radiofrequency photonic filters with rapid tunability and high selectivity," Nat. Photonics **6**, 186–194 (2012).

239. M. Abramowitz, I. A. Stegun, and D. Miller, "Handbook of mathematical functions with formulas, graphs and mathematical tables (National Bureau of Standards Applied Mathematics Series No. 55)," J. Appl. Mech. **32**, 239 (1965).

240. R. Wu, V. R. Supradeepa, C. M. Long, D. E. Leaird, and A. M. Weiner, "Generation of very flat optical frequency combs from continuous-wave lasers using cascaded intensity and phase modulators driven by tailored radio frequency waveforms," Opt. Lett. **35**, 3234–3236 (2010).

241. M. Xu, M. He, and X. Cai, "Generation of flat optical frequency comb using integrated cascaded lithium niobate modulators," in *Conference on Lasers and Electro-Optics* (Optical Society of America, 2020), paper STh1O.5.

242. T. Kobayashi, T. Sueta, Y. Cho, and Y. Matsuo, "High-repetition-rate optical pulse generator using a Fabry–Perot electro-optic modulator," Appl. Phys. Lett. **21**, 341–343 (1972).

243. M. Kourogi, K. Nakagawa, and M. Ohtsu, "Wide-span optical frequency comb generator for accurate optical frequency difference measurement," IEEE J. Quantum Electron. **29**, 2693–2701 (1993).

244. K. Ho and J. M. Kahn, "Optical frequency comb generator using phase modulation in amplified circulating loop," IEEE Photon. Technol. Lett. **5**, 721–725 (1993).

245. A. Rueda, F. Sedlmeir, M. Kumari, G. Leuchs, and H. G. L. Schwefel, "Resonant electro-optic frequency comb," Nature **568**, 378–381 (2019).

246. B. Buscaino, M. Zhang, M. Lončar, and J. M. Kahn, "Design of efficient resonator-enhanced electro-optic frequency comb generators," J. Lightwave Technol. **38**, 1400–1413 (2020).

247. N. Picqué and T. W. Hänsch, "Frequency comb spectroscopy," Nat. Photonics **13**, 146–157 (2019).

248. A. Shams-Ansari, M. Yu, Z. Chen, C. Reimer, M. Zhang, N. Picqué, and M. Lončar, "An integrated lithium-niobate electro-optic platform for spectrally tailored dual-comb spectroscopy," arXiv:2003.04533 (2020).

249. P. R. Griffiths and J. A. De Haseth, *Fourier Transform Infrared Spectrometry* (Wiley, 2007).

250. M. Yan, P.-L. Luo, K. Iwakuni, G. Millot, T. W. Hänsch, and N. Picqué, "Mid-infrared dual-comb spectroscopy with electro-optic modulators," Light Sci. Appl. **6**, e17076 (2017).

251. R. V. Kochanov, I. E. Gordon, L. S. Rothman, K. P. Shine, S. W. Sharpe, T. J. Johnson, T. J. Wallington, J. J. Harrison, P. F. Bernath, M. Birk, G. Wagner, K. Le Bris, I. Bravo, and C. Hill, "REPRINT OF: Infrared absorption cross-sections in HITRAN2016 and beyond: expansion for climate, environment, and atmospheric applications," J. Quant. Spectrosc. Radiat. Transfer **238**, 106708 (2019).

252. M.-G. Suh, Q.-F. Yang, K. Y. Yang, X. Yi, and K. J. Vahala, "Microresonator soliton dual-comb spectroscopy," Science **354**, 600–603 (2016).

253. A. Dutt, C. Joshi, X. Ji, J. Cardenas, Y. Okawachi, K. Luke, A. L. Gaeta, and M. Lipson, "On-chip dual-comb source for spectroscopy," Sci. Adv. **4**, e1701858 (2018).

254. A. Shams-Ansari, C. Reimer, N. Sinclair, M. Zhang, N. Picque, and M. Loncar, "Low-repetition-rate integrated electro-optic frequency comb sources," in *Conference on Lasers and Electro-Optics* (Optical Society of America, 2020), paper STh1O.2.

255. M. Bayer, T. Gutbrod, J. P. Reithmaier, A. Forchel, T. L. Reinecke, P. A. Knipp, A. A. Dremin, and V. D. Kulakovskii, "Optical modes in photonic molecules," Phys. Rev. Lett. **81**, 2582–2585 (1998).

256. J. M. Lukens and P. Lougovski, "Frequency-encoded photonic qubits for scalable quantum information processing," Optica **4**, 8–16 (2017).

257. A. Rueda, F. Sedlmeir, M. C. Collodo, U. Vogl, B. Stiller, G. Schunk, D. V. Strekalov, C. Marquardt, J. M. Fink, O. Painter, G. Leuchs, and H. G. L. Schwefel, "Efficient microwave to optical photon conversion: an electro-optical realization," Optica **3**, 597–604 (2016).

258. M. Tsang, "Cavity quantum electro-optics," Phys. Rev. A **81**, 063837 (2010).

259. M. Tsang, "Cavity quantum electro-optics. II. Input-output relations between traveling optical and microwave fields," Phys. Rev. A **84**, 043845 (2011).

260. V. S. Ilchenko, A. A. Savchenkov, A. B. Matsko, and L. Maleki, "Whispering-gallery-mode electro-optic modulator and photonic microwave receiver," J. Opt. Soc. Am. B **20**, 333–342 (2003).

261. M. Soltani, M. Zhang, C. Ryan, G. J. Ribeill, C. Wang, and M. Loncar, "Efficient quantum microwave-to-optical conversion using electro-optic nanophotonic coupled resonators," Phys. Rev. A **96**, 043808 (2017).

262. J. D. Witmer, T. P. McKenna, P. Arrangoiz-Arriola, R. Van Laer, E. Alex Wollack, F. Lin, A. K.-Y. Jen, J. Luo, and A. H. Safavi-Naeini, "A silicon-organic hybrid platform for quantum microwave-to-optical transduction," Quantum Sci. Technol. **5**, 034004 (2020).

263. W. Hease, A. Rueda, R. Sahu, M. Wulf, G. Arnold, H. G. L. Schwefel, and J. M. Fink, "Cavity quantum electro-optics: microwave-telecom conversion in the quantum ground state," PRX Quantum **1**, 020315 (2020).

264. M. Kjaergaard, M. E. Schwartz, J. Braumüller, P. Krantz, J. I.-J. Wang, S. Gustavsson, and W. D. Oliver, "Superconducting qubits: current state of play," Annu. Rev. Condens. Matter Phys. **11**, 369–395 (2020).

265. D. Awschalom, K. K. Berggren, H. Bernien, S. Bhave, L. D. Carr, P. Davids, S. E. Economou, D. Englund, A. Faraon, M. Fejer, S. Guha, M. V. Gustafsson, E. Hu, L. Jiang, J. Kim, B. Korzh, P. Kumar, P. G. Kwiat, M. Lončar, M. D. Lukin, D. A. B. Miller, C. Monroe, S. W. Nam, P. Narang, J. S. Orcutt, M. G. Raymer, A. H. Safavi-Naeini, M. Spiropulu, K. Srinivasan, S. Sun, J. Vučković, E. Waks, R. Walsworth, A. M. Weiner, and Z. Zhang, "Development of quantum interconnects for next-generation information technologies," PRX Quantum **2**, 017002 (2021).

266. N. Lauk, N. Sinclair, S. Barzanjeh, J. P. Covey, M. Saffman, M. Spiropulu, and C. Simon, "Perspectives on quantum transduction," Quantum Sci. Technol. **5**, 020501 (2020).

267. N. J. Lambert, A. Rueda, and F. Sedlmeir, "Coherent conversion between microwave and optical photons—an overview of physical implementations," Adv. Quantum **3**, 1900077 (2020).

268. Y. Xu, A. A. Sayem, L. Fan, S. Wang, R. Cheng, C.-L. Zou, W. Fu, L. Yang, M. Xu, and H. X. Tang, "Bidirectional electro-optic conversion reaching 1% efficiency with thin-film lithium niobate," arXiv:2012.14909 (2020).

269. L. Yuan, Q. Lin, M. Xiao, and S. Fan, "Synthetic dimension in photonics," Optica **5**, 1396–1405 (2018).

270. Y. Hu, C. Reimer, A. Shams-Ansari, M. Zhang, and M. Loncar, "Realization of high-dimensional frequency crystals in electro-optic microcombs," Optica **7**, 1189–1194 (2020).

271. L. Yuan and S. Fan, "Bloch oscillation and unidirectional translation of frequency in a dynamically modulated ring resonator," Optica **3**, 1014–1018 (2016).

272. Q. Lin, M. Xiao, L. Yuan, and S. Fan, "Photonic Weyl point in a two-dimensional resonator lattice with a synthetic frequency dimension," Nat. Commun. **7**, 13731 (2016).

273. L. Yuan, Y. Shi, and S. Fan, "Photonic gauge potential in a system with a synthetic frequency dimension," Opt. Lett. **41**, 741–744 (2016).

274. L. Yuan, M. Xiao, Q. Lin, and S. Fan, "Synthetic space with arbitrary dimensions in a few rings undergoing dynamic modulation," Phys. Rev. B **97**, 104105 (2018).

275. T. Ozawa, H. M. Price, N. Goldman, O. Zilberberg, and I. Carusotto, "Synthetic dimensions in integrated photonics: from optical isolation to four-dimensional quantum Hall physics," Phys. Rev. A **93**, 043827 (2016).

276. L. Yuan, Q. Lin, A. Zhang, M. Xiao, X. Chen, and S. Fan, "Photonic gauge potential in one cavity with synthetic frequency and orbital angular momentum dimensions," Phys. Rev. Lett. **122**, 083903 (2019).

277. A. Dutt, M. Minkov, Q. Lin, L. Yuan, D. A. B. Miller, and S. Fan, "Experimental band structure spectroscopy along a synthetic dimension," Nat. Commun. **10**, 3122 (2019).

278. A. Dutt, Q. Lin, L. Yuan, M. Minkov, M. Xiao, and S. Fan, "A single photonic cavity with two independent physical synthetic dimensions," Science **367**, 59–64 (2020).

279. K. Fang and S. Fan, "Controlling the flow of light using the inhomogeneous effective gauge field that emerges from dynamic modulation," Phys. Rev. Lett. **111**, 203901 (2013).

280. Q. Lin and S. Fan, "Light guiding by effective gauge field for photons," Phys. Rev. X **4**, 031031 (2014).

281. L. Yuan and S. Fan, "Three-dimensional dynamic localization of light from a time-dependent effective gauge field for photons," Phys. Rev. Lett. **114**, 243901 (2015).

282. L. Yuan and S. Fan, "Topologically nontrivial Floquet band structure in a system undergoing photonic transitions in the ultrastrong-coupling regime," Phys. Rev. A **92**, 053822 (2015).

283. K. Fang, Z. Yu, and S. Fan, "Photonic Aharonov-Bohm effect based on dynamic modulation," Phys. Rev. Lett. **108**, 153901 (2012).

284. K. Fang, Z. Yu, and S. Fan, "Realizing effective magnetic field for photons by controlling the phase of dynamic modulation," Nat. Photonics **6**, 782–787 (2012).

285. M. Minkov and V. Savona, "Haldane quantum Hall effect for light in a dynamically modulated array of resonators," Optica **3**, 200–206 (2016).

286. M. C. Rechtsman, J. M. Zeuner, Y. Plotnik, Y. Lumer, D. Podolsky, F. Dreisow, S. Nolte, M. Segev, and A. Szameit, "Photonic Floquet topological insulators," Nature **496**, 196–200 (2013).

287. L. Yuan, D.-W. Wang, and S. Fan, "Synthetic gauge potential and effective magnetic field in a Raman medium undergoing molecular modulation," Phys. Rev. A **95**, 033801 (2017).

288. R. W. Boyd, *Nonlinear Optics*, 3rd ed. (Academic, 2008).

289. Y. He, H. Liang, R. Luo, M. Li, and Q. Lin, "Dispersion engineered high quality lithium niobate microring resonators," Opt. Express **26**, 16315–16322 (2018).

290. D. E. Zelmon, D. L. Small, and D. Jundt, "Infrared corrected Sellmeier coefficients for congruently grown lithium niobate and 5 mol. % magnesium oxide–doped lithium niobate," J. Opt. Soc. Am. B **14**, 3319–3322 (1997).

291. M. Nie and S.-W. Huang, "Quadratic soliton mode-locked degenerate optical parametric oscillator," Opt. Lett. **45**, 2311–2314 (2020).

292. P. Vidaković, D. J. Lovering, J. A. Levenson, J. Webjörn, and P. St.J. Russell, "Large nonlinear phase shift owing to cascaded $\chi^{(2)}$ in quasi-phase-matched bulk LiNbO$_3$," Opt. Lett. **22**, 277–279 (1997).

293. Y. Okawachi, M. Yu, B. Desiatov, B. Y. Kim, T. Hansson, M. Lončar, and A. L. Gaeta, "Chip-based self-referencing using integrated lithium niobate waveguides," Optica **7**, 702–707 (2020).

294. M. Yu, L. Shao, Y. Okawachi, A. L. Gaeta, and M. Loncar, "Ultraviolet to mid-infrared supercontinuum generation in lithium-niobate waveguides," in *Conference on Lasers and Electro-Optics* (Optical Society of America, 2020), paper STu4H.1.

295. M. Jankowski, C. Langrock, B. Desiatov, A. Marandi, C. Wang, M. Zhang, C. R. Phillips, M. Lončar, and M. M. Fejer, "Ultrabroadband nonlinear optics in nanophotonic periodically poled lithium niobate waveguides," Optica **7**, 40–46 (2020).

296. R. Luo, Y. He, H. Liang, M. Li, and Q. Lin, "Semi-nonlinear nanophotonic waveguides for highly efficient second-harmonic generation," Laser Photon. Rev. **13**, 1800288 (2019).

297. R. Luo, Y. He, H. Liang, M. Li, and Q. Lin, "Highly tunable efficient second-harmonic generation in a lithium niobate nanophotonic waveguide," Optica **5**, 1006–1011 (2018).

298. M. C. Wengler, B. Fassbender, E. Soergel, and K. Buse, "Impact of ultraviolet light on coercive field, poling dynamics and poling quality of various lithium niobate crystals from different sources," J. Appl. Phys. **96**, 2816–2820 (2004).

299. V. Gopalan, T. E. Mitchell, Y. Furukawa, and K. Kitamura, "The role of nonstoichiometry in 180° domain switching of LiNbO$_3$ crystals," Appl. Phys. Lett. **72**, 1981–1983 (1998).

300. M. C. Wengler, M. Müller, E. Soergel, and K. Buse, "Poling dynamics of lithium niobate crystals," Appl. Phys. B **76**, 393–396 (2003).

301. J. T. Nagy and R. M. Reano, "Periodic poling of ion-sliced X-cut magnesium oxide doped lithium niobate thin films," in *Conference on Lasers and Electro-Optics* (Optical Society of America, 2018), paper SF2I.2.

302. J. T. Nagy and R. M. Reano, "Reducing leakage current during periodic poling of ion-sliced x-cut MgO doped lithium niobate thin films," Opt. Mater. Express **9**, 3146–3155 (2019).

303. L. Gui, *Periodically Poled Ridge Waveguides and Photonic Wires in LiNbO$_3$ for Efficient Nonlinear Interactions* (University of Paderborn, 2010).

304. G. Li, Y. Chen, H. Jiang, and X. Chen, "Broadband sum-frequency generation using d_{33} in periodically poled LiNbO$_3$ thin film in the telecommunications band," Opt. Lett. **42**, 939–942 (2017).

305. L. Ge, Y. Chen, H. Jiang, G. Li, B. Zhu, Y. Liu, and X. Chen, "Broadband quasi-phase matching in a MgO:PPLN thin film," Photon. Res. **6**, 954–958 (2018).

306. Z. Hao, L. Zhang, A. Gao, W. Mao, X. Lyu, X. Gao, F. Bo, F. Gao, G. Zhang, and J. Xu, "Periodically poled lithium niobate whispering gallery mode microcavities on a chip," Sci. China. Phys. Mech. Astron. **61**, 114211 (2018).

307. J. Zhao, M. Rüsing, and S. Mookherjea, "Optical diagnostic methods for monitoring the poling of thin-film lithium niobate waveguides," Opt. Express **27**, 12025–12038 (2019).

308. A. Rao, K. Abdelsalam, T. Sjaardema, A. Honardoost, G. F. Camacho-Gonzalez, and S. Fathpour, "Actively-monitored periodic-poling in thin-film lithium niobate photonic waveguides with ultrahigh nonlinear conversion efficiency of 4600%W^{-1}cm^{-2}," Opt. Express **27**, 25920–25930 (2019).

309. Y. Niu, C. Lin, X. Liu, Y. Chen, X. Hu, Y. Zhang, X. Cai, Y.-X. Gong, Z. Xie, and S. Zhu, "Optimizing the efficiency of a periodically poled LNOI waveguide using *in situ* monitoring of the ferroelectric domains," Appl. Phys. Lett. **116**, 101104 (2020).

310. J. Zhao, M. Rüsing, M. Roeper, L. M. Eng, and S. Mookherjea, "Poling thin-film x-cut lithium niobate for quasi-phase matching with sub-micrometer periodicity," J. Appl. Phys. **127**, 193104 (2020).

311. N. Ohnishi and T. Iizuka, "Etching study of microdomains in LiNbO$_3$ single crystals," J. Appl. Phys. **46**, 1063–1067 (1975).

312. J. Zhao, M. Rüsing, U. A. Javid, J. Ling, M. Li, Q. Lin, and S. Mookherjea, "Shallow-etched thin-film lithium niobate waveguides for highly-efficient second-harmonic generation," Opt. Express **28**, 19669–19682 (2020).

313. A. L. Kholkin, S. V. Kalinin, A. Roelofs, and A. Gruverman, "Review of ferroelectric domain imaging by piezoresponse force microscopy," in *Scanning Probe Microscopy: Electrical and Electromechanical Phenomena at the Nanoscale*, S. Kalinin and A. Gruverman, eds. (Springer, 2007), pp. 173–214.

314. M. Rüsing, J. Zhao, and S. Mookherjea, "Second harmonic microscopy of poled x-cut thin film lithium niobate: understanding the contrast mechanism," J. Appl. Phys. **126**, 114105 (2019).

315. G. Lin, J. U. Fürst, D. V. Strekalov, and N. Yu, "Wide-range cyclic phase matching and second harmonic generation in whispering gallery resonators," Appl. Phys. Lett. **103**, 181107 (2013).

316. D. V. Strekalov, C. Marquardt, A. B. Matsko, H. G. L. Schwefel, and G. Leuchs, "Nonlinear and quantum optics with whispering gallery resonators," J. Opt. **18**, 123002 (2016).

317. J. Fürst, B. Sturman, K. Buse, and I. Breunig, "Whispering gallery resonators with broken axial symmetry: theory and experiment," Opt. Express **24**, 20143–20155 (2016).

318. C. Wang, Z. Li, M.-H. Kim, X. Xiong, X.-F. Ren, G.-C. Guo, N. Yu, and M. Lončar, "Metasurface-assisted phase-matching-free second harmonic generation in lithium niobate waveguides," Nat. Commun. **8**, 2098 (2017).

319. A. Rao, J. Chiles, S. Khan, S. Toroghi, M. Malinowski, G. F. Camacho-González, and S. Fathpour, "Second-harmonic generation in single-mode integrated waveguides based on mode-shape modulation," Appl. Phys. Lett. **110**, 111109 (2017).

320. A. Boes, L. Chang, M. Knoerzer, T. G. Nguyen, J. D. Peters, J. E. Bowers, and A. Mitchell, "Improved second harmonic performance in periodically poled

LNOI waveguides through engineering of lateral leakage," Opt. Express **27**, 23919–23928 (2019).

321. X. Guo, C.-L. Zou, and H. X. Tang, "Second-harmonic generation in aluminum nitride microrings with 2500%/W conversion efficiency," Optica **3**, 1126–1131 (2016).

322. M. Minkov, D. Gerace, and S. Fan, "Doubly resonant $\chi(2)$ nonlinear photonic crystal cavity based on a bound state in the continuum," Optica **6**, 1039–1045 (2019).

323. U. A. Javid, J. Ling, J. Staffa, M. Li, Y. He, and Q. Lin, "Ultra-broadband entangled photons on a nanophotonic chip," arXiv:2101.04877 (2021).

324. Z. Ma, J.-Y. Chen, Z. Li, C. Tang, Y. M. Sua, H. Fan, and Y.-P. Huang, "Ultrabright quantum photon sources on chip," Phys. Rev. Lett. **125**, 263602 (2020).

325. R. Kumar and J. Ghosh, "Joint spectral amplitude analysis of SPDC photon pairs in a multimode ppLN ridge waveguide," arXiv:1906.10344 (2019).

326. G. I. Stegeman, D. J. Hagan, and L. Torner, "$\chi(2)$ cascading phenomena and their applications to all-optical signal processing, mode-locking, pulse compression and solitons," Opt. Quantum Electron. **28**, 1691–1740 (1996).

327. C. R. Phillips, C. Langrock, J. S. Pelc, M. M. Fejer, I. Hartl, and M. E. Fermann, "Supercontinuum generation in quasi-phasematched waveguides," Opt. Express **19**, 18754–18773 (2011).

328. M. Bache, J. Moses, and F. W. Wise, "Scaling laws for soliton pulse compression by cascaded quadratic nonlinearities," J. Opt. Soc. Am. B **24**, 2752–2762 (2007).

329. X. Liu, L. Qian, and F. Wise, "High-energy pulse compression by use of negative phase shifts produced by the cascade $\chi(2){:}\chi(2)$ nonlinearity," Opt. Lett. **24**, 1777–1779 (1999).

330. M. Bache, O. Bang, B. B. Zhou, J. Moses, and F. W. Wise, "Optical Cherenkov radiation in ultrafast cascaded second-harmonic generation," Phys. Rev. A **82**, 063806 (2010).

331. L. J. Qian, X. Liu, and F. W. Wise, "Femtosecond Kerr-lens mode locking with negative nonlinear phase shifts," Opt. Lett. **24**, 166–168 (1999).

332. X. Liu, F. O. Ilday, K. Beckwitt, and F. W. Wise, "Femtosecond nonlinear polarization evolution based on cascade quadratic nonlinearities," Opt. Lett. **25**, 1394–1396 (2000).

333. X. Liu, L. J. Qian, and F. W. Wise, "Generation of optical spatiotemporal solitons," Phys. Rev. Lett. **82**, 4631–4634 (1999).

334. F. Ö. Ilday, K. Beckwitt, Y.-F. Chen, H. Lim, and F. W. Wise, "Controllable Raman-like nonlinearities from nonstationary, cascaded quadratic processes," J. Opt. Soc. Am. B **21**, 376–383 (2004).

335. M. Bache, O. Bang, W. Krolikowski, J. Moses, and F. W. Wise, "Limits to compression with cascaded quadratic soliton compressors," Opt. Express **16**, 3273–3287 (2008).

336. T. J. Kippenberg, A. L. Gaeta, M. Lipson, and M. L. Gorodetsky, "Dissipative Kerr solitons in optical microresonators," Science **361**, eaan8083 (2018).

337. Z. Gong, X. Liu, Y. Xu, and H. X. Tang, "Near-octave lithium niobate soliton microcomb," Optica **7**, 1275–1278 (2020).

338. Z. Gong, M. Li, X. Liu, Y. Xu, J. Lu, A. Bruch, J. B. Surya, C. Zou, and H. X. Tang, "Photonic dissipation control for Kerr soliton generation in strongly Raman-active media," Phys. Rev. Lett. **125**, 183901 (2020).

339. Y. Xu, M. Shen, J. Lu, J. Surya, A. A. Sayem, and H. X. Tang, "Mitigating photorefractive effect in thin-film lithium niobate microring resonators," Opt. Express **29**, 5497–5504 (2021).

340. H.-C. Huang, J. I. Dadap, I. P. Herman, H. Bakhru, and R. M. Osgood, "Micro-Raman spectroscopic visualization of lattice vibrations and strain in He$^+$-implanted single-crystal LiNbO$_3$," Opt. Mater. Express **4**, 338–345 (2014).

341. H.-C. Huang, J. I. Dadap, O. Gaathon, I. P. Herman, R. M. Osgood, S. Bakhru, and H. Bakhru, "A micro-Raman spectroscopic investigation of He$_+$-irradiation damage in LiNbO$_3$," Opt. Mater. Express **3**, 126–142 (2013).

342. S. Sanna, S. Neufeld, M. Rüsing, G. Berth, A. Zrenner, and W. G. Schmidt, "Raman scattering efficiency in LiTaO$_3$ and LiNbO$_3$ crystals," Phys. Rev. B **91**, 224302 (2015).

343. P. S. Zelenovskiy, V. Y. Shur, P. Bourson, M. D. Fontana, D. K. Kuznetsov, and E. A. Mingaliev, "Raman study of neutral and charged domain walls in lithium niobate," Ferroelectrics **398**, 34–41 (2010).

344. S. Sanna, G. Berth, W. Hahn, A. Widhalm, A. Zrenner, and W. G. Schmidt, "Localised phonon modes at LiNbO$_3$ (0001) surfaces," Ferroelectrics **419**, 1–8 (2011).

345. M. Bache and R. Schiek, "Review of measurements of Kerr nonlinearities in lithium niobate: the role of the delayed Raman response," arXiv:1211.1721 (2012).

346. A. S. Barker and R. Loudon, "Dielectric properties and optical phonons in LiNbO$_3$," Phys. Rev. **158**, 433–445 (1967).

347. R. F. Schaufele and M. J. Weber, "Raman scattering by lithium niobate," Phys. Rev. **152**, 705–708 (1966).

348. W. D. Johnston, I. P. Kaminow, and J. G. Bergman, "Stimulated Raman gain coefficients for Li$_6$NbO$_3$, Ba$_2$NaNb$_5$O$_{15}$, and other materials," Appl. Phys. Lett. **13**, 190–193 (1968).

349. V. S. Gorelik and P. P. Sverbil', "Raman scattering by longitudinal and transverse optical vibrations in lithium niobate single crystals," Inorg. Mater. **51**, 1104–1110 (2015).

350. C. H. Henry and J. J. Hopfield, "Raman scattering by polaritons," Phys. Rev. Lett. **15**, 964–966 (1965).

351. M. Leidinger, B. Sturman, K. Buse, and I. Breunig, "Strong forward-backward asymmetry of stimulated Raman scattering in lithium-niobate-based whispering gallery resonators," Opt. Lett. **41**, 2823–2826 (2016).

352. J. M. Dudley, G. Genty, and S. Coen, "Supercontinuum generation in photonic crystal fiber," Rev. Mod. Phys. **78**, 1135–1184 (2006).

353. A. L. Gaeta, M. Lipson, and T. J. Kippenberg, "Photonic-chip-based frequency combs," Nat. Photonics **13**, 158–169 (2019).

354. D. Duchesne, M. Peccianti, M. R. E. Lamont, M. Ferrera, L. Razzari, F. Légaré, R. Morandotti, S. Chu, B. E. Little, and D. J. Moss, "Supercontinuum generation in a high index doped silica glass spiral waveguide," Opt. Express **18**, 923–930 (2010).

355. B. Kuyken, X. Liu, R. M. Osgood, Jr., R. Baets, G. Roelkens, and W. M. J. Green, "Mid-infrared to telecom-band supercontinuum generation in highly nonlinear silicon-on-insulator wire waveguides," Opt. Express **19**, 20172–20181 (2011).

356. R. Halir, Y. Okawachi, J. S. Levy, M. A. Foster, M. Lipson, and A. L. Gaeta, "Ultrabroadband supercontinuum generation in a CMOS-compatible platform," Opt. Lett. **37**, 1685–1687 (2012).

357. N. Singh, D. D. Hudson, Y. Yu, C. Grillet, S. D. Jackson, A. Casas-Bedoya, A. Read, P. Atanackovic, S. G. Duvall, S. Palomba, B. Luther-Davies, S. Madden, D. J. Moss, and B. J. Eggleton, "Midinfrared supercontinuum generation from 2 to 6 µm in a silicon nanowire," Optica **2**, 797–802 (2015).

358. X. Liu, M. Pu, B. Zhou, C. J. Krückel, A. Fülöp, V. Torres-Company, and M. Bache, "Octave-spanning supercontinuum generation in a silicon-rich nitride waveguide," Opt. Lett. **41**, 2719–2722 (2016).

359. D. Y. Oh, K. Y. Yang, C. Fredrick, G. Ycas, S. A. Diddams, and K. J. Vahala, "Coherent ultra-violet to near-infrared generation in silica ridge waveguides," Nat. Commun. **8**, 13922 (2017).

360. N. Singh, M. Xin, D. Vermeulen, K. Shtyrkova, N. Li, P. T. Callahan, E. S. Magden, A. Ruocco, N. Fahrenkopf, C. Baiocco, B. P.-P. Kuo, S. Radic, E. Ippen, F. X. Kärtner, and M. R. Watts, "Octave-spanning coherent supercontinuum generation in silicon on insulator from 1.06 μm to beyond 2.4 μm," Light Sci. Appl. **7**, 17131 (2018).

361. M. H. P. Pfeiffer, C. Herkommer, J. Liu, H. Guo, M. Karpov, E. Lucas, M. Zervas, and T. J. Kippenberg, "Octave-spanning dissipative Kerr soliton frequency combs in Si_3N_4 microresonators," Optica **4**, 684–691 (2017).

362. A. R. Johnson, A. S. Mayer, A. Klenner, K. Luke, E. S. Lamb, M. R. E. Lamont, C. Joshi, Y. Okawachi, F. W. Wise, M. Lipson, U. Keller, and A. L. Gaeta, "Octave-spanning coherent supercontinuum generation in a silicon nitride waveguide," Opt. Lett. **40**, 5117–5120 (2015).

363. A. Klenner, A. S. Mayer, A. R. Johnson, K. Luke, M. R. E. Lamont, Y. Okawachi, M. Lipson, A. L. Gaeta, and U. Keller, "Gigahertz frequency comb offset stabilization based on supercontinuum generation in silicon nitride waveguides," Opt. Express **24**, 11043–11053 (2016).

364. D. R. Carlson, D. D. Hickstein, A. Lind, S. Droste, D. Westly, N. Nader, I. Coddington, N. R. Newbury, K. Srinivasan, S. A. Diddams, and S. B. Papp, "Self-referenced frequency combs using high-efficiency silicon-nitride waveguides," Opt. Lett. **42**, 2314–2317 (2017).

365. M. A. G. Porcel, F. Schepers, J. P. Epping, T. Hellwig, M. Hoekman, R. G. Heideman, P. J. M. van der Slot, C. J. Lee, R. Schmidt, R. Bratschitsch, C. Fallnich, and K.-J. Boller, "Two-octave spanning supercontinuum generation in stoichiometric silicon nitride waveguides pumped at telecom wavelengths," Opt. Express **25**, 1542–1554 (2017).

366. D. Waldburger, A. S. Mayer, C. G. E. Alfieri, J. Nürnberg, A. R. Johnson, X. Ji, A. Klenner, Y. Okawachi, M. Lipson, A. L. Gaeta, and U. Keller, "Tightly locked optical frequency comb from a semiconductor disk laser," Opt. Express **27**, 1786–1797 (2019).

367. S. T. Cundiff and J. Ye, "Colloquium: femtosecond optical frequency combs," Rev. Mod. Phys. **75**, 325–342 (2003).

368. H. R. Telle, G. Steinmeyer, A. E. Dunlop, J. Stenger, D. H. Sutter, and U. Keller, "Carrier-envelope offset phase control: a novel concept for absolute optical frequency measurement and ultrashort pulse generation," Appl. Phys. B **69**, 327–332 (1999).

369. D. J. Jones, S. A. Diddams, J. K. Ranka, A. Stentz, R. S. Windeler, J. L. Hall, and S. T. Cundiff, "Carrier-envelope phase control of femtosecond mode-locked lasers and direct optical frequency synthesis," Science **288**, 635–640 (2000).

370. R. Holzwarth, T. Udem, T. W. Hansch, J. C. Knight, W. J. Wadsworth, and P. St.J. Russell, "Optical frequency synthesizer for precision spectroscopy," Phys. Rev. Lett. **85**, 2264–2267 (2000).

371. D. D. Hickstein, H. Jung, D. R. Carlson, A. Lind, I. Coddington, K. Srinivasan, G. G. Ycas, D. C. Cole, A. Kowligy, C. Fredrick, S. Droste, E. S. Lamb, N. R. Newbury, H. X. Tang, S. A. Diddams, and S. B. Papp, "Ultrabroadband supercontinuum generation and frequency-comb stabilization using on-chip waveguides with both cubic and quadratic nonlinearities," Phys. Rev. Appl. **8**, 014025 (2017).

372. Y. Okawachi, M. Yu, J. Cardenas, X. Ji, A. Klenner, M. Lipson, and A. L. Gaeta, "Carrier envelope offset detection via simultaneous supercontinuum and second-harmonic generation in a silicon nitride waveguide," Opt. Lett. **43**, 4627–4630 (2018).

373. D. D. Hickstein, D. R. Carlson, H. Mundoor, J. B. Khurgin, K. Srinivasan, D. Westly, A. Kowligy, I. I. Smalyukh, S. A. Diddams, and S. B. Papp, "Self-organized nonlinear gratings for ultrafast nanophotonics," Nat. Photonics **13**, 494–499 (2019).

374. J. Lu, J. B. Surya, X. Liu, Y. Xu, and H. X. Tang, "Octave-spanning supercontinuum generation in nanoscale lithium niobate waveguides," Opt. Lett. **44**, 1492–1495 (2019).

375. G. Genty, P. Kinsler, B. Kibler, and J. M. Dudley, "Nonlinear envelope equation modeling of sub-cycle dynamics and harmonic generation in nonlinear waveguides," Opt. Express **15**, 5382–5387 (2007).

376. S. Wabnitz and V. V. Kozlov, "Harmonic and supercontinuum generation in quadratic and cubic nonlinear optical media," J. Opt. Soc. Am. B **27**, 1707–1711 (2010).

377. T. Hansson, F. Leo, M. Erkintalo, J. Anthony, S. Coen, I. Ricciardi, M. De Rosa, and S. Wabnitz, "Single envelope equation modeling of multi-octave comb arrays in microresonators with quadratic and cubic nonlinearities," J. Opt. Soc. Am. B **33**, 1207–1215 (2016).

378. A. B. Fallahkhair, K. S. Li, and T. E. Murphy, "Vector finite difference mode-solver for anisotropic dielectric waveguides," J. Lightwave Technol. **26**, 1423–1431 (2008).

379. A. Efimov, A. V. Yulin, D. V. Skryabin, J. C. Knight, N. Joly, F. G. Omenetto, A. J. Taylor, and P. Russell, "Interaction of an optical soliton with a dispersive wave," Phys. Rev. Lett. **95**, 213902 (2005).

380. K. E. Webb, Y. Q. Xu, M. Erkintalo, and S. G. Murdoch, "Generalized dispersive wave emission in nonlinear fiber optics," Opt. Lett. **38**, 151–153 (2013).

381. Y. Okawachi, M. Yu, J. Cardenas, X. Ji, M. Lipson, and A. L. Gaeta, "Coherent, directional supercontinuum generation," Opt. Lett. **42**, 4466–4469 (2017).

382. M. Aspelmeyer, T. J. Kippenberg, and F. Marquardt, "Cavity optomechanics," Rev. Mod. Phys. **86**, 1391–1452 (2014).

383. H. C. Frankis, K. M. Kiani, D. Su, R. Mateman, A. Leinse, and J. D. B. Bradley, "High-Q tellurium-oxide-coated silicon nitride microring resonators," Opt. Lett. **44**, 118–121 (2019).

384. K. Vu and S. Madden, "Tellurium dioxide Erbium doped planar rib waveguide amplifiers with net gain and 2.8 dB/cm internal gain," Opt. Express **18**, 19192–19200 (2010).

385. M. S. I. Khan, A. Mahmoud, L. Cai, M. Mahmoud, T. Mukherjee, J. A. Bain, and G. Piazza, "Extraction of elastooptic coefficient of thin-film arsenic trisulfide using a Mach–Zehnder acoustooptic modulator on lithium niobate," J. Lightwave Technol. **38**, 2053–2059 (2020).

386. M. Mirhosseini, A. Sipahigil, M. Kalaee, and O. Painter, "Quantum transduction of optical photons from a superconducting qubit," Nature **588**, 599–603 (2020).

387. S. J. Whiteley, G. Wolfowicz, C. P. Anderson, A. Bourassa, H. Ma, M. Ye, G. Koolstra, K. J. Satzinger, M. V. Holt, F. J. Heremans, A. N. Cleland, D. I. Schuster, G. Galli, and D. D. Awschalom, "Spin–phonon interactions in silicon carbide addressed by Gaussian acoustics," Nat. Phys. **15**, 490–495 (2019).

388. C. Campbell, *Surface Acoustic Wave Devices and Their Signal Processing Applications* (Elsevier, 1989).

389. L. Shao, S. Maity, L. Zheng, L. Wu, A. Shams-Ansari, Y. I. Sohn, E. Puma, M. N. Gadalla, M. Zhang, C. Wang, E. Hu, K. Lai, and M. Lončar, "Phononic band

structure engineering for high- Q gigahertz surface acoustic wave resonators on lithium niobate," Phys. Rev. Appl. **12**, 014022 (2019).

390. F. M. Mayor, W. Jiang, C. J. Sarabalis, T. P. McKenna, J. D. Witmer, and A. H. Safavi-Naeini, "Gigahertz phononic integrated circuits on thin-film lithium niobate on sapphire," Phys. Rev. Appl. **15**, 014039 (2021).

391. L. Shao, D. Zhu, M. Colangelo, D. H. Lee, N. Sinclair, Y. Hu, P. T. Rakich, K. Lai, K. K. Berggren, and M. Loncar, "Electrical control of surface acoustic waves," arXiv:2101.01626 (2021).

392. Z. Y. Cheng and C. S. Tsai, "Baseband integrated acousto-optic frequency shifter," Appl. Phys. Lett. **60**, 12–14 (1992).

393. L. Shao, N. Sinclair, J. Leatham, Y. Hu, M. Yu, T. Turpin, D. Crowe, and M. Lončar, "Integrated microwave acousto-optic frequency shifter on thin-film lithium niobate," Opt. Express **28**, 23728–23738 (2020).

394. L. Cai, A. Mahmoud, M. Khan, M. Mahmoud, T. Mukherjee, J. Bain, and G. Piazza, "Acousto-optical modulation of thin film lithium niobate waveguide devices," Photon. Res. **7**, 1003–1013 (2019).

395. M. Mahmoud, A. Mahmoud, L. Cai, M. Khan, T. Mukherjee, J. Bain, and G. Piazza, "Novel on chip rotation detection based on the acousto-optic effect in surface acoustic wave gyroscopes," Opt. Express **26**, 25060–25075 (2018).

396. L. Cai and G. Piazza, "Low-loss waveguides in Y-cut thin film lithium niobate for acousto-optic applications," in *Conference on Lasers and Electro-Optics* (2019).

397. C. J. Sarabalis, T. P. McKenna, R. N. Patel, R. Van Laer, and A. H. Safavi-Naeini, "Acousto-optic modulation in lithium niobate on sapphire," APL Photon. **5**, 086104 (2020).

398. Z. Yu and X. Sun, "Gigahertz acousto-optic modulation and frequency shifting on etchless lithium niobate integrated platform," arXiv:2006.12187 (2020).

399. M. B. Tellekamp, J. C. Shank, M. S. Goorsky, and W. A. Doolittle, "Molecular beam epitaxy growth of high crystalline quality LiNbO$_3$," J. Electron. Mater. **45**, 6292–6299 (2016).

400. Y. D. Dahmani, C. J. Sarabalis, W. Jiang, F. M. Mayor, and A. H. Safavi-Naeini, "Piezoelectric transduction of a wavelength-scale mechanical waveguide," Phys. Rev. Appl. **13**, 024069 (2020).

401. L. Shao, M. Yu, S. Maity, N. Sinclair, L. Zheng, C. Chia, A. Shams-Ansari, C. Wang, M. Zhang, K. Lai, and M. Loncar, "Acoustically mediated microwave-to-optical conversion on thin-film lithium niobate," in *IEEE 33rd International Conference on Micro Electro Mechanical Systems* (MEMS) (2020), pp. 1215–1218.

402. B. E. A. Saleh and M. C. Teich, *Fundamentals of Photonics* (Wiley, 2019).

403. D. B. Sohn and G. Bahl, "Direction reconfigurable nonreciprocal acousto-optic modulator on chip," APL Photon. **4**, 126103 (2019).

404. E. A. Kittlaus, W. M. Jones, P. T. Rakich, N. T. Otterstrom, R. E. Muller, and M. Rais-Zadeh, "Electrically-driven acousto-optics and broadband non-reciprocity in silicon photonics," Nat. Photonics **15**, 43–52 (2021).

405. C. J. Sarabalis, R. Van Laer, R. N. Patel, Y. D. Dahmani, W. Jiang, F. M. Mayor, and A. H. Safavi-Naeini, "Acousto-optic modulation of a wavelength-scale waveguide," Optica **8**, 477–483 (2021).

406. G. T. Reed, G. Mashanovich, F. Y. Gardes, and D. J. Thomson, "Silicon optical modulators," Nat. Photonics **4**, 518–526 (2010).

407. A. Honardoost, F. A. Juneghani, R. Safian, and S. Fathpour, "Towards subter-ahertz bandwidth ultracompact lithium niobate electrooptic modulators," Opt. Express **27**, 6495–6501 (2019).

408. D. Pohl, M. Reig Escalé, M. Madi, F. Kaufmann, P. Brotzer, A. Sergeyev, B. Guldimann, P. Giaccari, E. Alberti, U. Meier, and R. Grange, "An integrated broadband spectrometer on thin-film lithium niobate," Nat. Photonics **14**, 24–29 (2020).

409. S. Ferrari, C. Schuck, and W. Pernice, "Waveguide-integrated superconducting nanowire single-photon detectors," Nanophotonics **7**, 1725–1758 (2018).

410. G. N. Gol'tsman, O. Okunev, G. Chulkova, A. Lipatov, A. Semenov, K. Smirnov, B. Voronov, A. Dzardanov, C. Williams, and R. Sobolewski, "Picosecond superconducting single-photon optical detector," Appl. Phys. Lett. **79**, 705–707 (2001).

411. C. M. Natarajan, M. G. Tanner, and R. H. Hadfield, "Superconducting nanowire single-photon detectors: physics and applications," Supercond. Sci. Technol. **25**, 063001 (2012).

412. B. Cabrera, R. M. Clarke, P. Colling, A. J. Miller, S. Nam, and R. W. Romani, "Detection of single infrared, optical, and ultraviolet photons using superconducting transition edge sensors," Appl. Phys. Lett. **73**, 735 (1998).

413. A. J. Miller, S. W. Nam, J. M. Martinis, and A. V. Sergienko, "Demonstration of a low-noise near-infrared photon counter with multiphoton discrimination," Appl. Phys. Lett. **83**, 791–793 (2003).

414. M. G. Tanner, L. S. E. Alvarez, W. Jiang, R. J. Warburton, Z. H. Barber, and R. H. Hadfield, "A superconducting nanowire single photon detector on lithium niobate," Nanotechnology **23**, 505201 (2012).

415. E. Smirnov, A. Golikov, P. Zolotov, V. Kovalyuk, M. Lobino, B. Voronov, A. Korneev, and G. Goltsman, "Superconducting nanowire single-photon detector on lithium niobate," J. Phys. Conf. Ser. **1124**, 051025 (2018).

416. J. P. Höpker, M. Bartnick, E. Meyer-Scott, F. Thiele, T. Meier, T. Bartley, S. Krapick, N. M. Montaut, M. Santandrea, H. Herrmann, S. Lengeling, R. Ricken, V. Quiring, A. E. Lita, V. B. Verma, T. Gerrits, S. W. Nam, and C. Silberhorn, "Towards integrated superconducting detectors on lithium niobate waveguides," Proc. SPIE **10358**, 1035809 (2017).

417. J. P. Höpker, T. Gerrits, A. Lita, S. Krapick, H. Herrmann, R. Ricken, V. Quiring, R. Mirin, S. W. Nam, C. Silberhorn, and T. J. Bartley, "Integrated transition edge sensors on titanium in-diffused lithium niobate waveguides," APL Photon. **4**, 056103 (2019).

418. M. Colangelo, B. Desiatov, D. Zhu, J. Holzgrafe, O. Medeiros, M. Loncar, and K. K. Berggren, "Superconducting nanowire single-photon detector on thin-film lithium niobate photonic waveguide," in *CLEO: Science and Innovations* (2020), paper SM4O.4.

419. B. Desiatov and M. Lončar, "Silicon photodetector for integrated lithium niobate photonics," Appl. Phys. Lett. **115**, 121108 (2019).

420. A. A. Sayem, R. Cheng, S. Wang, and H. X. Tang, "Lithium-niobate-on-insulator waveguide-integrated superconducting nanowire single-photon detectors," Appl. Phys. Lett. **116**, 151102 (2020).

421. R. Cheng, S. Wang, and H. X. Tang, "Superconducting nanowire single-photon detectors fabricated from atomic-layer- deposited NbN," Appl. Phys. Lett. **115**, 241101 (2019).

422. A. E. Dane, A. N. McCaughan, D. Zhu, Q. Zhao, C.-S. Kim, N. Calandri, A. Agarwal, F. Bellei, and K. K. Berggren, "Bias sputtered NbN and superconducting nanowire devices," Appl. Phys. Lett. **111**, 122601 (2017).

423. M. K. Akhlaghi, E. Schelew, and J. F. Young, "Waveguide integrated superconducting single-photon detectors implemented as near-perfect absorbers of coherent radiation," Nat. Commun. **6**, 8233 (2015).

424. R. Cheng, S. Wang, C.-L. Zou, and H. X. Tang, "Design of a micrometer-long superconducting nanowire perfect absorber for efficient high-speed single-photon detection," Photon. Res. **8**, 1260–1267 (2020).

425. N. A. Tyler, J. Barreto, G. E. Villarreal-Garcia, D. Bonneau, D. Sahin, J. L. O'Brien, and M. G. Thompson, "Modelling superconducting nanowire single photon detectors in a waveguide cavity," Opt. Express **24**, 8797–8808 (2016).

426. F. Najafi, J. Mower, N. C. Harris, F. Bellei, A. Dane, C. Lee, X. Hu, P. Kharel, F. Marsili, S. Assefa, K. K. Berggren, and D. Englund, "On-chip detection of non-classical light by scalable integration of single-photon detectors," Nat. Commun. **6**, 5873 (2015).

427. R. Hamerly, L. Bernstein, A. Sludds, M. Soljačić, and D. Englund, "Large-scale optical neural networks based on photoelectric multiplication," Phys. Rev. X **9**, 021032 (2019).

428. W. K. Chan, A. Yi-Yan, T. Gmitter, L. T. Florez, J. L. Jackel, E. Yablonovitch, R. Bhat, and J. P. Harbison, "GaAs photodetectors integrated with lithium niobate waveguides," IEEE Trans. Electron Devices **36**, 2627–2628 (1989).

429. J.-H. Kim, S. Aghaeimeibodi, C. J. K. Richardson, R. P. Leavitt, D. Englund, and E. Waks, "Hybrid integration of solid-state quantum emitters on a silicon photonic chip," Nano Lett. **17**, 7394–7400 (2017).

430. D. J. P. Ellis, A. J. Bennett, C. Dangel, J. P. Lee, J. P. Griffiths, T. A. Mitchell, T.-K. Paraiso, P. Spencer, D. A. Ritchie, and A. J. Shields, "Independent indistin-guishable quantum light sources on a reconfigurable photonic integrated circuit," Appl. Phys. Lett. **112**, 211104 (2018).

431. I. E. Zadeh, A. W. Elshaari, K. D. Jöns, A. Fognini, D. Dalacu, P. J. Poole, M. E. Reimer, and V. Zwiller, "Deterministic integration of single photon sources in silicon based photonic circuits," Nano Lett. **16**, 2289–2294 (2016).

432. S. Aghaeimeibodi, B. Desiatov, J.-H. Kim, C.-M. Lee, M. A. Buyukkaya, A. Karasahin, C. J. K. Richardson, R. P. Leavitt, M. Lončar, and E. Waks, "Integration of quantum dots with lithium niobate photonics," Appl. Phys. Lett. **113**, 221102 (2018).

433. D. White, A. Branny, R. J. Chapman, R. Picard, M. Brotons-Gisbert, A. Boes, A. Peruzzo, C. Bonato, and B. D. Gerardot, "Atomically-thin quantum dots integrated with lithium niobate photonic chips," Opt. Mater. Express **9**, 441–448 (2019).

434. M. J. F. Digonnet, *Rare-Earth-Doped Fiber Lasers and Amplifiers, Revised and Expanded* (CRC Press, 2001).

435. G. Liu and B. Jacquier, *Spectroscopic Properties of Rare Earths in Optical Materials* (Springer, 2006).

436. C. W. Thiel, T. Böttger, and R. L. Cone, "Rare-earth-doped materials for applications in quantum information storage and signal processing," J. Lumin. **131**, 353–361 (2011).

437. S. Dutta, E. A. Goldschmidt, S. Barik, U. Saha, and E. Waks, "Integrated photonic platform for rare-earth ions in thin film lithium niobate," Nano Lett. **20**, 741–747 (2020).

438. T. Zhong and P. Goldner, "Emerging rare-earth doped material platforms for quantum nanophotonics," Nanophotonics **8**, 2003–2015 (2019).

439. N. Sinclair, D. Oblak, C. W. Thiel, R. L. Cone, and W. Tittel, "Properties of a rare-earth-ion-doped waveguide at sub-kelvin temperatures for quantum signal processing," Phys. Rev. Lett. **118**, 100504 (2017).

440. D. Pak, H. An, A. Nandi, X. Jiang, Y. Xuan, and M. Hosseini, "Ytterbium-implanted photonic resonators based on thin film lithium niobate," J. Appl. Phys. **128**, 084302 (2020).

441. J. Zhou, Y. Liang, Z. Liu, W. Chu, H. Zhang, D. Yin, Z. Fang, R. Wu, J. Zhang, W. Chen, Z. Wang, Y. Zhou, M. Wang, and Y. Cheng, "On-chip integrated waveguide amplifiers on erbium-doped thin film lithium niobate on insulator," arXiv:2101.00783 (2021).

442. Z. Chen, Q. Xu, K. Zhang, W.-H. Wong, D.-L. Zhang, E. Y.-B. Pun, and C. Wang, "Efficient erbium-doped thin-film lithium niobate waveguide amplifiers," arXiv:2101.06994 (2021).

443. Z. Wang, Z. Fang, Z. Liu, W. Chu, Y. Zhou, J. Zhang, R. Wu, M. Wang, T. Lu, and Y. Cheng, "An on-chip tunable micro-disk laser fabricated on Er^{3+} doped lithium niobate on insulator (LNOI)," arXiv:2009.08953 (2020).

444. Q. Luo, Z. Hao, C. Yang, R. Zhang, D. Zheng, S. Liu, H. Liu, F. Bo, Y. Kong, G. Zhang, and J. Xu, "Microdisk lasers on an erbium-doped lithium-niobite chip," Sci. China Phys. Mech. Astron. **64**, 100504 (2021).

445. Y. Liu, X. Yan, J. Wu, B. Zhu, Y. Chen, and X. Chen, "On-chip erbium-doped lithium niobate microcavity laser," Sci. China Phys. Mech. Astron. **64**, 234262 (2021).

446. S. Sun, M. He, M. Xu, S. Gao, S. Yu, and X. Cai, "Hybrid silicon and lithium niobate modulator," IEEE J. Sel. Top. Quantum Electron. **27**, 3300112 (2021).

447. G. Roelkens, L. Liu, D. Liang, R. Jones, A. Fang, B. Koch, and J. Bowers, "III-V/silicon photonics for on-chip and intra-chip optical interconnects," Laser Photon. Rev. **4**, 751–779 (2010).

448. J. Zhang, B. Haq, J. O'Callaghan, A. Gocalinska, E. Pelucchi, A. J. Trindade, B. Corbett, G. Morthier, and G. Roelkens, "Transfer-printing-based integration of a III-V-on-silicon distributed feedback laser," Opt. Express **26**, 8821–8830 (2018).

449. Y. Wang, Z. Wang, Q. Yu, X. Xie, T. Posavitz, M. Jacob-Mitos, A. Ramaswamy, E. J. Norberg, G. A. Fish, and A. Beling, "High-power photodiodes with 65 GHz bandwidth heterogeneously integrated onto silicon-on-insulator nano-waveguides," IEEE J. Sel. Top. Quantum Electron. **24**, 6000206 (2018).

450. Q. Yu, J. Gao, N. Ye, B. Chen, K. Sun, L. Xie, K. Srinivasan, M. Zervas, G. Navickaite, M. Geiselmann, and A. Beling, "Heterogeneous photodiodes on silicon nitride waveguides," Opt. Express **28**, 14824–14830 (2020).

451. J. Zhang, G. Muliuk, J. Juvert, S. Kumari, J. Goyvaerts, B. Haq, C. Op de Beeck, B. Kuyken, G. Morthier, D. Van Thourhout, R. Baets, G. Lepage, P. Verheyen, J. Van Campenhout, A. Gocalinska, J. O'Callaghan, E. Pelucchi, K. Thomas, B. Corbett, A. J. Trindade, and G. Roelkens, "III-V-on-Si photonic integrated circuits realized using micro-transfer-printing," APL Photon. **4**, 110803 (2019).

452. R. Gerson, J. F. Kirchhoff, L. E. Halliburton, and D. A. Bryan, "Photoconductivity parameters in lithium niobate," J. Appl. Phys. **60**, 3553–3557 (1986).

453. P. Günter and J.-P. Huignard, *Photorefractive Materials and Their Applications 1: Basic Effects* (Springer, 2005).

454. S. Yamada and M. Minakata, "DC drift phenomena in $LiNbO_3$ optical waveguide devices," Jpn. J. Appl. Phys. **20**, 733–737 (1981).

455. H. Jiang, R. Luo, H. Liang, X. Chen, Y. Chen, and Q. Lin, "Fast response of photorefraction in lithium niobate microresonators," Opt. Lett. **42**, 3267–3270 (2017).

456. X. Sun, H. Liang, R. Luo, W. C. Jiang, X.-C. Zhang, and Q. Lin, "Nonlinear optical oscillation dynamics in high-Q lithium niobate microresonators," Opt. Express **25**, 13504–13516 (2017).

457. J. B. Surya, J. Lu, Y. Xu, and H. X. Tang, "Stable tuning of photorefractive microcavities using an auxiliary laser," Opt. Lett. **46**, 328–331 (2021).

458. P. Günter and J.-P. Huignard, eds., *Photorefractive Materials and Their Applications 1: Basic Effects* (Springer, 2006).

459. V. E. Wood, P. J. Cressman, R. L. Holman, and C. M. Verber, *Photorefractive Effects in Waveguides, Photorefractive Materials and Their Applications II. Topics in Applied Physics*, P. Günter and J. P. Huignard, eds. (Springer, 1989), Vol. **62**.

460. Y. Kong, F. Bo, W. Wang, D. Zheng, H. Liu, G. Zhang, R. Rupp, and J. Xu, "Recent progress in lithium niobate: optical damage, defect simulation, and on-chip devices," Adv. Mater. **32**, 1806452 (2020).

461. J. Rams, A. Alcázar-de-Velasco, M. Carrascosa, J. M. Cabrera, and F. Agulló-López, "Optical damage inhibition and thresholding effects in lithium niobate above room temperature," Opt. Commun. **178**, 211–216 (2000).

462. R. A. Becker, "Circuit effect in LiNbO$_3$ channel-waveguide modulators," Opt. Lett. **10**, 417–419 (1985).

463. C. M. Gee, G. D. Thurmond, H. Blauvelt, and H. W. Yen, "Minimizing dc drift in LiNbO$_3$ waveguide devices," Appl. Phys. Lett. **47**, 211–213 (1985).

464. S. K. Korotky and J. J. Veselka, "An RC network analysis of long term Ti:LiNbO$_3$ bias stability," J. Lightwave Technol. **14**, 2687–2697 (1996).

465. J. Holzgrafe, N. Sinclair, D. Zhu, A. Shams-Ansari, M. Colangelo, Y. Hu, M. Zhang, K. K. Berggren, and M. Loncar, "Toward efficient microwave-optical transduction using cavity electro-optics in thin-film lithium niobate," in *Conference on Lasers and Electro-Optics* (OSA, 2020).

466. S. Sun, M. He, M. Xu, S. Gao, Z. Chen, X. Zhang, Z. Ruan, X. Wu, L. Zhou, L. Liu, C. Lu, C. Guo, L. Liu, S. Yu, and X. Cai, "Bias-drift-free Mach–Zehnder modulators based on a heterogeneous silicon and lithium niobate platform," Photon. Res. **8**, 1958–1963 (2020).

467. H.-S. Zhong, H. Wang, Y.-H. Deng, M.-C. Chen, L.-C. Peng, Y.-H. Luo, J. Qin, D. Wu, X. Ding, Y. Hu, P. Hu, X.-Y. Yang, W.-J. Zhang, H. Li, Y. Li, X. Jiang, L. Gan, G. Yang, L. You, Z. Wang, L. Li, N.-L. Liu, C.-Y. Lu, and J.-W. Pan, "Quantum computational advantage using photons," Science **370**, 1460–1463 (2020).

468. J. Wang, F. Sciarrino, A. Laing, and M. G. Thompson, "Integrated photonic quantum technologies," Nat. Photonics **14**, 273–284 (2020).

469. J. Wang, S. Paesani, Y. Ding, R. Santagati, P. Skrzypczyk, A. Salavrakos, J. Tura, R. Augusiak, L. Mančinska, D. Bacco, D. Bonneau, J. W. Silverstone, Q. Gong, A. Acín, K. Rottwitt, L. K. Oxenløwe, J. L. O'Brien, A. Laing, and M. G. Thompson, "Multidimensional quantum entanglement with large-scale integrated optics," Science **360**, 285–291 (2018).

470. N. C. Harris, J. Carolan, D. Bunandar, M. Prabhu, M. Hochberg, T. Baehr-Jones, M. L. Fanto, A. M. Smith, C. C. Tison, P. M. Alsing, and D. Englund, "Linear programmable nanophotonic processors," Optica **5**, 1623–1631 (2018).

471. I. Dhand, "Circumventing defective components in linear optical interferometers," arXiv:1912.08789 (2019).

472. S. Slussarenko and G. J. Pryde, "Photonic quantum information processing: a concise review," Appl. Phys. Rev. **6**, 041303 (2019).

473. H.-H. Lu, J. M. Lukens, B. P. Williams, P. Imany, N. A. Peters, A. M. Weiner, and P. Lougovski, "A controlled-NOT gate for frequency-bin qubits," npj Quantum Inf. **5**, 24 (2019).

474. I. Marcikic, H. de Riedmatten, W. Tittel, V. Scarani, H. Zbinden, and N. Gisin, "Time-bin entangled qubits for quantum communication created by femtosecond pulses," Phys. Rev. A **66**, 062308 (2002).

475. C. Joshi, A. Farsi, C. Clemmen, S. Ramelow, and A. Gaeta, "Frequency multiplexing for quasi-deterministic heralded single-photon sources," Nat. Commun. **9**, 847 (2018).

476. C. Joshi, A. Farsi, A. Dutt, B.-Y. Kim, X. Ji, Y. Zhao, A. M. Bishop, M. Lipson, and A. L. Gaeta, "Frequency-domain quantum interference with correlated photons from an integrated microresonator," Phys. Rev. Lett. **124**, 143601 (2020).

477. Y. Soudagar, F. Bussières, G. Berlín, S. Lacroix, J. M. Fernandez, and N. Godbout, "Cluster-state quantum computing in optical fibers," J. Opt. Soc. Am. B **24**, 226–230 (2007).

478. M. Kues, C. Reimer, P. Roztocki, L. R. Cortés, S. Sciara, B. Wetzel, Y. Zhang, A. Cino, S. T. Chu, B. E. Little, D. J. Moss, L. Caspani, J. Azaña, and R. Morandotti, "On-chip generation of high-dimensional entangled quantum states and their coherent control," Nature **546**, 622–626 (2017).

479. F. Kaneda and P. G. Kwiat, "High-efficiency single-photon generation via large-scale active time multiplexing," Sci. Adv. **5**, eaaw8586 (2019).

480. M. G. Puigibert, G. H. Aguilar, Q. Zhou, F. Marsili, M. D. Shaw, V. B. Verma, S. W. Nam, D. Oblak, and W. Tittel, "Heralded single photons based on spectral multiplexing and feed-forward control," Phys. Rev. Lett. **119**, 1–6 (2017).

481. C. Etrich, U. Peschel, and F. Lederer, "Solitary waves in quadratically nonlinear resonators," Phys. Rev. Lett. **79**, 2454–2457 (1997).

482. A. U. Nielsen, Y. Xu, M. Ferré, M. G. Clerc, S. Coen, S. G. Murdoch, and M. Erkintalo, "Engineered discreteness enables observation and control of chimera-like states in a system with local coupling," arXiv:1910.11329 (2019).

483. A. K. Tusnin, A. M. Tikan, and T. J. Kippenberg, "Nonlinear states and dynamics in a synthetic frequency dimension," Phys. Rev. A **102**, 023518 (2020).

484. M. Zhang, C. Reimer, L. He, R. Cheng, M. Yu, R. Zhu, and M. Loncar, "Microresonator frequency comb generation with simultaneous Kerr and electro-optic nonlinearities," in *Conference on Lasers and Electro-Optics (CLEO)* (IEEE, 2019), pp. 1–2.

485. Y. Shi, Z. Yu, and S. Fan, "Limitations of nonlinear optical isolators due to dynamic reciprocity," Nat. Photonics **9**, 388–392 (2015).

486. K. Abdelsalam, T. Li, J. B. Khurgin, and S. Fathpour, "Linear isolators using wavelength conversion," Optica **7**, 209–213 (2020).

487. Z. Yu and S. Fan, "Complete optical isolation created by indirect interband photonic transitions," Nat. Photonics **3**, 91–94 (2009).

488. D. L. Sounas and A. Alù, "Non-reciprocal photonics based on time modulation," Nat. Photonics **11**, 774–783 (2017).

489. J. Wang, Y. Shi, and S. Fan, "Non-reciprocal polarization rotation using dynamic refractive index modulation," Opt. Express **28**, 11974–11982 (2020).

490. L. D. Tzuang, K. Fang, P. Nussenzveig, S. Fan, and M. Lipson, "Non-reciprocal phase shift induced by an effective magnetic flux for light," Nat. Photonics **8**, 701–705 (2014).

491. H. Lira, Z. Yu, S. Fan, and M. Lipson, "Electrically driven nonreciprocity induced by interband photonic transition on a silicon chip," Phys. Rev. Lett. **109**, 033901 (2012).

492. D. B. Sohn, S. Kim, and G. Bahl, "Time-reversal symmetry breaking with acoustic pumping of nanophotonic circuits," Nat. Photonics **12**, 91–97 (2018).

493. E. A. Kittlaus, N. T. Otterstrom, P. Kharel, S. Gertler, and P. T. Rakich, "Non-reciprocal interband Brillouin modulation," Nat. Photonics **12**, 613–619 (2018).

494. D. Marpaung, J. Yao, and J. Capmany, "Integrated microwave photonics," Nat. Photonics **13**, 80–90 (2019).

495. Y. Liu, A. Choudhary, D. Marpaung, and B. J. Eggleton, "Integrated microwave photonic filters," Adv. Opt. Photon. **12**, 485–555 (2020).

496. C. Deakin and Z. Liu, "Dual frequency comb assisted analog-to-digital conversion," Opt. Lett. **45**, 173–176 (2020).
497. K. Luke, P. Kharel, C. Reimer, L. He, M. Loncar, and M. Zhang, "Wafer-scale low-loss lithium niobate photonic integrated circuits," Opt. Express **28**, 24452–24458 (2020).
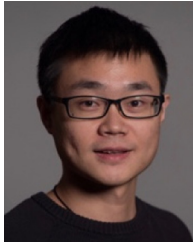
Di Zhu is a postdoctoral fellow at Harvard University. He received his Ph.D. (2019) and M.Sc. (2017) from the Massachusetts Institute of Technology, and his B.Eng. (2013) from Nanyang Technological University, all in Electrical Engineering. His current research interests include integrated quantum photonics, applied superconductivity, and nanoscale electromagnetics. His Ph.D. thesis on superconducting nanowire single-photon detectors was recognized by the MIT Jin-Au Kong thesis award. He was a recipient of the inaugural Harvard Quantum Initiative Postdoctoral Fellowship and A*STAR National Science Scholarship.
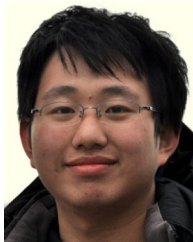
Linbo Shao is a Postdoctoral Fellow at Harvard University. He received his Ph.D. in engineering science (2019) and M.S. in applied physics (2014) from Harvard University, and a B.S. in microelectronics (2014) from Peking University. He works on integrated acousto-optics and electro-acoustics on the lithium-niobate platform and color centers in diamond.

Mengjie Yu is a postdoctoral fellow in the John A. Paulson School of Engineering and Applied Sciences at Harvard University. She received her Ph.D. in Electrical Engineering in 2018 from Cornell University. Her research focuses on integrated photonics in silicon, silicon nitride, and lithium-niobate platforms, and her interests include nonlinear frequency conversion, frequency combs, mid-infrared photonics, and optical coherent computing. Mengjie Yu is the 2020 OSA Ambassador. She was the winner of the 2016 Maiman Student Paper Competition and the 2016 Emil Wolf Student Paper Competition, and a finalist of the 2020 Tingye Li Innovation Prize. She was the Caltech 2019 Young Investigator Lecturer. She has published 32 peer-reviewed journal papers and 44 conference papers and is a referee for 15 peer-reviewed journals. Currently, she serves as chair of the OSA Integrated Optics Technical Group.
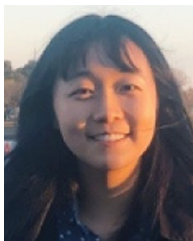
Rebecca Cheng is a graduate student in Applied Physics at Harvard University. She received her Sc.B. in Mathematical Physics from Brown University in 2018. She is currently studying integrated nonlinear photonics in Professor Marko Lončar's group.

Boris Desiatov received his BS in Physics and Mathematics in 2006 and an MS and a Ph.D. in Applied Physics from the Hebrew University of Jerusalem, Israel, in 2015. After a postdoctoral fellowship at Harvard University, he joined Bar Ilan University as Assistant Professor of Electrical Engineering. His research is focused on integrated photonic devices, quantum information, quantum optics, electro-optical systems, and nonlinear optics.

CJ Xin is a Ph.D. student in Applied Physics at Harvard University. With the Lončar Group since 2018, she has been working on quantum frequency conversion in the thin-film lithium niobate on insulator photonic platform. She is interested in developing scalable sources of single photons and entangled photon pairs for quantum information processing.
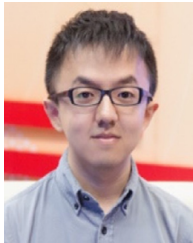
Yaowen Hu is a graduate student in the Department of Physics at Harvard University. He received his Bachelor of Science in Physics at Tsinghua University in 2018. During his undergraduate studies, he worked on coupling superconducting qubits with spin ensembles. He was awarded the highest honor and the Students of the Year award of Tsinghua University, both in 2017. He is currently working in Prof. Marko Lončar's group. His main interests are photonic computing, nonlinear photonics, and topological photonics.

Jeffrey Holzgrafe is a Ph.D. candidate in Applied Physics at Harvard University. He received his M.Phil. in Physics from the University of Cambridge in 2017, supported by a Marshall Scholarship, and his B.S. in Engineering from Olin College in 2015, supported by a Goldwater Scholarship. Jeffrey is currently studying integrated photonics and quantum transduction in Marko Lončar's Laboratory for Nanoscale Optics.

Soumya Ghosh is a Ph.D. student in Physics at Harvard University, currently supported by an NSF Graduate Research Fellowship. He received his Sc.B in Mathematical Physics from Brown University, and is studying integrated nonlinear photonics in Marko Lončar's Laboratory for Nanoscale Optics.

Amirhassan Shams-Ansari is a Ph.D. student in Electrical Engineering at Harvard University. He started his Ph.D. by exploring nonlinear-optical phenomena in a single-crystalline diamond platform. Over the last few years, he has mainly been working on studying the thin-film lithium-niobate platform's fundamental limitations, developing integrated electro-optics frequency combs, and implementing LN integrated devices in practical applications such as gas-phase spectroscopy.
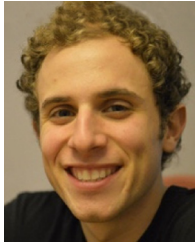
Eric Puma received his B.A. in Physics from Pomona College (2014) and his M.S. in Applied Physics from Harvard University (2020), where he is currently a Ph.D. candidate in the group of Marko Lončar. His work focuses on the advancement of the lithium niobate on insulator platform for integrated quantum photonics. Formerly, he worked in the group of Frank Koppens at ICFO (2014–2017) developing graphene optoelectronics. Outside the lab, Eric is a musician and cyclist, serving as director of the Harvard World Music Collective (2018–2019) and as co-founder of the Caravan Project.

Neil Sinclair is a postdoctoral fellow in the group of Marko Lončar at Harvard University working on projects in nanophotonics and is co-appointed at the California Institute of Technology to develop quantum networks under Maria Spiropulu. Neil worked on quantum entanglement theory in the group of Shohini Ghose during his B.Sc. studies at the University of Waterloo. For his graduate work, he developed quantum science experiments using rare-earth-ion-doped crystals under Wolfgang Tittel at the University of Calgary.

Christian Reimer is a physicist and entrepreneur working in the fields of nonlinear optics, integrated photonics, and quantum optics. He received graduate degrees from the Karlsruhe Institute of Technology in Germany, Heriot-Watt University in Scotland, and the National Institute of Scientific Research in Canada. He then worked as a postdoctoral fellow at Harvard University, before becoming Co-Founder and Head of Product of HyperLight Corporation. HyperLight, a Venture-Capital funded start-up out of Harvard University, is specialized on integrated lithium-niobate technologies for ultra-high-performance photonic solutions.
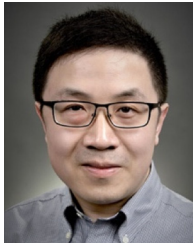
Mian Zhang is co-founder and CEO of HyperLight, a VC backed startup company located in Cambridge, MA, focusing on the commercialization of ultra-high-performance lithium-niobate integrated photonics technology. He has pioneered the technical development of the thin-film lithium-niobate photonic platform during his postdoc at Harvard. Mian obtained his Ph.D. from Cornell University in 2015. Prior to that, he received his Bachelor's degree from the University of Bristol.

Marko Lončar is Tiantsai Lin Professor of Electrical Engineering at Harvard's John A Paulson School of Engineering and Applied Sciences (SEAS), as well as a Harvard College Professor. Lončar received his diploma from the University of Belgrade (R. Serbia) in 1997, and his Ph.D. from Caltech in 2003 (with Axel Scherer), both in Electrical Engineering. After completing his postdoctoral studies at Harvard (with Federico Capasso), he joined the SEAS faculty in 2006. Lončar is an expert in nanophotonics and nanofabrication, and his current research interests include quantum and nonlinear nanophotonics, quantum optomchanics, high-power optics, and nanofabrication. He has received the NSF CAREER Award in 2009 and a Sloan Fellowship in 2010. In recognition of his teaching activities, Lončar has been awarded the Levenson Prize for Excellence in Undergraduate Teaching (2012), and was named Harvard College Professor in 2017. Lončar is a fellow of the The Optical Society and a Senior Member of IEEE and SPIE.